Politecnico di Milano

School of Industrial and Information Engineering

Department of Chemistry, Materials and Chemical Engineering “Giulio Natta”

Master of Science in Materials Engineering and Nanotechnology

Density functional study of vibrational properties of $\pi-$conjugated and ferroelectric polymers

Master Thesis of
Gianluca SERRA
Matriculation Number: 898981

Supervisor:
Professor Matteo TOMMASINI

Co-supervisor:
Professor Chiara CASTIGLIONI

Academic Year 2019/2020

Hoppípolla
I engum stígvélum
Allur rennvotur (rennblautur)
I engum stígvélum

Og ég fæ blóðnasir
En ég stend alltaf upp

Abstract

Advanced materials are complex systems, and the comprehension of the physical mechanisms underlying their macroscopic properties requires the insight of theoretical methods. Among these, density functional theory (DFT) is the most popular in materials science. In this Thesis, a density functional investigation of vibrational properties of three advanced materials of current interest in the field of materials engineering is performed.

The first material is an electron-transporting $\pi-$conjugated polymer known in the literature as P(NDI2OD-T2). Starting from recent spectroscopic experiments unveiling the localization of structural relaxation following its n-doping [1], DFT is applied to simulate the electronic charge distribution in the polymer both in the absence and in the presence of an atomic dopant. Then, different atomic dopants are considered to draw further conclusions about the effect of charge-screening on electron delocalization.

The focus is then shifted onto functionalized graphene nanoribbons, and their vibrational and electronic spectra are simulated for selected choices of the functional groups and different lengths of the $\pi-$conjugated backbone. In doing this, the most prominent features of IR, Raman and UV-Vis spectra are assigned.

Finally, the β phase of PVDF and P(VDF$-$TrFE), both ferroelectric polymers, are studied. The existence of vibrational markers for the chemical unit TrFE in P(VDF$-$TrFE) is predicted, corroborating recent results obtained by vibrational spectroscopy [2]. Then, conformational disorder is modeled in a simple way to account for the temperature dependence of IR and Raman spectra of P(VDF$-$TrFE). Finally, a series of periodic three-dimensional models with different cell parameters is used to highlight solid-state effects on the IR and Raman spectra of PVDF.

The results presented in this Thesis show the usefulness of DFT in the prediction and corroboration of experimental results concerning the vibrational properties of advanced materials which are at the center of current research interest.

Keywords: Density functional theory, Vibrational spectroscopy, P(NDI2OD-T2), Graphene nanoribbons, PVDF, P(VDF$-$TrFE)

Sommario

I materiali avanzati sono sistemi complessi, e la comprensione dei meccanismi fisici alla base delle loro proprietà macroscopiche richiede l'utilizzo di metodi teorici. Tra questi, la teoria del funzionale della densità (*Density Functional Theory*, DFT) è il più popolare in scienza dei materiali. In questa Tesi, si esegue una indagine DFT delle proprietà vibrazionali di tre materiali avanzati di interesse attuale nel campo dell'ingegneria dei materiali.

Il primo materiale è un polimero trasportatore di elettroni $\pi-$coniugato conosciuto in letteratura come P(NDI2OD-T2). A partire da recenti esperimenti che svelano la localizzazione del rilassamento strutturale a seguito del suo drogaggio n [1], la DFT è applicata per simulare la distribuzione di carica elettronica nel polimero sia in assenza che in presenza di un drogante atomico. Successivamente, diversi droganti atomici vengono considerati per trarre ulteriori conclusioni sull'effetto dello schermaggio di carica sulla delocalizzazione elettronica.

Si sposta poi l'attenzione sui nanoribbon di grafene funzionalizzati, e i loro spettri vibrazionali ed elettronici sono simulati per una selezione di gruppi funzionali e a diverse lunghezze della catena dorsale $\pi-$coniugata. Così facendo, si assegnano i picchi più importanti degli spettri IR, Raman e UV-Vis.

Infine, la fase β di PVDF e P(VDF$-$TrFE), entrambi polimeri ferroelettrici, sono studiati. Si predice l'esistenza di marker vibrazionali per l'unità chimica TrFE in P(VDF$-$TrFE), corroborando recenti risultati ottenuti tramite spettroscopia vibrazionale [2]. Successivamente, il disordine conformazionale è modellato in modo semplice per rendere conto della dipendenza dalla temperatura degli spettri IR e Raman di P(VDF$-$TrFE). Infine, una serie di modelli periodici tridimensionali con diversi parametri di cella è usata per mettere in luce gli effetti di stato solido sugli spettri IR e Raman di PVDF.

I risultati presentati in questa Tesi mostrano l'utilità della DFT per la predizione e corroborazione di risultati sperimentali riguardanti le proprietà vibrazionali di materiali avanzati al centro dell'interesse di ricerca attuale.

Parole chiave: Teoria del funzionale della densità, Spettroscopia vibrazionale, P(NDI2OD-T2), Nanoribbon di grafene, PVDF, P(VDF$-$TrFE)

Acknowledgement

It is impossible not to divide life in key moments. At least, this is impossible *for me.* I recall one key moment at elementary school, when I said: la mia prima matita spezzata.[1] And then the 8:35 of the first day of final exams, when five Virgil-teachers threw open at the same time the five doors with panic bars of Liceo Volta di Milano, to lead a hundred of Dante-students to their classrooms. Maybe we were more, and it was not even eight. But it does not matter.

Another key moment is that in which I am writing these words on the application *Text Edit* of my computer.[2] It is natural to want to thank everyone now, but I know this is not possible. In any case, I will move starting from this Thesis to the outside. In this way, I will place my friends in between my two guides. My family will not take this personally, because all of the following pages are dedicated to them.

Now the opening quote of this Thesis translates from Icelandic as [3]:

> *Hopping into puddles*
> *Completely drenched*
> *Soaked*
> *With no boots on*
>
> *And I get nosebleed*
> *But I always get up*

I like this song. It is the background of all of what follows. Thank you to professor Tommasini, who will be conceived as my thesis prof, in secret, forever. Thank you to professor Castiglioni, who made me discover that we are not islands. Thank you to professor del Zoppo, who told me the right thing. Thank you to professor Bertarelli, who made me feel accepted. Thank you to professor Milani, who helped me. Thank you to Alessia[3] and Valentina from The Balsamic Association of Friends for being here. Thank you to all my friends of Poli, because when I think: maybe I should have done this, or that, I immediately say: but I would not have met them. Thank you to my friends of Patio and BCA, whom I miss. Thank you to my friends, in order of skills in *Mario Kart Wii*: (me), Cipo, Bob, Agno, Sibo, Pelipe, Yugi, Hectov (in particular for the help), Pede, Pilo, Cate. Thank you to my friends I did not mention, in particular Fra Villa who told me: but you should do it. Thank you to my brother, who is close to me. Thank you to my father, who taught me how to be strong. Thank you to my mother, who taught me how to love. Thank you to the combination of all of the above, which taught me that there is no room for hate.

---

[1] *My first broken pencil.*

[2] In writing this text the first time, I forgot to thank my computer as well, for the billion times I pressed its buttons during this Thesis.

[3] Who also suggested me the quote by Kekulé of Chapter 4.

Table of contents

1 Introduction **23**

1.1 Outline of the Thesis 29

2 Methods **31**

2.1 Quantum mechanics of a molecule 31

Molecular Schrödinger equation 31

Born-Oppenheimer approximation 32

Hellmann-Feynman theorem 32

Harmonic approximation 33

Classical vibrations of a polyatomic molecule 33

Quantum vibrations of a polyatomic molecule 33

2.2 Quantum mechanics of a crystal 34

Translational symmetry 34

Bloch theorem 34

Born-von Kármán boundary conditions 35

2.3 Density functional theory 36

Stationary theory 36

Time-dependent theory 37

2.4 Computational tools 38

3 N2200 **41**

3.1 The computational model 42

3.2 Results and discussion 46

3.3 Chapter conclusions 60

4 Functionalized graphene nanoribbons **63**

4.1 The computational model 64

4.2 Results and discussion - IR 68

4.3 Results and discussion - UV-Vis 77

4.4 Results and discussion - Raman 79

4.5 Chapter conclusions 84

5 PVDF **87**

5.1 The computational model 87
5.2 Model performance 91
5.3 Chemical defect 96
5.4 Conformational defect 103
5.5 Solid-state effects in PVDF 105
5.6 Chapter conclusions 111

6 Conclusion **113**

List of figures

1.1 Number of citations per year to one or both the seminal papers of DFT (Refs. [4] and [5]). Data from the Web of Science. Reproduced from Ref. [6]. 24

1.2 Incorporation of $\pi-$conjugation and redox sites in the same polymer as a way of enhancing electronic conductivity. (a) Illustration of electron transport in a $\pi-$conjugated polymer (top left) and in a redox polymer (bottom left), together with the incorporation of both these properties in the same polymer (right). (b) Molecular structures of P(NDI2OD-TET), a redox polymer lacking $\pi-$conjugation, and P(NDI2OD-T2), the n-dopable $\pi-$conjugated redox polymer studied in Chapter 3. Reproduced from Ref. [7]. 26

1.3 Three edge morphologies of GNRs. Zigzag-edged GNRs are metallic, whereas armchair- and cove-edged GNRs can be either semiconductive or metallic depending on their width and edge functionalization. Reproduced from Ref. [8]. 27

1.4 (a) Conformations of different phases of PVDF: α and δ phases (top), β phase (middle) and γ phase (bottom). (b) Origin of the non-zero electric dipole in the β phase of PVDF. (c) Arrangement of PVDF macromolecules in their β phase in a three-dimensional crystal. Panels (a) and (c) are reproduced from Ref. [9], while panel (b) comes from Ref. [10]. 28

3.1 From bottom to top: IR spectra of pristine N2200, doped N2200 at increasing dopant/polymer ratio MR and pristine dopant DPhBI. The latter is a molecular dopant with a relatively complex structure, not taken into account in this Chapter. Asterisks label the features induced by doping, and indicate therefore polaron markers. Reproduced from Ref. [1]. 41

3.2 From bottom to top: Raman spectra of pristine N2200, doped N2200 at increasing dopant/polymer ratio MR and pristine dopant DPhBI. The latter is a molecular dopant with a relatively complex structure, not taken into account in this Chapter. Asterisks label the features induced by doping, and indicate therefore polaron markers. Reproduced from Ref. [1]. 42

3.3 (a) Structural formula of N2200. (b) Molecular model of undoped N2200. . . 43

3.4 Molecular models of doped N2200. 44

3.5 One-dimensional periodic models of N2200. 45

3.6 Representation of the energies of the FMOs of **1**, $\mathbf{1^-}$ and $\mathbf{1^-Li^+}$. 46

3.7 Isosurfaces of the FMOs of different molecular models of N2200. The FMOs are positive in yellow regions, negative in blue regions. Isosurfaces have been taken at `0.006` $a_0^{-3/2}$. Black arrows indicate the main differences observed in the three isosurfaces. 47

3.8 Artificial covalent bond between lithium and a sulfur atom in the $\mathbf{1^{-}Li^{+}}$ model. The labeled atoms define the dihedral angle Li−O−C−C, τ. 48

3.9 Total energy of the $\mathbf{1^{-}Li^{+}}$ model as a function of the Li−O−C−C dihedral angle τ. For the estimation of the thermal energy, $T = 298\,\mathrm{K}$ has been considered. 48

3.10 Labeling scheme of the atoms taken into account in the NBO analysis of Tables 3.2 and 3.3. The atoms omitted in such analysis are not represented as spheres. 49

3.11 Particular of the isosurface of the SOMO of $\mathbf{1^{-}Li^{+}}$, showing its bilobed shape near the lithium atom. The SOMO is positive in yellow regions, negative in blue regions. The isosurface has been taken at `0.006` $a_0^{-3/2}$. 51

3.12 Isosurface of the spin density of $\mathbf{1^{-}Li^{+}}$. The spin density is positive in yellow regions, negative in blue regions. The isosurface has been taken at `0.001` a_0^{-3}. 52

3.13 Bondplot of $\mathbf{1^{-}Li^{+}}$: bond-length differences between $\mathbf{1^{-}Li^{+}}$ and **1**. This plot has the same orientation as in Figure 3.12, so that the asterisk indicates the lithiation site. Differences are reported in pm. Only differences whose absolute value is equal to or larger than 0.1 pm are shown. Bond-length variations are positive in red regions, negative in blue regions. 53

3.14 Bondplot of $\mathbf{1^{-}}$: bond-length differences between $\mathbf{1^{-}}$ and **1**. Differences are reported in pm. Only differences whose absolute value is equal to or larger than 0.1 pm are shown. Bond-length variations are positive in red regions, negative in blue regions. 54

3.15 Labeling of the dihedral angles taken as a rough measure for the conjugation in the molecular models of doped N2200 in Table 3.4. Only atoms defining the dihedral angles and lithium are represented as spheres. 55

3.16 Isosurface of the electron-density difference between $\mathbf{1^{-}}$ and $\mathbf{1^{-}}$ in the geometry of **1**. The electron-density difference is positive in yellow regions, negative in blue regions. The isosurface has been taken at `0.001` a_0^{-3}. Inset: representation of the transformation associated with this electron-density difference. In particular, we are concerned with the transformation with energy variation $\mathrm{E_{IP-V}}$, from the ground state to the ionized state. Reproduced from Ref. [11]. 57

3.17 Bondplot of a portion of $\mathbf{1^{-}Li^{+}}$–PBC: bond-length differences between $\mathbf{1^{-}Li^{+}}$–PBC and **1**–PBC. In this plot, the asterisk indicates the lithiation site. Differences are reported in pm. Only differences whose absolute value is equal to or larger than 0.1 pm are shown. Inset: portion of Figure 3.13, where the bondplot of $\mathbf{1^{-}Li^{+}}$ is shown. 58

3.18 (a, b, c) Bondplots of molecular models of N2200 with different alkali metals as n-doping agents: bond-length differences between n-doped models and **1**. In these plots, asterisks indicate the attachment sites of alkali metals. Differences are reported in pm. Only differences whose absolute value is equal to or larger than 0.1 pm are shown. (d) Bond-length difference Δ of the C−O bond in the lithiation site at different ionic radii. 59

4.1 Schematic representation of the RBLM of a GNR. Reproduced from Ref. [12]. 63

4.2 Molecular models of fully hydrogenated GNRs. 65

4.3 Molecular model of a GNR functionalized with A and OM, and their structural formulae. In panel (a) the substituents are indicated. In panels (b) and (c) asterisks indicate the attaching sites. 66

4.4 Molecular and periodic models of GNRs functionalized with A groups. In panel (d), a repeat unit of GNR–A–PBC is represented. 67

4.5 Experimental IR spectrum of GNR–AOM (courtesy of Dr. Junzhi Liu, The University of Hong Kong). The most intense bands are labelled with their corresponding wavenumbers in cm^{-1}. 68

4.6 Left: simulated IR spectra of hydrogenated oligomers of GNRs. Three most intense simulated bands are labelled with their corresponding wavenumbers in cm^{-1}. Spectra are normalized on their maximum intensity in the represented interval. Top right: wavenumber dispersion of the most intense computed IR bands with respect to the length of the molecular models. Bottom right: ratio between the intensities of the two bands at $\sim 792\,\mathrm{cm}^{-1}$ and $\sim 755\,\mathrm{cm}^{-1}$ at different lengths of the molecular models. 69

4.7 Simulated IR spectrum of [4]GNR–[4]A[4]OM compared with the experimental IR spectrum of GNR–AOM (courtesy of Dr. Junzhi Liu, The University of Hong Kong). Dotted lines highlight the assignment of the most prominent IR features. In both spectra, the most intense features are labelled with their wavenumber in cm^{-1}. Spectra are normalized on their maximum intensity in the represented interval. 73

4.8 Simulated IR spectra of models of GNRs functionalized with A groups compared with the experimental IR spectrum of GNR–AOM (courtesy of Dr. Junzhi Liu, The University of Hong Kong). In the spectra of GNR–AOM and GNR–A–PBC, the most intense features are labelled with their wavenumber in cm^{-1}. Dashed grey lines help to visualize the dispersion of some features with respect to the length of the model. Spectra are normalized on their maximum intensity in the represented interval. 77

4.9 (a) Experimental UV-Vis spectrum of GNR–AOM (courtesy of Dr. Junzhi Liu, The University of Hong Kong). (b) Simulated UV-Vis spectra of [n]GNR–H and [4]GNR–[4]A[4]OM models. (c) Dispersion of the peak at 549 nm in [13]GNR–H. (d-g) Isosurfaces of the FMOs of [4]GNR–[4]A[4]OM involved in the electronic transitions associated with the most prominent peaks of its UV-Vis spectrum. The FMOs are positive in yellow regions, negative in blue regions. Isosurfaces have been taken at $\texttt{0.005}\, a_0^{-3/2}$. In the UV-Vis spectra, the most intense features are labelled with their wavelength in nm. In particular, a dashed line helps to visualize the shoulder of the UV-Vis spectrum of [13]GNR–H. 78

4.10 Left: simulated Raman spectra of hydrogenated oligomers of GNRs and experimental Raman spectrum of GNR–AOM (courtesy of Dr. Junzhi Liu, The University of Hong Kong). The D and G peaks of the experimental spectrum are labelled with their corresponding wavenumbers in cm^{-1}. Spectra are normalized on the intensity of the D peak. Right: wavenumber dispersion of the computed D peak with respect to the length of the molecular models. 80

4.11 Simulated Raman spectrum of [4]GNR–[4]A[4]OM compared with the experimental Raman spectrum of GNR–AOM (courtesy of Dr. Junzhi Liu, The University of Hong Kong). The D and G peaks of the experimental spectrum are labelled with their corresponding wavenumbers in cm^{-1}. Spectra are normalized on the intensity of the D peak. 83

4.12 From top to bottom: experimental Raman spectrum of GNR–AOM (courtesy of Dr. Junzhi Liu, The University of Hong Kong), simulated Raman spectra of [6]GNR–H, [n]GNR–H models with $n = 5, 4, 3$, and [4]GNR–[4]A[4]OM. The RBLM features of GNR–AOM and [6]GNR–H are labelled with their corresponding wavenumbers in cm^{-1}. All spectra except those of [n]GNR–H models are normalized with respect to the most intense feature of the represented interval. The spectra of [n]GNR–H models are normalized with respect to the intensity of the RBLM feature of [6]GNR–H. 84

5.1 Equilibrium geometries of molecular models of PVDF and P(VDF−TrFE). . . 88

5.2 Equilibrium geometries of one-dimensional periodic models of PVDF and P(VDF−TrFE). In panel (a) a portion with five repeat units of VDF−1D is represented, while panel (b) shows the repeat unit of P(VDF−TrFE). 89

5.3 Equilibrium geometries of cluster models of PVDF. In both panels, portions with five repeat units are shown. In panel (b), crossed atoms are assigned a mass $m = 1000\,\mathrm{amu}$. 90

5.4 Equilibrium geometries of three-dimensional periodic models of PVDF and P(VDF−TrFE). In both panels, portions with seven repeat units are shown. . 91

5.5 Equilibrium geometry of 9−VDF−1−TrFE−**m**. Crossed atoms are assigned a mass $m = 1000$ amu. 91

5.6 Study of the performance of oligomeric models of PVDF. IR spectra of n−VDF with $n = 2, 4, 6, 8, 10, 20, 30$. In both panels, IR intensities are normalized to n. In panel (b) terminal bands are indicated with T. 92

5.7 Study of the performance of oligomeric models of PVDF. Raman spectra of n−VDF with $n = 2, 4, 6, 8, 10, 20, 30$. In both panels, Raman activities are normalized to n. In panel (b) a terminal band is indicated with T. 93

5.8 Study of the performance of oligomeric models of P(VDF−TrFE). IR (a) and Raman (b) spectra of n−VDF−m−TrFE, with $n = 9, 18, 27$. IR intensities and Raman activities are normalized to $(10/9)n$. 94

5.9 Comparison between IR and Raman spectra of molecular and one-dimensional periodic models of PVDF (a, b) and P(VDF−TrFE) (c, d). In all panels, IR intensities and Raman activities have been normalized on the number of CH_2CF_2 or $CHCF_3$ units either in the molecule or in the repeat unit. 95

5.10 IR vibrational markers of the chemical defect in molecular models. (a) IR spectra of P(VDF−TrFE), 10−VDF and 9−VDF−1−TrFE, where asterisks indicate experimental and computed vibrational markers of the TrFE unit. The maximum IR intensities are normalized to 1 in the represented interval. The experimental IR spectrum is reproduced from Ref. [2]. (b, c) Vibrational normal modes of 9−VDF−1−TrFE corresponding to the computed vibrational markers of the TrFE unit. 97

5.11 IR vibrational markers of the chemical defect in molecular models. IR spectra of 9−VDF−1−TrFE and 9−VDF−1−TrFE−**m**. The maximum IR intensities are normalized to 1. 98

5.12 IR vibrational markers of the chemical defect in periodic models. (a) IR spectra of 10−VDF, 9−VDF−1−TrFE and VDF−TrFE−1D. Asterisks indicate the computed vibrational markers of the chemical defect. IR intensities are normalized on the number of CH_2CF_2 or $CHCF_3$ units either in the molecule or in the repeat unit. (b) IR spectra of P(VDF−TrFE), VDF−3D and VDF−TrFE−3D. The maximum IR intensities are normalized to 1. 99

5.13 Raman vibrational markers of the chemical defect in molecular models. Raman spectra of P(VDF−TrFE), 10−VDF and 9−VDF−1−TrFE. The maximum Raman activities are normalized to 1 in the represented interval. The experimental Raman spectrum is reproduced from Ref. [2]. 101

5.14 Raman vibrational markers of the chemical defect in molecular models. (a) Raman spectra of 9−VDF−1−TrFE and 9−VDF−1−TrFE−**m**, with their maxima normalized to 1 in the represented interval. (b) IR and Raman spectra of 9−VDF−1−TrFE−**m** with their maxima normalized to 1 in the represented interval. 101
5.15 Raman vibrational markers of the chemical defect in periodic models. (a) Raman spectra of VDF−1D, 9−VDF−1−TrFE and VDF−TrFE−1D. (b) Raman spectra of VDF−3D and VDF−TrFE−3D. In both panels, asterisks indicate the computed vibrational markers of the chemical defect, and Raman activities are normalized on the number of CH_2CF_2 or $CHCF_3$ either in the molecule or in the repeat unit. 102
5.16 (a) IR vibrational marker of the conformational defect in molecular models. IR spectra of 10−VDF, 20−VDF, 10−VDF−1−GTG' and 20−VDF−2−GTG'. IR intensities are normalized on the number of CH_2CF_2 repeat units. (b) IR spectrum of P(VDF−TrFE) films, reproduced from Ref. [2]. IR intensities are normalized to 1 in the represented interval. 103
5.17 Raman vibrational marker of the conformational defect in molecular models. (a) Raman spectra of 10−VDF, 20−VDF, 10−VDF−1−GTG' and 20−VDF−2−GTG'. Raman activities are normalized on the number CH_2CF_2 repeat units. (b) Raman of P(VDF−TrFE) fibers, reproduced from Ref. [2]. Raman intensities are normalized to 1. 105
5.18 Solid-state effects on the IR and Raman responses of PVDF. (a) IR spectra of VDF−1D and VDF−3D. (b) Raman spectra of VDF−1D and VDF−3D. 106
5.19 Solid-state effects on the IR and Raman responses of PVDF. (a) IR spectra of VDF−1D, 2−VDF−1D, 3−VDF−1D−**m**, VDF−2D and VDF−3D. (b) Raman spectra of VDF−1D, 2−VDF−1D, 3−VDF−1D−**m**, VDF−2D and VDF−3D. . . 108
5.20 IR and Raman spectra of VDF−3D at different extents of isotropic expansion. In both spectra, the key reports the values of $a/a_0 = b/b_0$, where the cell parameters a and b correspond to directions orthogonal to the PVDF chain axis and 0 indicates their equilibrium values. 110
5.21 IR and Raman spectra of VDF−3D at different extents of anisotropic expansion. In both spectra, the key reports the values of a/a_0, where the cell parameter a corresponds to a direction orthogonal to the PVDF chain axis and 0 indicates its equilibrium value. 110

List of tables

3.1 Energies of FMOs and energy gaps E_g of different molecular models of N2200. 46

3.2 NBO analysis of the $\mathbf{1^-Li^+}$ model: occupancies of the first nine natural orbitals of lithium. The atomic label is defined in Figure 3.10b. C, V, and R stand respectively for core, valence, and Rydberg natural atomic orbitals. 50

3.3 NBO analyses of $\mathbf{1}$ and $\mathbf{1^-Li^+}$: natural charges of some atoms and rings. Atomic labels are defined in Figure 3.10. Tn, with $n = 1, 2, 3, 4$, labels the thiophene ring containing the atom Sn. Natural charges are called q in this Table. Natural charges for the thiophene rings have been obtained summing the natural atomic charges of all the hydrogen, carbon and sulphur atoms of each ring. The last column reports the variations $\Delta = q(\mathbf{1^-Li^+}) - q(\mathbf{1})$ of natural charges from $\mathbf{1}$ to $\mathbf{1^-Li^+}$. Data of corresponding atoms or rings are on the same row. 50

3.4 Values of some dihedral angles α in $\mathbf{1^-}$ and $\mathbf{1^-Li^+}$. Atomic labels are defined in Figure 3.15. Here we use $\min|n\pi - \alpha|$, with $n \in \mathbb{Z}$, as a measure of the non-planarity of the dihedral angle α. We have $\min|n\pi - \alpha| \approx \varphi$, where φ is the angle formed by the normals to the planes onto which NDI and thiophene units can be thought to lay, approximately. The last column reports the variation Δ of this measure from $\mathbf{1^-}$ to $\mathbf{1^-Li^+}$. 56

4.1 Vibrational normal modes associated with the most intense features of the IR spectrum of [6]GNR–H. The last column represents the atomic displacements at a given instant of time of the vibration. Blue and green segments symbolize stretching and shortening bonds. 71

4.2 Assignment of the experimental IR spectrum of GNR–AOM. 72

4.3 Vibrational normal modes associated with the most intense features of the IR spectrum of [4]GNR–[4]A[4]OM. The last column represents the atomic displacements at a given instant of time of the vibration. 75

4.4 Analysis of the electronic excitations associated with the UV-Vis features at 472 nm and 549 nm in the simulated spectrum of [13]GNR–H of Figure 4.9b. . 79

4.5 Vibrational normal modes associated with the D and G peaks of [6]GNR–H. The last column represents the atomic displacements at a given instant of time of the vibration. Blue and green segments symbolize stretching and shortening bonds. 81

4.6 Vibrational normal modes associated with the D and G peaks of [4]GNR–[4]A[4]OM. The last column represents the atomic displacements at a given instant of time of the vibration. Blue and green segments symbolize stretching and shortening bonds. 82

5.1 IR vibrational markers of the unit TrFE in different molecular and periodic models. In the last column, the localization of the vibrational normal mode in the chemical defect is understood. 100
5.2 Raman vibrational markers of the chemical-defective unit TrFE in different molecular and periodic models. In the last column, the localization of the vibrational normal mode in the chemical defect is understood. 100
5.3 Vibrational normal modes corresponding to the low-wavenumber component of the band at 850 cm^{-1} of the IR spectrum of 10−VDF−1−GTG', represented in Figure 5.16a. 104
5.4 Raman vibrational markers of the chemical-defective unit TrFE in different molecular and periodic models. In the last column, the localization of the vibrational normal mode in the chemical defect is understood. 105
5.5 Assignment of the IR and Raman spectra of VDF−1D and VDF−3D shown in Figure 5.18. IR intensities are reported in km/mol, Raman activities in $\mathrm{\AA}^2/\mathrm{amu}^{1/2}$. 107
5.6 Solid-state effects on two vibrational features in the region between 850 cm^{-1} and 1000 cm^{-1} in periodic models of PVDF. 109

Chapter 1

Introduction

I am not accustomed to saying anything with certainty
after only one or two observations.

— Andreas Vesalius

Experimental observations are crucial for the comprehension of natural phenomena. The total amount of scientific knowledge increases as more experiments are done, each of them being capable of falsifying previous beliefs. Incidentally, the existence of this latter possibility is a characteristic of any physical theory, in the view of the philosopher of science Karl Popper [13]. Then a general understanding of a given phenomenon requires it to be attacked on several fronts. One may recall Galilei's view of scientific investigation, according to which [14]:

> [...] in the discussions of physical problems we ought to begin [...] from sense-experiences and necessary demonstrations.

Coupled with the quantum nature of matter at the atomic scale [15], these necessary demonstrations acquire a quantum many-body character. As long as more than few particles are considered, this is known to be a practically unsolvable problem [16]. Nevertheless, several brilliant interpretations of the behavior of matter have been given in the past without explicitly referring to the inherent many-body problem. Of these, the kinetic theory of gases is an example, where temperature is connected with the average square velocity of molecules [17].

In 1927-1928, a model by Llewellyn Thomas and Enrico Fermi proved that the total energy of a Fermi gas interacting with a positive nucleus is captured approximately by a functional of the only electronic density [18, 19, 20]. One of the important limitations of this model is that it does not account for chemical bonding [21]. Nevertheless, the Thomas-Fermi model has been considered as a precursor [22] when in 1964-1965 density functional theory (DFT) was formulated in the seminal papers of Pierre Hohenberg, Walter Kohn and Lu Jeu Sham [4, 5]. As will be reviewed in Chapter 2, DFT is a reformulation of quantum mechanics that allows to exactly express the ground-state energy of a quantum system as a functional of the three-dimensional electronic density, removing the need to refer to the more complex wave function [22]. This simplification has made DFT the most popular method for computing the electronic structure of systems [6], starting with the physics community in 1965 and landing among chemical-physicists in the mid-1980s. [23].

Figure 1.1 reports the number of citations per year to one or both the seminal papers of DFT (Refs. [4] and [5]). It shows that the interest in DFT exploded in time. Today, those papers are among the most cited ones in *Physical Review*. [6]. For his development of DFT, Walter Kohn shared the Nobel prize in Chemistry in 1998. The other half was awarded to John Pople, who developed important computational methods, also applied in this Thesis, as will be mentioned in Chapter 2.

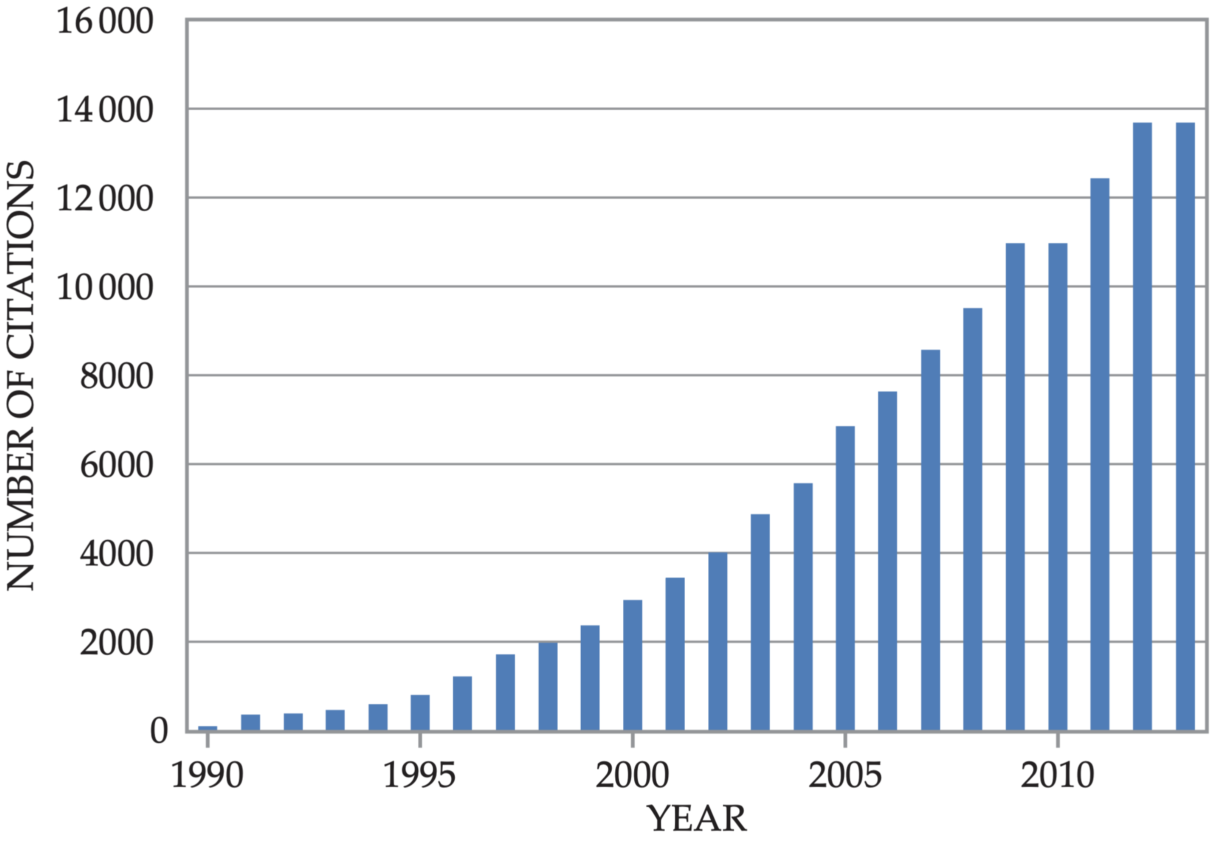

Figure 1.1: Number of citations per year to one or both the seminal papers of DFT (Refs. [4] and [5]). Data from the Web of Science. Reproduced from Ref. [6].

It is therefore expected that DFT finds space in several applications. Indeed, there exists a large portion of literature where density functional methods are applied to very different problems. Starting from its historical first application in materials science of 1980, where the phase and lattice stability of silicon were studied [24], DFT was also applied to explain the puzzling properties of the lowermost portion of the mantle of Earth [25], to predict the formation energy of transition-metal alloys [26], and to determine the exchange integrals of Heisenberg models, allowing an *ab initio* description of magnetism [27]. One particular case puts in evidence the predictive power of DFT: in 2010-2013, a new Fe-B superconducting compound was first computationally predicted [28] and then experimentally discovered [29].

In this Thesis, we will be concerned with the application of DFT to the study of vibrational properties of advanced materials. These are complex systems, for which the comprehension of the physical mechanisms underlying their macroscopic properties requires the insight of theoretical calculations. Two classes of advanced materials will be considered in the following Chapters, namely $\pi-$conjugated and ferroelectric polymers. We will refer in particular to three materials, which are introduced in the following.

The $\pi-$conjugated polymer N2200. Since the discovery of conductive polyacetylene in 1977 [30], which led Hideki Shirakawa, Alan MacDiarmid and Alan Heeger to share the Nobel Prize in Chemistry in 2000, conductive polymers constitute a research topic of increasing interest. Such materials allow indeed for the realization of organic-based opto-electronic devices, which in turn are characterized, when compared to silicon-based technologies, by far lower costs and novel functionalities. From these applications of polymers, new device properties arise, such as mechanical flexibility, impact resistance, optical transparency, and light weight [31]. Although both hole- (p-type) and electron-transporting (n-type) polymers are known, the instability of the latter hinders the development of all-polymer devices [32, 33]. There is therefore a need for the enhancement of the transport properties of n-type polymers, of which P(NDI2OD-T2), briefly referred to as N2200, is a promising instance [34, 35].

Two general classes of n-type polymers can be identified, namely $\pi-$conjugated polymers and redox polymers. In $\pi-$conjugated polymers, the superposition of p atomic orbitals results in electron delocalization along the backbone of the molecule. This favors electron transport in the presence of an external applied voltage. However, $\pi-$conjugated polymers often need several repeat units to stabilize the injected electronic charge, this resulting in poor electronic conductivity. On the other hand, redox polymers are characterized by the presence of redox sites capable of accepting one or more electrons per repeat unit. However, they lack in general $\pi-$conjugation, in the absence of which electrical conductivity is compromised [7, 36].

Both the problems exposed above are solved incorporating $\pi-$conjugation and redox sites in the same polymer. This is the case of N2200, which is thus termed as an n-dopable $\pi-$conjugated redox polymer [7]. Figure 1.2 offers a visual representation of the combination of properties just described, together with the molecular structure of N2200. Given the essential role of polaron as charge carrier in N2200 [37, 38], we investigated by DFT calculations the polaron structure and the associated molecular structure relaxation.

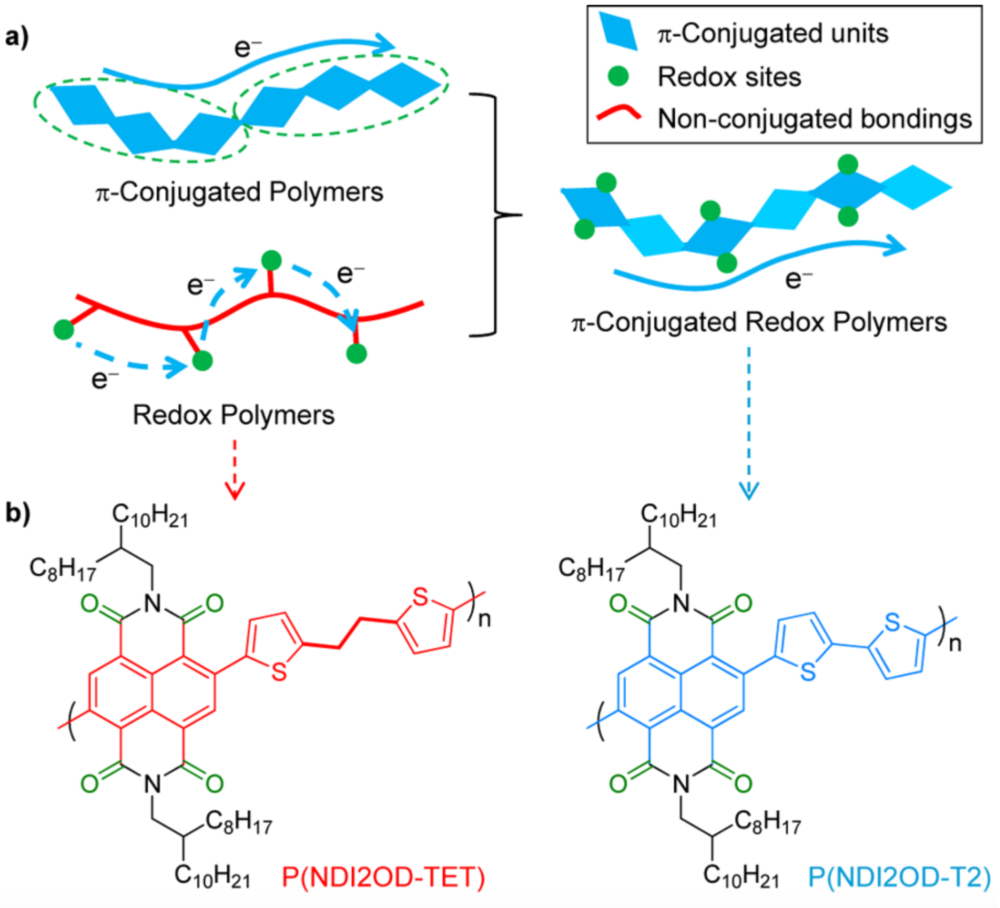

Figure 1.2: Incorporation of $\pi-$conjugation and redox sites in the same polymer as a way of enhancing electronic conductivity. (a) Illustration of electron transport in a $\pi-$conjugated polymer (top left) and in a redox polymer (bottom left), together with the incorporation of both these properties in the same polymer (right). (b) Molecular structures of P(NDI2OD-TET), a redox polymer lacking $\pi-$conjugation, and P(NDI2OD-T2), the n-dopable $\pi-$conjugated redox polymer studied in Chapter 3. Reproduced from Ref. [7].

Functionalized graphene nanoribbons. In 2010, the Nobel Prize in Physics was awarded to Konstantin Novoselov and Andrej Geim for their breakthrough experiments on graphene, a single atomic layer of carbon, where electrons behave as two-dimensional [39]. In addition to other remarkable properties, graphene has a particular electronic behavior in being a zero-gap semiconductor [40]. However, from the point of view of the realization of carbon-based nanoelectronics, not always this latter property is wanted, because it hinders the existence of ON and OFF states. This problem is solved if one considers to cut an infinite graphene sheet along vertical lines, so as to obtain a narrow ribbon. Such structure has the general name of graphene nanoribbon (GNR), and was studied from a theoretical point of view by Mitsutaka Fujita and coworkers in 1996 [41, 42]. They showed that, as opposed to the case of graphene, the bandgap of GNRs depends on their width and edge morphology. Based on the orientation of the cut by which GNRs are ideally derived from graphene, three classes of edge morphologies can be obtained, as represented in Figure 1.3. In particular, zigzag-edged GNRs are found to be metallic, whereas armchair- and cove-edged GNRs can be either semiconductive or metallic depending on their width and edge functionalization [8, 43].

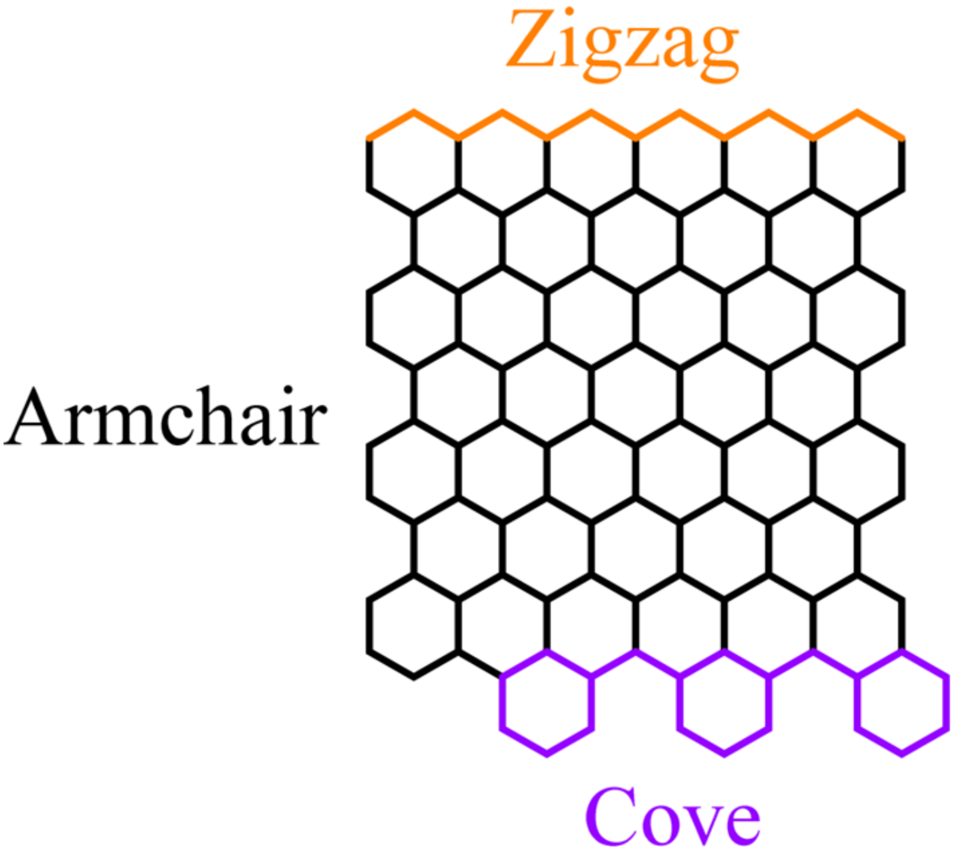

Figure 1.3: Three edge morphologies of GNRs. Zigzag-edged GNRs are metallic, whereas armchair- and cove-edged GNRs can be either semiconductive or metallic depending on their width and edge functionalization. Reproduced from Ref. [8].

Due to this tunability of their electronic properties, a valid alternative to conjugated polymers for organic nanoelectronics is given by GNRs, which are applied, for example, in the design of organic field-effect transistors [44]. As expected from the chemical structure of Figure 1.3, however, $\pi - \pi$ interactions hinder the processability of GNRs in solution, so that bulky substituents are usually applied in order to prevent stacking. Chemical synthesis is the preferred way to achieve GNRs production, since top-down techniques such as lithography usually fail in giving GNRs with nanometric and narrowly-distributed widths. There thus exists a need for the assessment of a correct edge functionalization of GNRs. DFT calculations and experimental characterization by spectroscopy can provide the identification of the spectral markers associated to the functional groups introduced by chemical synthesis.

The piezoelectric polymer P(VDF-TrFE). As discovered in 1969 by Heiji Kawai, the ferroelectric polymer polyvinylidene fluoride (PVDF) possesses piezoelectric properties, where mechanical stress causes a variation of electric polarization and *vice versa* [45, 10]. The

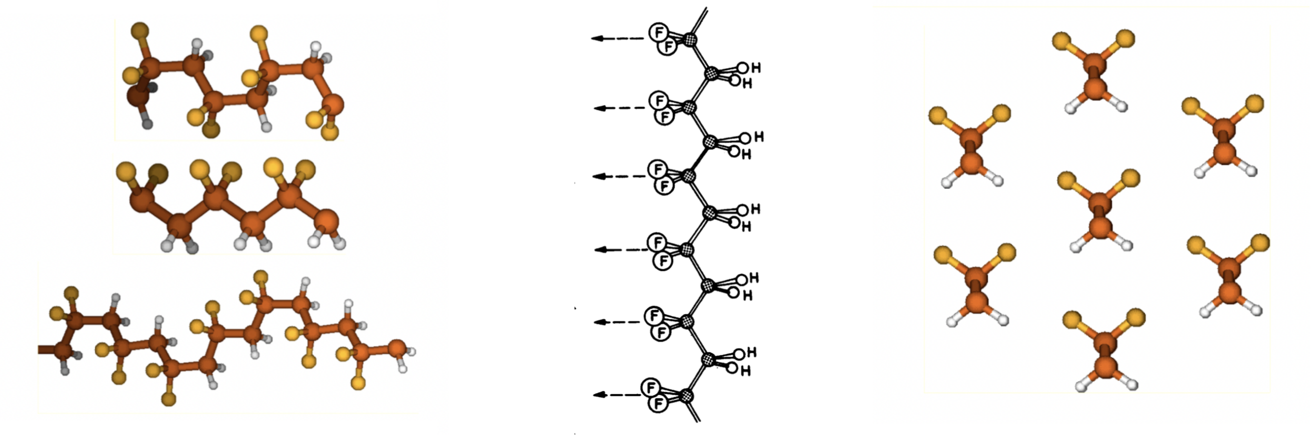

(a) (b) (c)

Figure 1.4: (a) Conformations of different phases of PVDF: α and δ phases (top), β phase (middle) and γ phase (bottom). (b) Origin of the non-zero electric dipole in the β phase of PVDF. (c) Arrangement of PVDF macromolecules in their β phase in a three-dimensional crystal. Panels (a) and (c) are reproduced from Ref. [9], while panel (b) comes from Ref. [10].

interest in piezoelectric polymers derives from the fact that other piezoelectric materials such as zinc oxide are brittle, and must be processed at high temperature. This constitutes an important limitation to their applications, of which energy harvesting and sensoring are some instances. Polymers, on the contrary, are generally known to lack both brittleness and high processing temperatures. This is a substantial advantage when polymers are applied as piezoelectric materials, in addition to the fact that new design possibilities may also arise, such as the realization of flexible components [2, 46].

A portion of a macromolecule of PVDF in its β phase is illustrated in the middle of Figure 1.4a. It is characterized by an all-trans planar zig-zag chain conformation, where carbon atoms lay on the same plane. As highlighted by Figure 1.4b, this conformation leads to the presence of a non-zero electric dipole moment oriented orthogonal to the chain axis. The β phase of PVDF is therefore polar, and packs in an orthorhombic crystal system as in Figure 1.4c.

The non-polar α phase of PVDF is represented in the top of Figure 1.4a for the conformation of a single molecule. This is the most thermodynamically stable phase of PVDF [2]. Therefore, in the crystallization from the polymer melt, this non-polar conformation of the polymer is obtained. Taking into account the interest in piezoelectric polymers, the spontaneous obtainment of the piezoelectric β phase during crystallization is wanted. This is the case of the random copolymer poly (vinylidene fluoride-co-trifluoroethylene) (P(VDF−TrFE)), which is characterized by the random alternation of VDF and TrFE units [47]. Apart from its piezoelectric β phase, no other phases of P(VDF−TrFE) have been observed [48], so that the inclusion of TrFE units in PVDF to give P(VDF−TrFE) results in the spontaneous obtainment of a piezoelectric phase from the polymer melt.

1.1 Outline of the Thesis

Vibrational properties of materials have been previously studied by means of DFT by several authors, both for IR and Raman [49, 50, 51, 52]. However, gaps in the literature still exist for what concerns the three advanced materials exposed above. In this Thesis, we will be thus interested in the application of DFT to the study of their vibrational properties, considering both molecular and periodic models in different dimensions. We want to show that DFT is a powerful analytical tool for the prediction and corroboration of experimental results obtained by means of vibrational spectroscopy. In doing so, we will also assess the validity of DFT in the necessary approximations that allow it to be implemented in computer codes with accessible computation times. In particular, after the brief theoretical review of Chapter 2:

- In Chapter 3 we use DFT to show that the lithiation of N2200 results in the confinement of structural relaxation. This phenomenon, called polaron localization, has been recently unveiled by vibrational spectroscopy [1]. However, DFT models used in [1] were not taking into consideration the dopant explicitly. The discussion is then extended to different atomic n-dopants, of which the electrostatic effect on charge delocalization is studied.

- In Chapter 4 the successful synthesis of functionalized graphene nanoribbons [53] is supported by simulating their IR, Raman and UV-Vis spectra.

- In Chapter 5 we compute the vibrational spectra of the two piezoelectric polymers $\beta-$PVDF and P(VDF−TrFE) and find vibrational markers for both the TrFE chemical unit and conformational disorder. This supports the results of Arrigoni *et al.* [2], who made a spectroscopic study of electrospun P(VDF−TrFE) nanoifbers, and allows us to study solid-state effects on the IR and Raman spectra of PVDF.

Chapter 2

Methods

> *[...] the question occurred to [me] whether a knowledge of $n(\mathbf{r})$ alone determined - at least in principle - the total energy.*
>
> — Walter Kohn

In this Thesis, materials are modeled either as molecules or crystals. We here introduce some general results of the quantum theories of these two systems. With that in mind, the principles of density functional theory are then exposed.

2.1 Quantum mechanics of a molecule

We begin with recalling the quantum description of a molecule, following Atkins [54]. This will also serve to introduce important approximations, which are retained in the whole Chapter.

Molecular Schrödinger equation

Let us consider a system of N electrons and M nuclei, and indicate with $\mathbf{r}$ and $\mathbf{R}$ the collection of electronic and nuclear coordinates, respectively. The stationary states of such system are described by the wavefunctions ψ that solve the time-independent Schrödinger equation,

$$H\psi = E\psi,$$

with eigenvalue E, where H is the molecular Hamiltonian. The latter is a sum of kinetic and potential energy operators:

$$H = T_{\mathrm{e}} + T_{\mathrm{n}} + V_{\mathrm{ee}} + V_{\mathrm{en}} + V_{\mathrm{nn}},$$

where the subscripts indicate electrons and nuclei. Jordan quantization rules allow to write these operators starting from their classical counterparts. The kinetic energy operators are then

$$T_\mathrm{e} = \sum_{i=1}^{N} -\frac{\hbar^2}{2m}\nabla_i^2, \qquad\qquad T_\mathrm{n} = \sum_{I=1}^{M} -\frac{\hbar^2}{2M_I}\nabla_I^2,$$

whereas electrostatic potential energy operators write

$$V_\mathrm{ee} = \frac{e^2}{4\pi\varepsilon_0}\sum_{i<j}\frac{1}{|\mathbf{r}_i - \mathbf{r}_j|}, \quad V_\mathrm{en} = -\frac{e^2}{4\pi\varepsilon_0}\sum_{i,I}\frac{Z_I}{|\mathbf{r}_i - \mathbf{R}_I|}, \quad V_\mathrm{nn} = \frac{e^2}{4\pi\varepsilon_0}\sum_{I<J}\frac{Z_I Z_J}{|\mathbf{r}_i - \mathbf{r}_j|}.$$

V_ee cannot be factorized as a sum of one-particle contributions. This already points out the difficulty set by electron correlation.

Born-Oppenheimer approximation

The quantum description of a molecule can be simplified observing that $m_\mathrm{p}/m_\mathrm{e} \approx 2000$. This means $v_\mathrm{e} \gg v_\mathrm{p}$, and it is therefore reasonable to consider the nuclear configuration as a fixed parameter of the instantaneous electronic motion. In other words, electronic and nuclear degrees of freedom can be decoupled, and the molecular wavefunction can be written as a product of an electronic wavefunction ψ_e and a nuclear wavefunction ϕ_n:

$$\psi(\mathbf{r}, \mathbf{R}) = \psi_\mathrm{e}(\mathbf{r}|\mathbf{R})\phi_\mathrm{n}(\mathbf{R}).$$

By definition, ψ_e is eigenfunction of the electronic Hamiltonian $H_\mathrm{e} = T_\mathrm{e} + V_\mathrm{en} + V_\mathrm{ee}$ with eigenvalue ε_e. Then, it is found that ϕ_n is eigenfunction of an effective nuclear Hamiltonian $H_\mathrm{n} = T_\mathrm{n} + V_\mathrm{nn} + \varepsilon_\mathrm{e}$. This is called the Born-Oppenheimer or adiabatic approximation, and constitutes the usual context in which the structure and dynamics of molecules and crystals are discussed.

Hellmann-Feynman theorem

If we now call $U = \langle\psi|H|\psi\rangle$ the energy of the system and consider the generic parameter λ, we can prove [55] that in stationary conditions

$$\frac{\partial U}{\partial \lambda} = \left\langle \psi \middle| \frac{\partial H}{\partial \lambda} \middle| \psi \right\rangle.$$

This result defines the force $-f_\lambda$ equivalently as the derivative of the energy and the expectation value of the derivative of the Hamiltonian. A particular case is obtained for $\lambda = X_\mu^\alpha$, the component along the μ axis of the $\alpha-$th nucleus:

$$\mathbf{f}_I = q_I \left[\mathbf{F}(\mathbf{R}_I) + \sum_J \mathbf{E}_J(\mathbf{R}_I) \right] ,$$

where $\mathbf{f}_I$ is the force acting on the $I-$th nucleus, q its charge, $\mathbf{F}$ the electric field of the electrons and $\mathbf{E}_J$ the electric field of the $J-$th nucleus. This is called the Hellmann-Feynman theorem, and states that the forces in a quantum system with a given electronic distribution can be evaluated with classical electrostatics.

Harmonic approximation

Every potential V is a quadratic function when considered sufficiently near its minimum. When the minimum of V is at R_0 and there its second derivative is equal to k, the force constant, then

$$V \approx \frac{1}{2} k (R - R_0)^2$$

near R_0. That is, each small-amplitude oscillation is harmonic. The harmonic approximation allows for useful simplifications of more general potentials.

Classical vibrations of a polyatomic molecule

The harmonic approximation can be exploited to reduce the classical vibrations of a polyatomic molecule to the solutions of an eigenvalue problem. To do so, the first step is to introduce normal coordinates q_i that diagonalize the Hamiltonian H. Then the nuclear masses and force constants are collected respectively in $\mathbf{M}$ and $\mathbf{K}$, that can be combined to give $\mathbf{W} = \mathbf{M}^{-1/2}\mathbf{K}\mathbf{M}^{-1/2}$, a real and symmetric matrix, which can thus be diagonalized. Finally, it is shown that the eigenvectors and eigenvalues of $\mathbf{W}$ give respectively the vibrational displacements and frequencies of the normal coordinates.

Quantum vibrations of a polyatomic molecule

When described in quantum-mechanical terms, the vibrations of a polyatomic molecule retain some aspects of their classical description because the normal coordinates diagonalize the Hamiltonian operator as well. For each normal coordinate, a vibrational Hamiltonian operator can be introduced as

$$h_i = -\frac{\partial^2}{\partial t_i^2} + t_i^2$$

such that $H = \sum_i h_i$, where the dimensionless coordinates $t_i = q_i \sqrt{\omega_i/\hbar}$. The quantum vibrational state of the system is then a product of eigenstates of the h_i.

2.2 Quantum mechanics of a crystal

We now move to an infinite crystal, and recall some important concepts of the theory of solids, following the approach of Ziman [56].

Translational symmetry

Several materials solidify forming a crystal. Bulk properties of crystals can be described referring to an infinite lattice characterized by translational symmetry. This means that it is possible to introduce lattice vectors $\mathbf{a}_1$, $\mathbf{a}_2$ and $\mathbf{a}_3$ such that the structure is invariant with respect to the translations

$$\mathbf{l} = l_1\mathbf{a}_1 + l_2\mathbf{a}_2 + l_3\mathbf{a}_3, \quad \text{with } l_1, l_2, l_3 \in \mathbb{Z}.$$

These three lattice vectors define a cell of the crystal. The lattice is obtained translating the cell by all the values of $\mathbf{l}$. The same invariance must hold for every bulk property $f(\mathbf{r})$:

$$f(\mathbf{r}) = f(\mathbf{r} + \mathbf{l}),$$

so that every property of a crystal is a multiple periodic function. Since any such function can be expressed as a Fourier series, it is easy to show that a generic bulk property can be written as

$$f(\mathbf{r}) = \sum_{\mathbf{g}} A_{\mathbf{g}} \mathrm{e}^{i\mathbf{g}\cdot\mathbf{r}}.$$

Here $\mathbf{g}$ is the reciprocal lattice vector: it has the property that $\mathrm{e}^{i\mathbf{g}\cdot\mathbf{l}} = 1$, and can be written as

$$\mathbf{g} = 2\pi \left(n_1\mathbf{b}_1 + n_2\mathbf{b}_2 + n_3\mathbf{b}_3\right),$$

where

$$\mathbf{b}_1 = \frac{\mathbf{a}_2 \times \mathbf{a}_3}{\mathbf{a}_1 \cdot \mathbf{a}_2 \times \mathbf{a}_3}, \qquad \mathbf{b}_2 = \frac{\mathbf{a}_3 \times \mathbf{a}_1}{\mathbf{a}_1 \cdot \mathbf{a}_2 \times \mathbf{a}_3}, \qquad \mathbf{b}_3 = \frac{\mathbf{a}_1 \times \mathbf{a}_2}{\mathbf{a}_1 \cdot \mathbf{a}_2 \times \mathbf{a}_3}$$

are the reciprocal lattice vectors. We also have:

$$A_{\mathbf{g}} = \frac{1}{v_{\text{cell}}} \int_{\text{cell}} f(\mathbf{r}) \mathrm{e}^{-i\mathbf{g}\cdot\mathbf{r}} \mathrm{d}\mathbf{r}.$$

Bloch theorem

By making use of translational invariance, we can prove that

$$|\mathbf{l}\rangle = \mathrm{e}^{i\mathbf{k}\cdot\mathbf{l}}\,|0\rangle \quad \forall\,\mathbf{l}.$$

This means that a vector **k** of the reciprocal lattice exists for every wave function such that its translation by **l** amounts to the multiplication by $\exp(i\mathbf{k}\cdot\mathbf{l})$. This most important theorem is solid-state physics is called the Bloch theorem. In the particular case of electrons, Bloch theorem reads

$$\psi_{\mathbf{k}}(\mathbf{r}+\mathbf{l}) = \mathrm{e}^{i\mathbf{k}\cdot\mathbf{l}}\psi_{\mathbf{k}}(\mathbf{r}).$$

This means that we can label a wavefunction with the wave vector that satisfies Bloch theorem. It can also be seen that the above relation does not hold for unique values of **k**, but for infinite discrete sets of wave vectors differing one from another by a reciprocal lattice vector **g**. This poses the problem on to uniquely define the wave vector of a given state, which can be solved in one dimension by requiring the modulus of **k** be inside the first Brillouin zone,

$$-\frac{\pi}{a} < k \leq \frac{\pi}{a},$$

and similarly in three dimensions. We thus see that a translational invariant infinite system can be described referring only to its repeat unit.

Born-von Kármán boundary conditions

Also called cyclic or periodic boundary conditions, Born-von Kármán conditions allow to model periodic infinite systems. For a one-dimensional system they write

$$\psi(x + La) = \psi(x),$$

so that, recalling Bloch theorem, we have

$$\mathrm{e}^{ikLa} = 1,$$

meaning

$$k = \frac{2\pi m}{La}, \qquad \text{with } m \in \mathbb{Z}.$$

Therefore,

$$-\frac{1}{2}L < m < \frac{1}{2}L,$$

from which we see that, for macroscopic systems, the set of k constitutes a quasi-continuum.

2.3 Density functional theory

We now turn to atomic units putting

$$a_0 = m_\mathrm{e} = \mathrm{e} = \hbar = E_\mathrm{h} = \frac{1}{4\pi\varepsilon_0} = 1$$

and expose the principles of density functional theory (DFT), following Parr and Yang [22] for the time-independent case and Marques and Gross [57] for its time-dependent extension.

Stationary theory

We start recalling the simple rule of calculation coming from elementary quantum mechanics for the expectation value of the generic observable $\mathcal{O}$,

$$\langle \mathcal{O}[\Psi] \rangle = \frac{\langle \Psi | \mathcal{O} | \Psi \rangle}{\langle \Psi | \Psi \rangle},$$

where we have put in evidence that the wave function Ψ completely determines the expectation value of every observable. We also add that solving $H\Psi = E\Psi$ numerically requires prohibitively long computation times, so that the simulation of materials properties by means of this formula is an impracticable way. However, it was shown by Hohenberg and Kohn [4, 5] that the role of Ψ can be taken by the electron density

$$\rho(\mathbf{r}) = N \int |\Psi|^2 \mathrm{d}\mathbf{r}',$$

where the primed differential prescribes to integrate over the coordinates of all electrons in the system expect for one, which is assigned the position $\mathbf{r}$. In particular, they shown (i) that there exists a biunivocal correspondence between the external potential $v(\mathbf{r})$ and the electron density $\rho(\mathbf{r})$, and (ii) that the electron density of the ground state minimizes its energy. These are called the Hohenberg-Kohn theorems, and their formulation in 1964-1965 is taken as the birth of DFT [23]. Now we introduce a non-interacting reference system in which the electrons are regarded as independent and interacting with an effective field such that the Schrödinger equation now writes

$$\left[-\frac{1}{2}\nabla^2 + v_\mathrm{eff} \right] \phi_i = \varepsilon_i \varphi_i,$$

where the ϕ_i are the Kohn-Sham orbitals, populated in the non-interacting reference systems, with eigenvalues ε_i, and such that

$$\rho(\mathbf{r}) = \sum_{i=0}^{N} |\phi(\mathbf{r})|^2,$$

and

$$v_{\text{eff}} = v(\mathbf{r}) + \int \frac{\rho(\mathbf{r}')}{|\mathbf{r} - \mathbf{r}'|} \mathrm{d}\mathbf{r}' + v_{\text{xc}}(\mathbf{r}),$$

where

$$v_{\text{xc}}(\mathbf{r}) = \frac{\delta E_{\text{xc}}}{\delta \rho}$$

is the exchange-correlation potential, with $E_{\text{xc}}[\rho]$ the exchange-correlation functional. These are called the Kohn-Sham equations. Two observations are worth at this point. First, v_{eff} is a self-consistent potential, so that these equations are solved by iteration. Second, the knowledge of $E_{\text{xc}}[\rho]$ solves exactly the electronic problem. However, $E_{\text{xc}}[\rho]$ is not known exactly for the moment, so that approximations to the exchange-correlation functional must be used. In particular, in this Thesis we make use of the B3LYP functional [58, 59, 60, 61].

Time-dependent theory

In the time-dependent case, the analogous of Hohenberg-Kohn theorems is the Runge-Gross theorem. In particular, introducing the quantum mechanical action operator

$$\mathcal{A}[\phi] = \int_{t_0}^{t_1} \left\langle \phi(t) \middle| -\frac{\partial}{\partial t} - H(t) \middle| \phi(t) \right\rangle \mathrm{d}t,$$

it is possible to see that imposing its functional derivative null the Schrödinger equation is obtained. Thus the stationary points of $\mathcal{A}[\phi]$ are solutions of the Schrödinger equation. Considering now a perturbation $v^{(1)}(\mathbf{r})$ to the stationary external potential $v^{(0)}(\mathbf{r})$ such that

$$v(\mathbf{r}, t) = \begin{cases} v^{(0)(\mathbf{r})} & \text{for } t < t_0, \\ v^{(0)}(\mathbf{r}) + v^{(1)}(\mathbf{r}) & \text{for } t \geq t_0, \end{cases}$$

the electron density can be written as a perturbative expansion:

$$\rho(\mathbf{r}, t) = \begin{cases} \rho^{(0)}(\mathbf{r}) & \text{for } t < t_0, \\ \rho^{(0)}(\mathbf{r}) + \rho^{(1)}(\mathbf{r}) + \ldots & \text{for } t \geq t_0, \end{cases}$$

where $\rho^{(n)}$ has an $n-$order dependence on the perturbation $v^{(1)}(\mathbf{r})$. In a linear-response framework the above series is truncated at first order. Then, $\rho^{(1)}$ can be expanded in terms of the imperturbed orbitals $\{\phi_i\}$ to obtain

$$\rho^{(1)}(\mathbf{r}) = \sum_{ij} \delta P_{ij} \phi_i^*(\mathbf{r}) \phi_j(\mathbf{r}),$$

where δP_{ij} depends both on $v^{(1)}(\mathbf{r})$ and $E_{\text{xc}}[\rho]$.

2.4 Computational tools

All molecular and periodic models described in this Thesis have been realized by means of the molecular editor Avogadro [62]. Vibrational normal modes have been inspected using Molden [63, 64]. DFT simulations have been run on molecular models by using the GAUSSIAN G09 software [65], published in an early version by John Pople, who shared the Nobel Prize in Chemistry with Walter Kohn in 1998 for his development of computational methods in quantum chemistry. DFT has been applied to periodic models using the CRYSTAL17 software [66, 67]. The functional B3LYP has been chosen based on its extensive use, together with the basis set 6-31G(d,p). Finally, scaling factors have been applied to computed frequencies in order to fit experimental data: 0.96 for N2200 and the low-wavenumber region of the IR spectra of graphene nanoribbons [68], 0.98 for the high wavenumber Raman region of graphene nanoribbons [69], 0.978 when investigating PVDF and P(VDF−TrFE).

Chapter 3

N2200

I can't keep you there
you're everywhere

— Beach House, *Woo*

The comprehension of the nature of charge carriers in $\pi-$conjugated polymers is of fundamental interest [70]. In Chapter 1, it was mentioned that P(NDI2OD-T2), briefly referred to as N2200, is a particular instance in this class of advanced materials, which incorporates both $\pi-$conjugation and redox sites [7]. Recent spectroscopy experiments [1] have unveiled polaron confinement in N2200, as illustrated in Figures 3.1 and 3.2. DFT calculations were also used, but the dopant was not taken into account explicitly. In this Chapter, we investigate the polaron localization in N2200, also considering its interaction with a dopant.

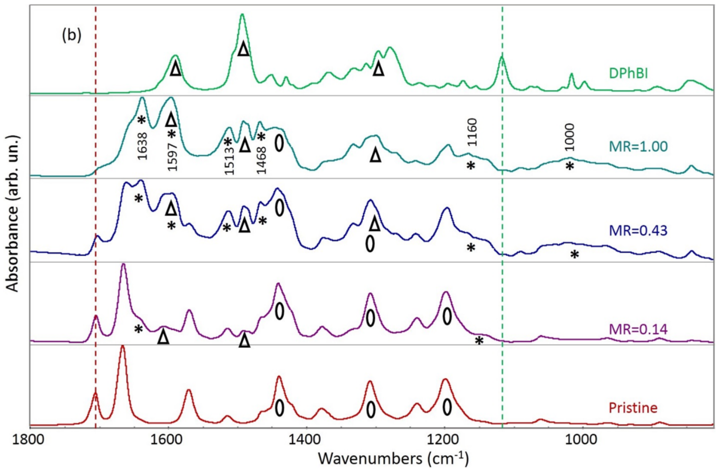

Figure 3.1: From bottom to top: IR spectra of pristine N2200, doped N2200 at increasing dopant/polymer ratio MR and pristine dopant DPhBI. The latter is a molecular dopant with a relatively complex structure, not taken into account in this Chapter. Asterisks label the features induced by doping, and indicate therefore polaron markers. Reproduced from Ref. [1].

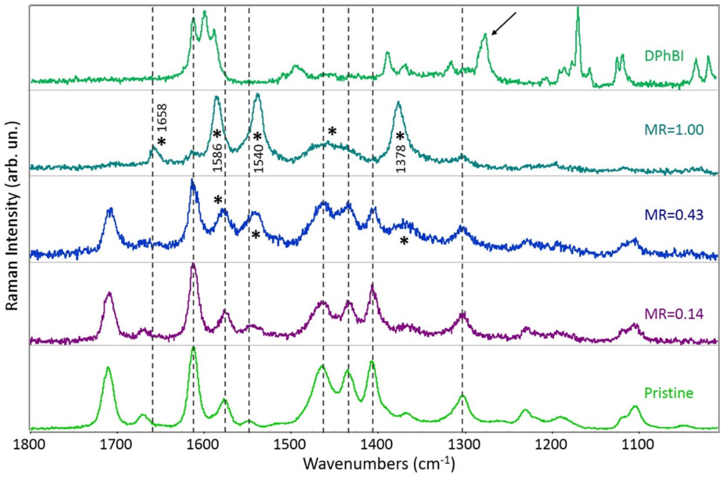

Figure 3.2: From bottom to top: Raman spectra of pristine N2200, doped N2200 at increasing dopant/polymer ratio MR and pristine dopant DPhBI. The latter is a molecular dopant with a relatively complex structure, not taken into account in this Chapter. Asterisks label the features induced by doping, and indicate therefore polaron markers. Reproduced from Ref. [1].

3.1 The computational model

Before we go into the details of the computational investigation carried out in this Chapter, it is necessary to introduce the model and show the motivation lying behind its structure. The repeat unit of N2200 is represented in Figure 3.3a. Figures 3.3b, 3.4, and 3.5 show five ball-and-stick models:

1. In Figure 3.3b, the molecular model of undoped N2200 is shown. It has the structure of the monomer of N2200 with the addition of two thiophene rings at its boundaries. This allows us to take into account the inter-ring torsion of the bithiophene (T2) unit. Moreover, the relatively small dimension of this model allows including the alkyl chains. We assume their conformation to be *trans*-planar and take their insertion angle similar to that of other $\pi-$conjugated polymers [71]. When considered as electrically neutral, we call this model **1**.

2. To the same model a negative elementary charge can be assigned, in which case we refer to it as $\mathbf{1}^-$. This represents n-doped N2200 in the absence of the interacting doping species, and is shown in Figure 3.4a.

3. A more realistic description of n-doped N2200 is obtained by attaching a lithium atom to oxygen, as represented in Figure 3.4b. In choosing lithium as doping agent and oxygen as attachment site, we are guided by previous studies [72, 73]. We call this model $\mathbf{1^-Li^+}$. Lithium is here considered as the doping agent also based on the small value of its ionic radius, which in turn prevents phase segregation of the doped polymer in the experiments. Moreover, the simple electronic structure of lithium allows us to carefully consider its changes upon doping. On the other hand, we immediately realize

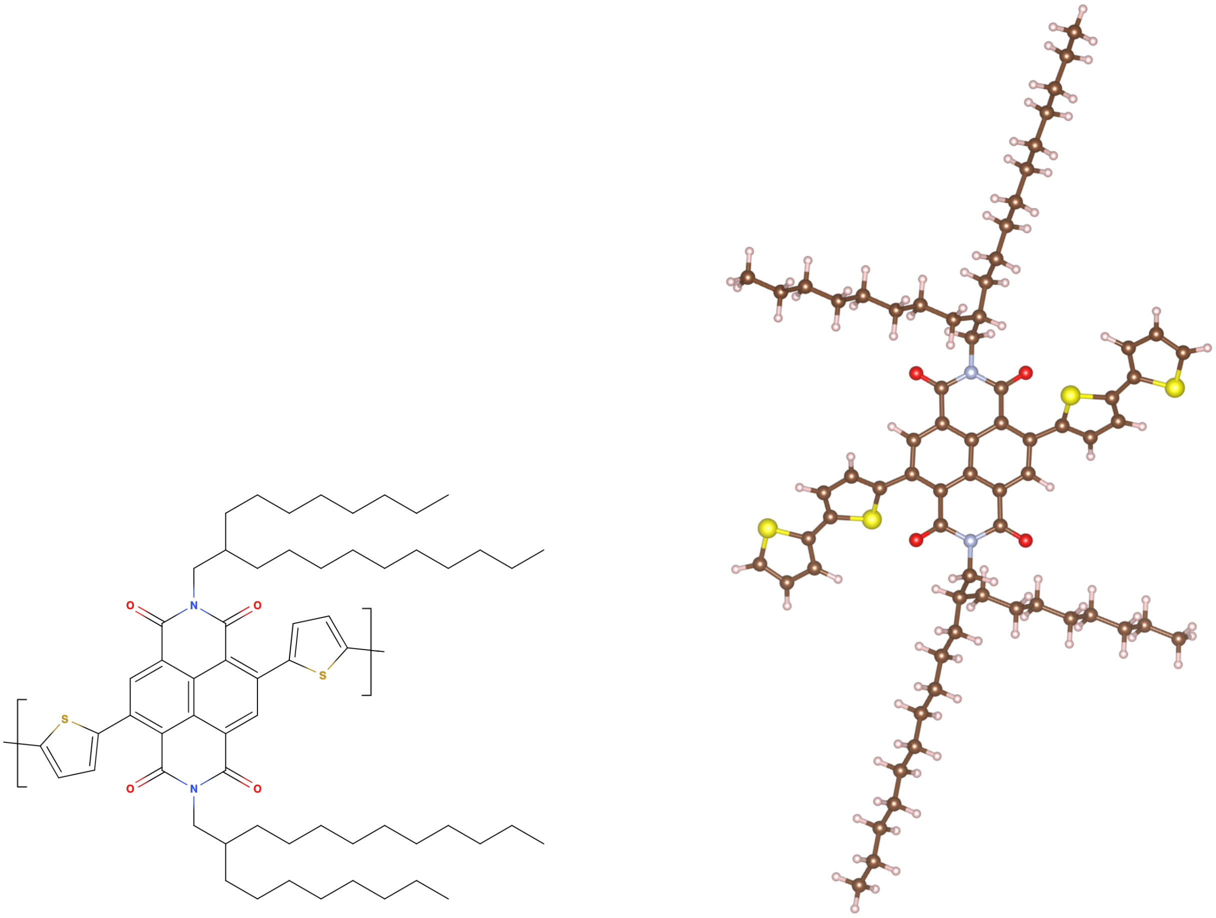

(a) N2200

(b) 1

Figure 3.3: (a) Structural formula of N2200. (b) Molecular model of undoped N2200.

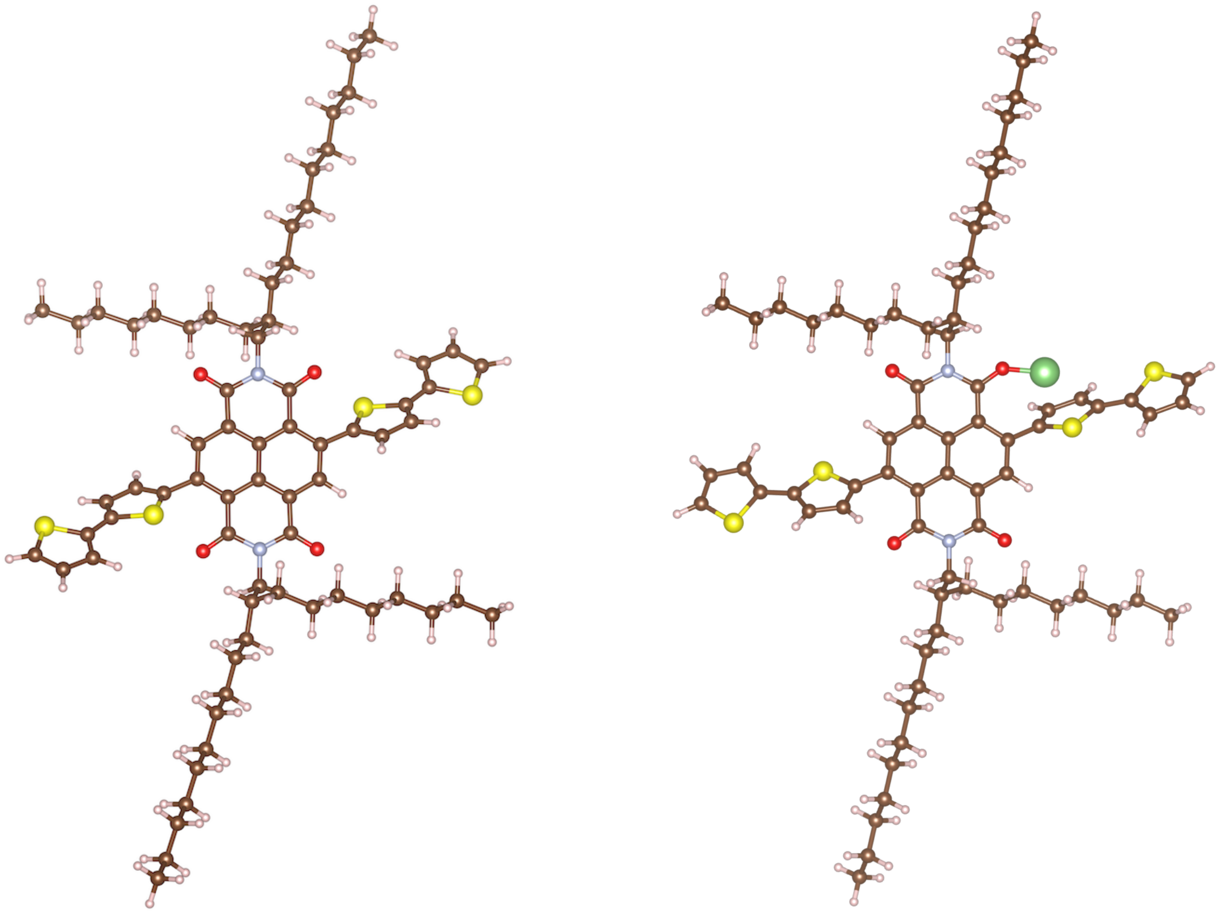

(a) $\mathbf{1}^-$

(b) $\mathbf{1}^-\mathbf{Li}^+$

Figure 3.4: Molecular models of doped N2200.

that two non-equivalent oxygen sites are present in N2200, which differ with respect to their distances from T2. In the following, we will study the lithiation of the oxygen near the thiophene ring, since this allows to study a particular interaction involving lithium (see Figure 3.8).

4. The monomer approach assumed by models $\mathbf{1}$, $\mathbf{1}^-$, and $\mathbf{1}^-\mathbf{Li}^+$ can be extended to periodic models considering one-dimensional crystals. Figure 3.5 represents two portions with three repeat units of $\mathbf{1}$–PBC and $\mathbf{1}^-\mathbf{Li}^+$–PBC.

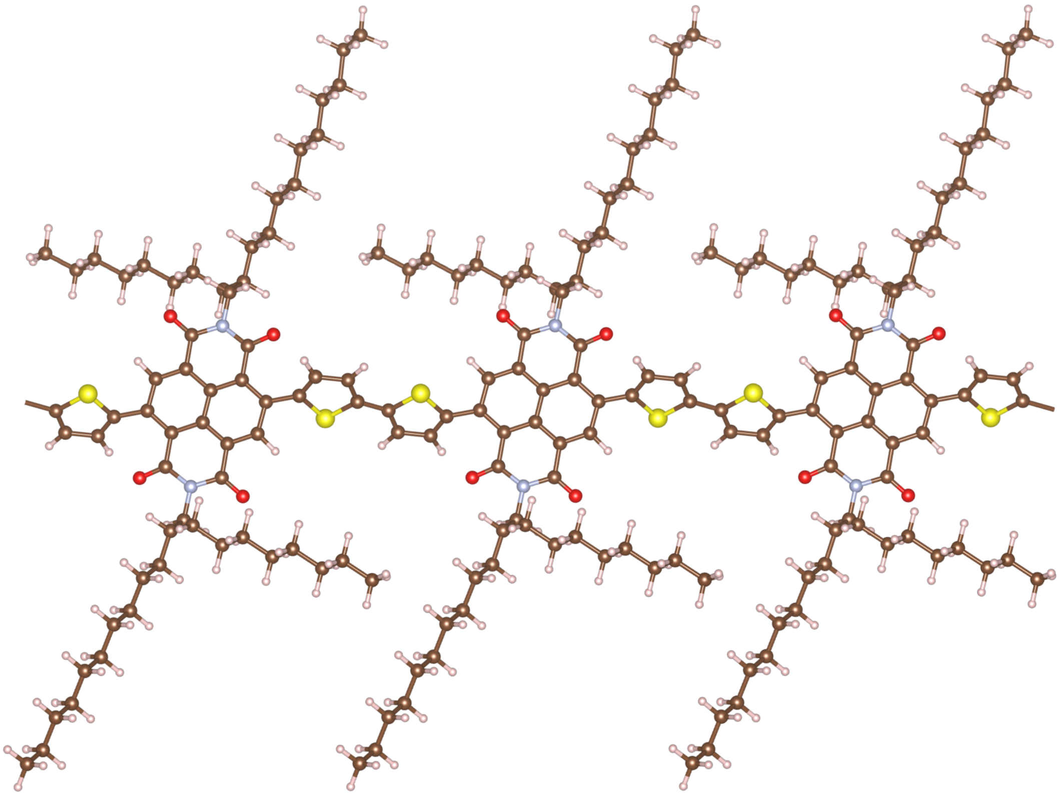

(a) $\mathbf{1}$–PBC

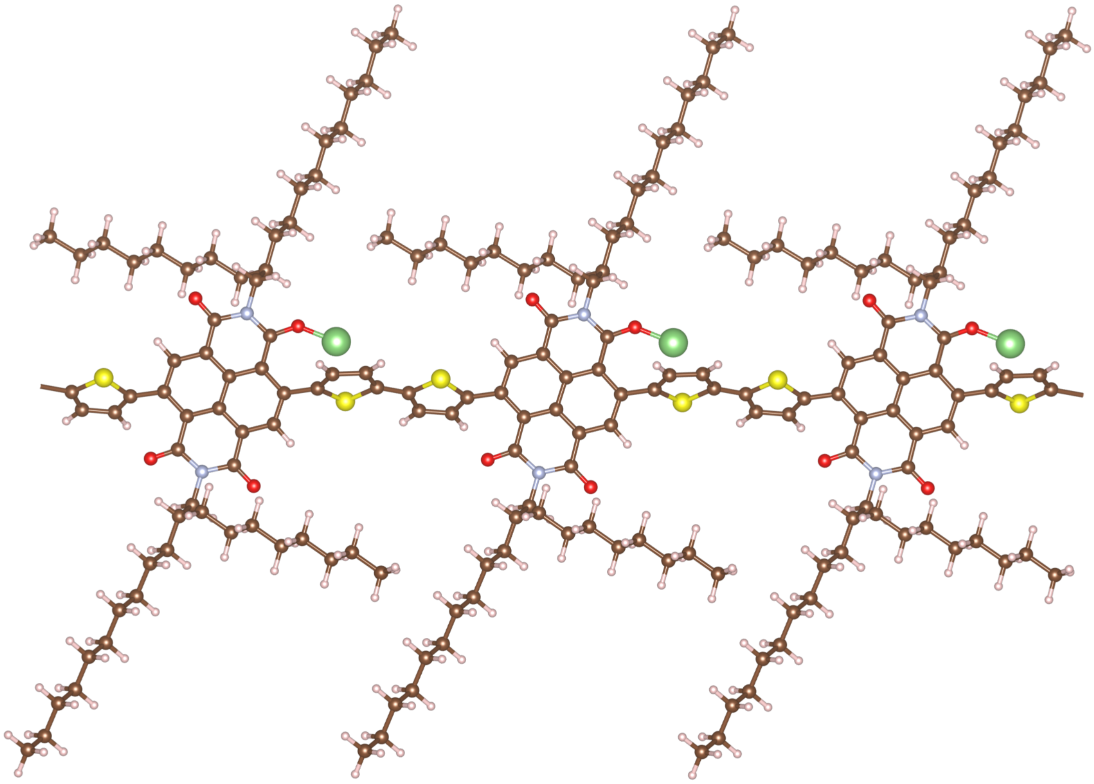

(b) $\mathbf{1^{-}Li^{+}}$–PBC

Figure 3.5: One-dimensional periodic models of N2200.

3.2 Results and discussion

Energies of the FMOs. We can consider the effect of lithium doping on the stability of N2200 by examining the energies of the frontier molecular orbitals (FMOs) of $\mathbf{1}^-$ and $\mathbf{1}^-\mathbf{Li}^+$. As shown in Table 3.1 and Figure 3.6, the singly-occupied molecular orbital (SOMO) of $\mathbf{1}^-\mathbf{Li}^+$ is lower in energy than the SOMO of $\mathbf{1}^-$. This means that $\mathbf{1}^-\mathbf{Li}^+$ is more stable than $\mathbf{1}^-$, so that the attachment of lithium has a stabilizing effect on the doped species [74]. We also verify that n-doping reduces the energy gap E_g.

Model	MO	Energy (eV)	E_g (eV)
1	LUMO	-3.33	2.18
1	HOMO	-5.51	
$\mathbf{1}^-$	SOMO	-1.41	1.64
$\mathbf{1}^-$	β−HOMO	-3.05	
$\mathbf{1}^-\mathbf{Li}^+$	SOMO	-4.10	0.91
$\mathbf{1}^-\mathbf{Li}^+$	β−HOMO	-5.01	

Table 3.1: Energies of FMOs and energy gaps E_g of different molecular models of N2200.

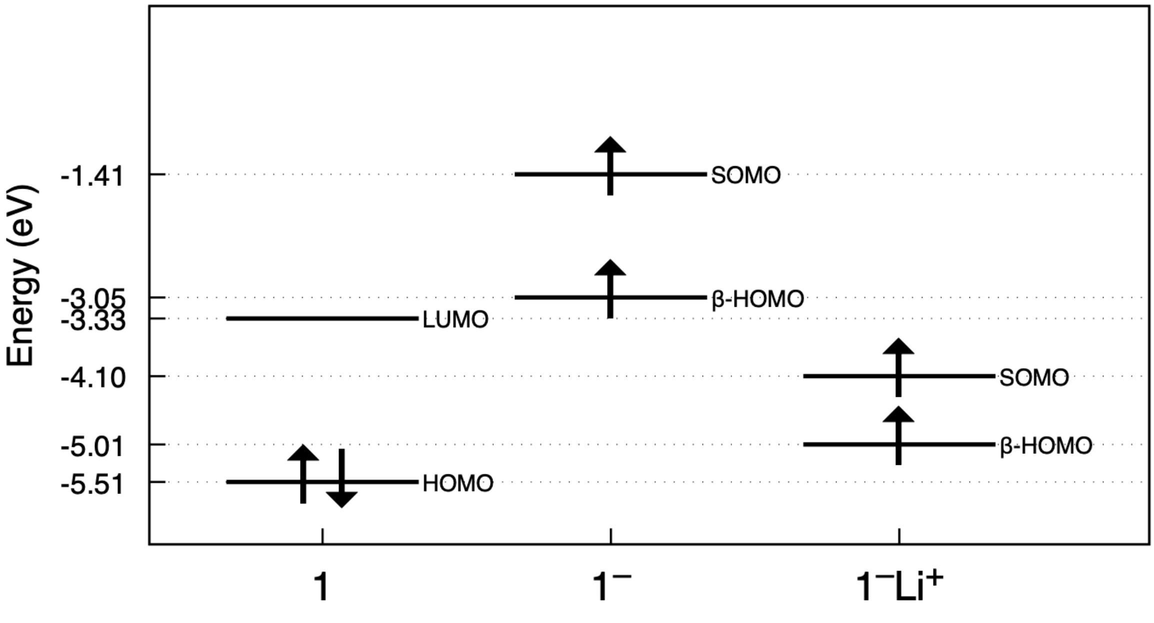

Figure 3.6: Representation of the energies of the FMOs of **1**, $\mathbf{1}^-$ and $\mathbf{1}^-\mathbf{Li}^+$.

Topology of the FMOs. The effect of doping on the electronic structure of N2200 modifies the topology of the FMOs occupied by the excess electron. These orbitals correspond to the LUMO of **1** and to the SOMOs of $\mathbf{1}^-$ and $\mathbf{1}^-\mathbf{Li}^+$. As shown in Figure 3.7, the FMOs of **1**

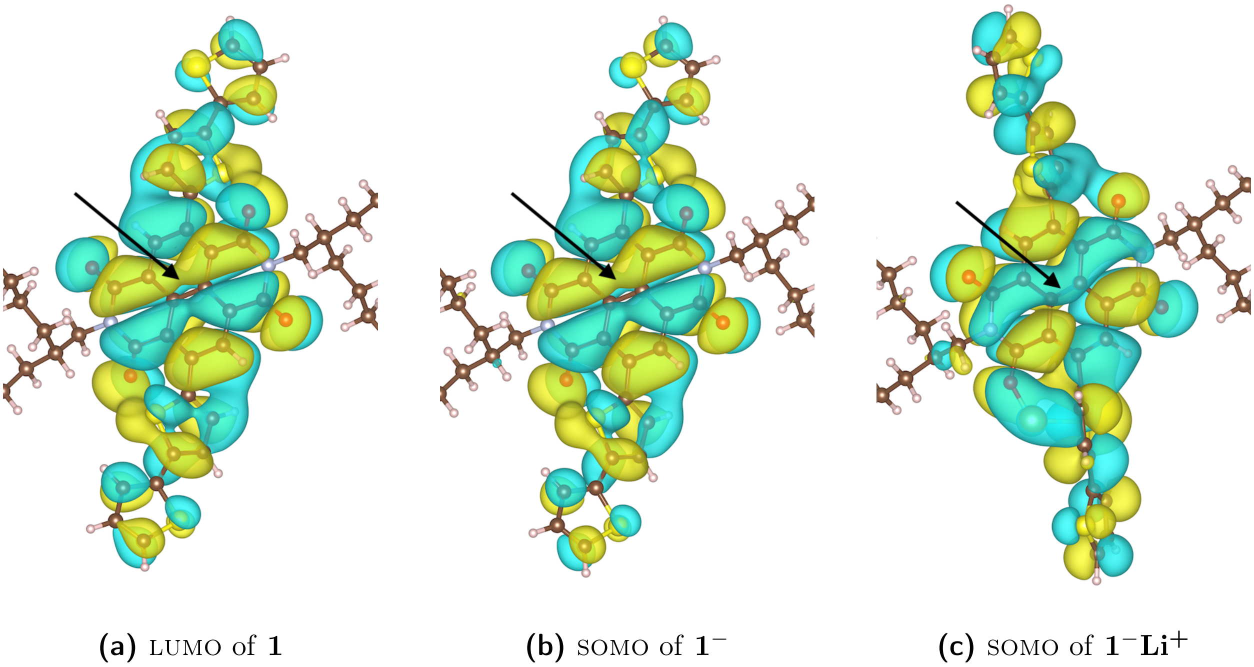
(a) LUMO of **1** **(b)** SOMO of $\mathbf{1}^-$ **(c)** SOMO of $\mathbf{1}^-\mathbf{Li}^+$

Figure 3.7: Isosurfaces of the FMOs of different molecular models of N2200. The FMOs are positive in yellow regions, negative in blue regions. Isosurfaces have been taken at $0.006\ a_0^{-3/2}$. Black arrows indicate the main differences observed in the three isosurfaces.

and $\mathbf{1}^-$ are almost identical, whereas that of $\mathbf{1}^-\mathbf{Li}^+$ changes because of the presence of Li. In particular, the inclusion of lithium causes the SOMO of $\mathbf{1}^-\mathbf{Li}^+$ to partially spread over the C−C bond in the center of the naphthalenediimide (NDI) unit, while that region is a node in the other models. Therefore, we expect $\mathbf{1}^-$ and $\mathbf{1}^-\mathbf{Li}^+$ to have different equilibrium geometries.

Effect of lithium motion and its position. The previous results motivate a further investigation about the role of lithium. In the minimum-energy configuration of $\mathbf{1}^-\mathbf{Li}^+$, Li disposes itself near the sulfur atom of a thiophene ring, in such a way that a molecular visualizer displays the two as covalently bonded (Figure 3.8). Although artificial, this fact suggests the existence of a potential well in the projection of the potential energy surface on the coordinate describing lithium displacement. For simplicity, we guess such a coordinate considering the dihedral angle Li−O−C−C, which we call τ. In Figure 3.9 we plot the total energy of $\mathbf{1}^-\mathbf{Li}^+$ at different values of τ, keeping constant all the other internal coordinates: as expected, the projection of the potential energy surface onto τ has a local minimum, which corresponds to the equilibrium geometry of $\mathbf{1}^-\mathbf{Li}^+$. More interestingly, we observe that even large variations of τ ($\sim 20\,^\circ$) cause total energy variations $\sim k_\mathrm{B}T$ at room temperature. Our model predicts therefore large fluctuations of τ at room temperature. Of course, in real doped samples of N2200 this feature may be influenced by the presence of solvent and neighboring molecules, which are not taken into account in this model. Nevertheless, we can still argue about the existence of a preferential interaction between lithium and the thiophene ring nearest to it. Such interaction resembles the CH−π interactions found in aromatic compounds [75].

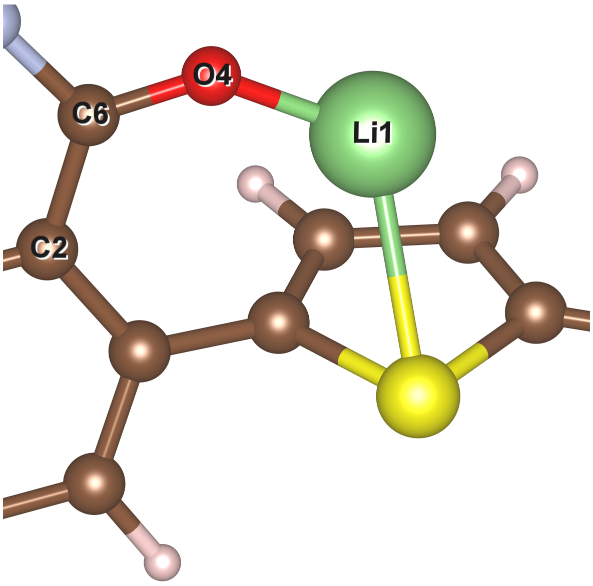

Figure 3.8: Artificial covalent bond between lithium and a sulfur atom in the $\mathbf{1^{-}Li^{+}}$ model. The labeled atoms define the dihedral angle Li−O−C−C, τ.

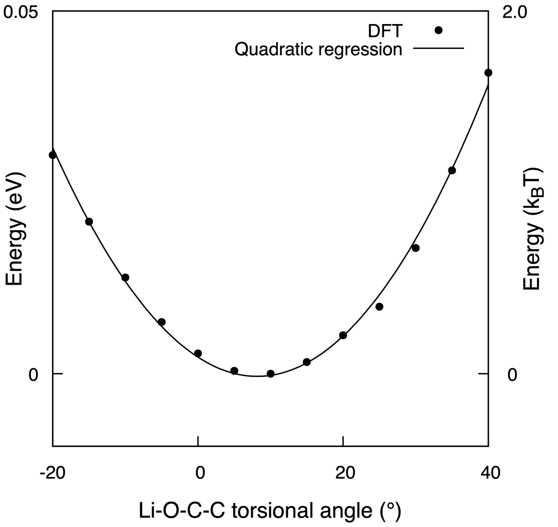

Figure 3.9: Total energy of the $\mathbf{1^{-}Li^{+}}$ model as a function of the Li−O−C−C dihedral angle τ. For the estimation of the thermal energy, $T = 298\,\mathrm{K}$ has been considered.

NBO analysis. The involvement of lithium as a dopant species is further investigated through a natural bond orbital (NBO) analysis, taking into account the labeling scheme defined in Figure 3.10. Such analysis shows that lithium donates almost completely its valence electron because its natural electron configuration is

$$\text{Li:}\quad [\text{He}]\,2\text{s}^{0.05}\,2\text{p}^{0.17}.$$

We observe that the 2p natural atomic orbital of lithium is partially populated; this is consistent with the fact that the SOMO of $\mathbf{1^{-}Li^{+}}$ has a bilobed shape near lithium, as shown in Figure 3.11. In Table 3.2 we also notice that the valence orbitals 2p_x, 2p_y, and 2p_z have different occupancies. This supports the existence of a directional interaction between lithium and the thiophene ring nearest to it.

Table 3.3 compares selected natural atomic charges of **1** and $\mathbf{1^{-}Li^{+}}$. It is found that the atoms and rings near the lithium atom have their natural charges most affected by lithiation. We notice in particular that the nearest thiophene ring has a large variation of its natural charge ($\Delta =$ `-0.13`), one order of magnitude larger than the other rings. Therefore, lithium

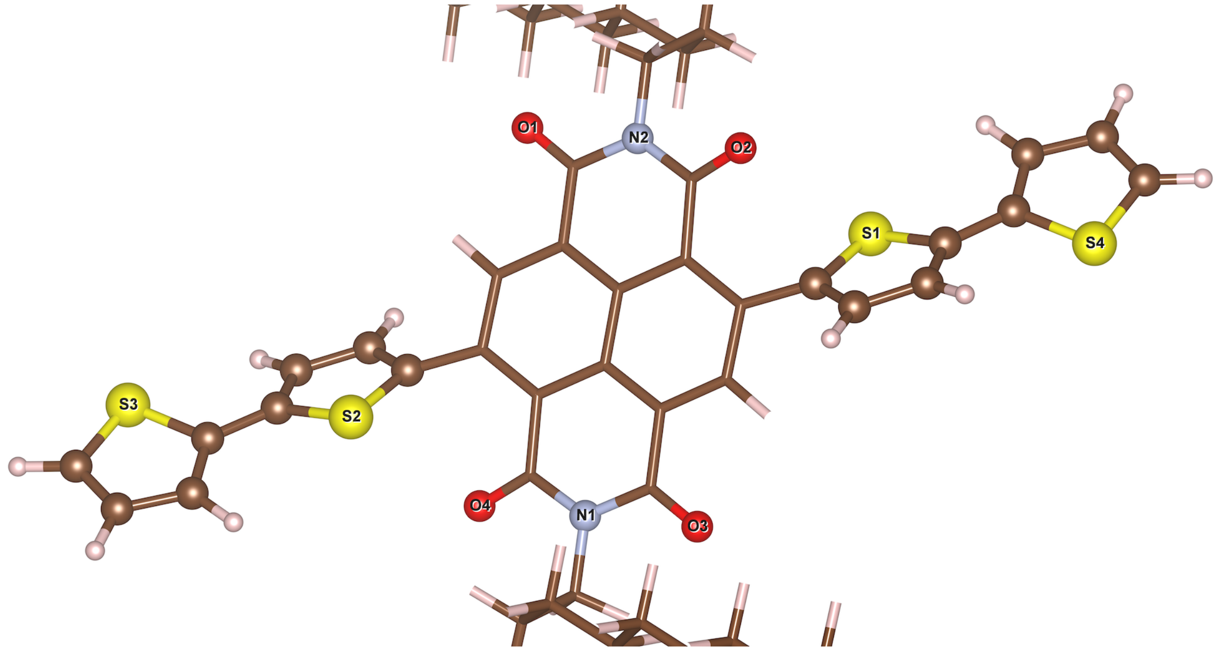
O1
N2
O2
S1
S4
S3
S2
O4
N1
O3

(a) 1

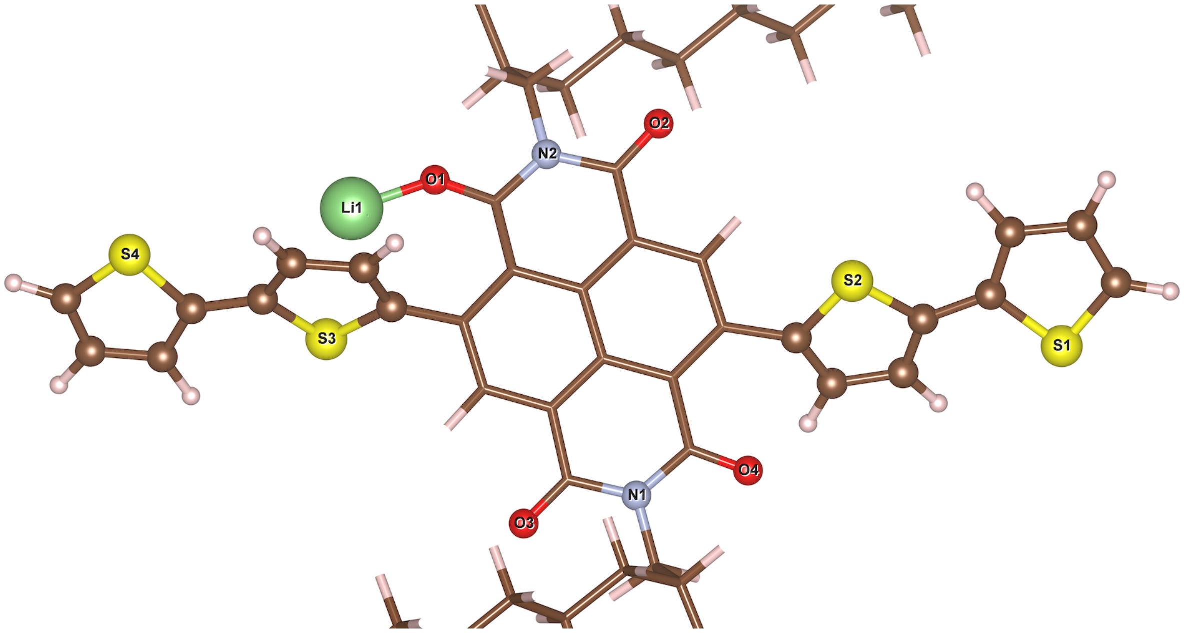
O2
N2
O1
Li1
S4
S2
S3
S1
O4
N1
O3

(b) 1^{-}Li^{+}

Figure 3.10: Labeling scheme of the atoms taken into account in the NBO analysis of Tables 3.2 and 3.3. The atoms omitted in such analysis are not represented as spheres.

Atom	Orbital	Type	Occupancy
Li1	1s	C	2.00
Li1	2s	V	0.05
Li1	$2p_x$	V	0.04
Li1	$2p_y$	V	0.06
Li1	$2p_z$	V	0.07
Li1	3s	R	0.00
Li1	$3p_x$	R	0.00
Li1	$3p_y$	R	0.00
Li1	$3p_z$	R	0.00

Table 3.2: NBO analysis of the $\mathbf{1^{-}Li^{+}}$ model: occupancies of the first nine natural orbitals of lithium. The atomic label is defined in Figure 3.10b. C, V, and R stand respectively for core, valence, and Rydberg natural atomic orbitals.

donates part of its charge to the nearest thiophene. This further supports the existence of an $\mathrm{OLi} - \pi$ interaction.

1		$\mathbf{1^{-}Li^{+}}$		
Atom or ring	q	Atom or ring	q	Δ
Li1	–	Li1	+0.78	–
N1	-0.48	N1	-0.47	+0.01
N2	-0.48	N2	-0.45	+0.03
O1	-0.59	O1	-0.79	-0.20
O2	-0.58	O2	-0.62	-0.04
O3	-0.59	O4	-0.60	-0.01
O4	-0.57	O3	-0.63	-0.06
T1	+0.06	T2	+0.05	-0.01
T2	+0.06	T3	-0.07	-0.13
T3	+0.02	T4	+0.04	+0.02
T4	+0.02	T1	+0.00	-0.02

Table 3.3: NBO analyses of **1** and $\mathbf{1^{-}Li^{+}}$: natural charges of some atoms and rings. Atomic labels are defined in Figure 3.10. Tn, with $n = 1, 2, 3, 4$, labels the thiophene ring containing the atom Sn. Natural charges are called q in this Table. Natural charges for the thiophene rings have been obtained summing the natural atomic charges of all the hydrogen, carbon and sulphur atoms of each ring. The last column reports the variations $\Delta = q(\mathbf{1^{-}Li^{+}}) - q(\mathbf{1})$ of natural charges from **1** to $\mathbf{1^{-}Li^{+}}$. Data of corresponding atoms or rings are on the same row.

Spin density. The spin density of $\mathbf{1^{-}Li^{+}}$ confirms the NBO analysis. Figure 3.12 illustrates the spin density, which represents the distribution of the excess charge donated by lithium. As expected, the spin density is important in the NDI unit, with non-negligible contributions also in the T2 units. Therefore, lithiation mainly affects the NDI unit of the molecule, while the T2 units play a minor role in charge delocalization. On the other side, alkyl

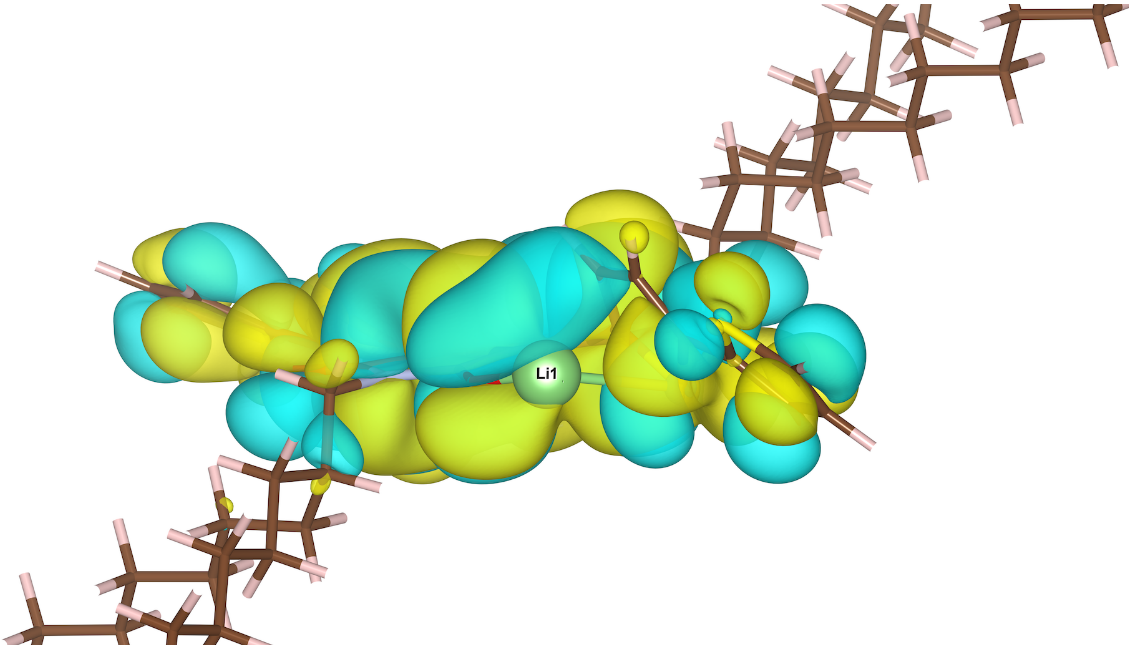

Figure 3.11: Particular of the isosurface of the SOMO of $\mathbf{1}^{-}\mathbf{Li}^{+}$, showing its bilobed shape near the lithium atom. The SOMO is positive in yellow regions, negative in blue regions. The isosurface has been taken at `0.006` $a_0^{-3/2}$.

chains are characterized by a null spin density, meaning that they are not involved in charge delocalization. Finally, the absence of spin density near the lithium atom confirms the nearly full donation of its valence electron.

Structural relaxation. Because of Feynman theorem [55], a variation of electron density in the region between two nuclei changes the strength of their chemical bond, hence their average equilibrium distance. Therefore, charge delocalization is expected to cause a perturbation of the nuclear positions of the NDI unit. This can be assessed by observing the differences between the bond lengths of $\mathbf{1}^{-}\mathbf{Li}^{+}$ and **1**, which are represented in the plot of Figure 3.13. We refer to this plot as a *bondplot*, where red and blue lines indicate bonds which respectively increase and decrease their length upon lithiation. By observing the bondplot, we immediately infer that charge delocalization produces a structural relaxation which is confined in the NDI and T2 units.

The reasons for structural relaxation are evident if we compare the bondplot of Figure 3.13 with the spin density of Figure 3.12. From this comparison, we notice that:

- In general, carbon-carbon bonds in the NDI unit increase their bond length when their internuclear spin density is overall positive, and decrease their bond length when the latter is negative.

- The thiophene ring near lithium is mostly affected. Indeed, all of its bonds are nodal regions for the spin density.

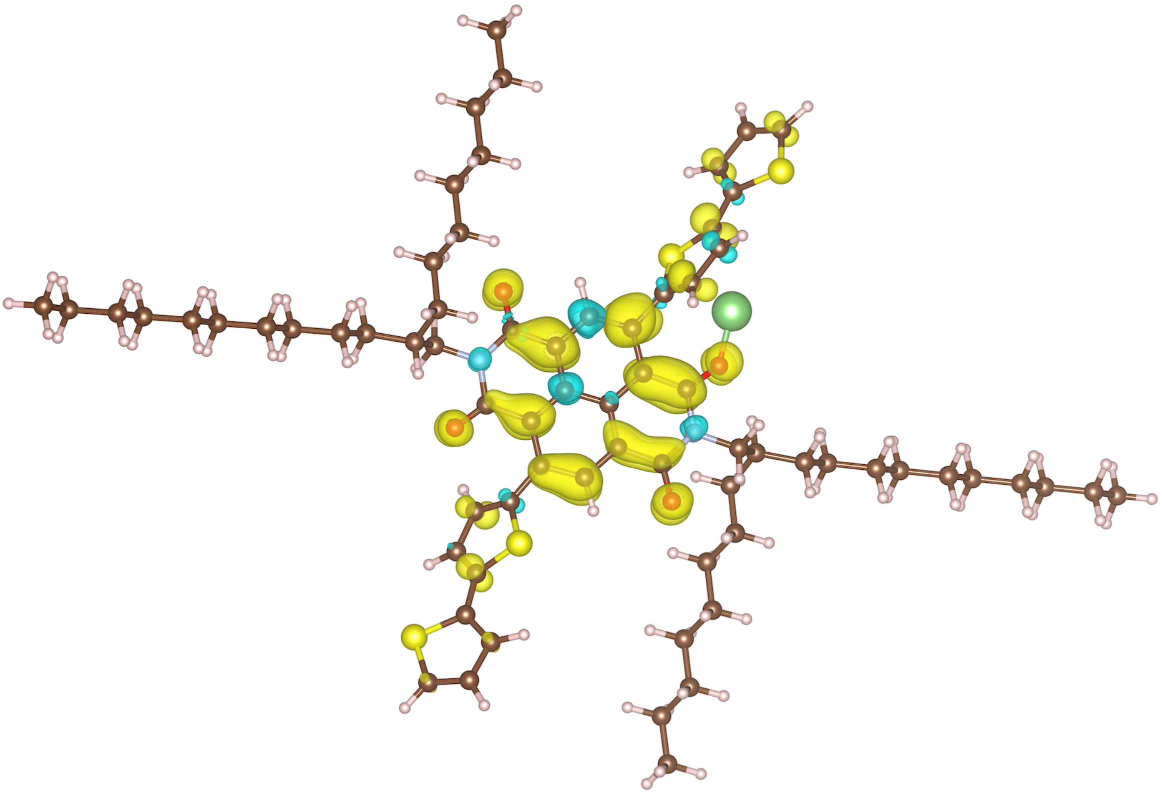

Figure 3.12: Isosurface of the spin density of $\mathbf{1}^{-}\mathbf{Li}^{+}$. The spin density is positive in yellow regions, negative in blue regions. The isosurface has been taken at `0.001` a_0^{-3}.

- Alkyl chains do not change their conformation. Coherently, they correspond to zero-spin density regions.
- The largest bond-length variation is found in the lithiation site. This is because lithiation weakens the double bond of the carbonyl group C=O.

This analysis shows that the spin density is a good descriptor for explaining the variation of electron density caused by lithiation, and the associated geometry relaxation.

The effect of lithium attachment on structural relaxation. When discussing the topology of the FMOs of $\mathbf{1}^{-}$ and $\mathbf{1}^{-}\mathbf{Li}^{+}$, we have noted some differences, illustrated in Figure 3.7. Such differences make the bondplot of $\mathbf{1}^{-}$, represented in Figure 3.14, different from that of $\mathbf{1}^{-}\mathbf{Li}^{+}$. In particular:

- The deformation pattern of the NDI unit is more homogeneous in $\mathbf{1}^{-}$. This is an effect of the absence of an attached doping agent, as a result of which the symmetry of charge delocalization increases.
- Roughly, all the thiophene rings have their structure modified to the same extent. This is because of the lack of a localized $\mathrm{OLi} - \pi$ interaction.
- All the oxygen-carbon bond lengths change in the same way. Again, this is because no lithiation site is present in $\mathbf{1}^{-}$.

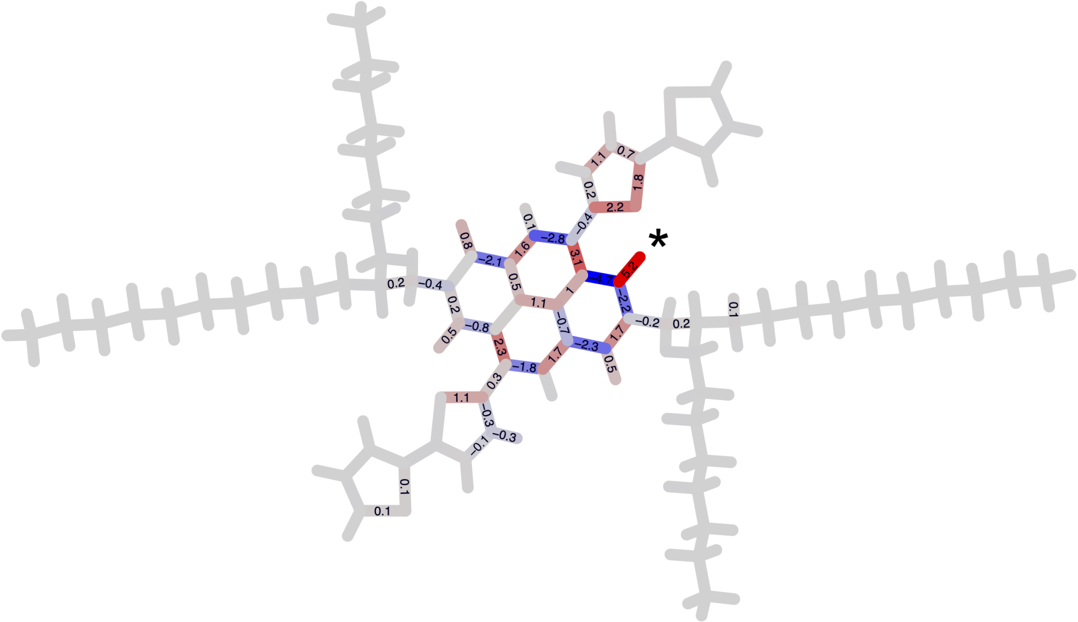

Figure 3.13: Bondplot of $\mathbf{1^{-}Li^{+}}$: bond-length differences between $\mathbf{1^{-}Li^{+}}$ and **1**. This plot has the same orientation as in Figure 3.12, so that the asterisk indicates the lithiation site. Differences are reported in pm. Only differences whose absolute value is equal to or larger than 0.1 pm are shown. Bond-length variations are positive in red regions, negative in blue regions.

These observations show that lithium doping affects the structural relaxation confining the excess charge in the NDI unit. We may wonder if the origin of this confinement is due to the variation of conjugation between $\mathbf{1^{-}}$ and $\mathbf{1^{-}Li^{+}}$. This can be roughly measured by comparing in the two models the dihedral angles between NDI and T2 and within T2. Taking into account the labeling scheme defined in Figure 3.15, Table 3.4 shows that lithiation does not modify appreciably the conjugation of the molecule. Therefore, we can infer that lithium attachment confines the excess charge on the NDI unit through electrostatic interaction, leaving the overall conjugation of the molecule unmodified. This is because the attached lithium acts as a positive-charge center, as it results from the NBO analysis.

Electron density difference. We finally consider the variation of electron density caused by doping. Following the conceptual scheme introduced by Brédas [11], we represent the electron density variation associated with the transformation represented in the cycle of the inset of Figure 3.16. This corresponds to subtracting the electron density of **1** from the electron density of a new model obtained constraining $\mathbf{1^{-}}$ to have the geometry of **1**. We will refer to this model as *$\mathbf{1^{-}}$ in the geometry of **1***. In doing this, we neglect two important points, namely the structural relaxation following the ionization process and the attachment

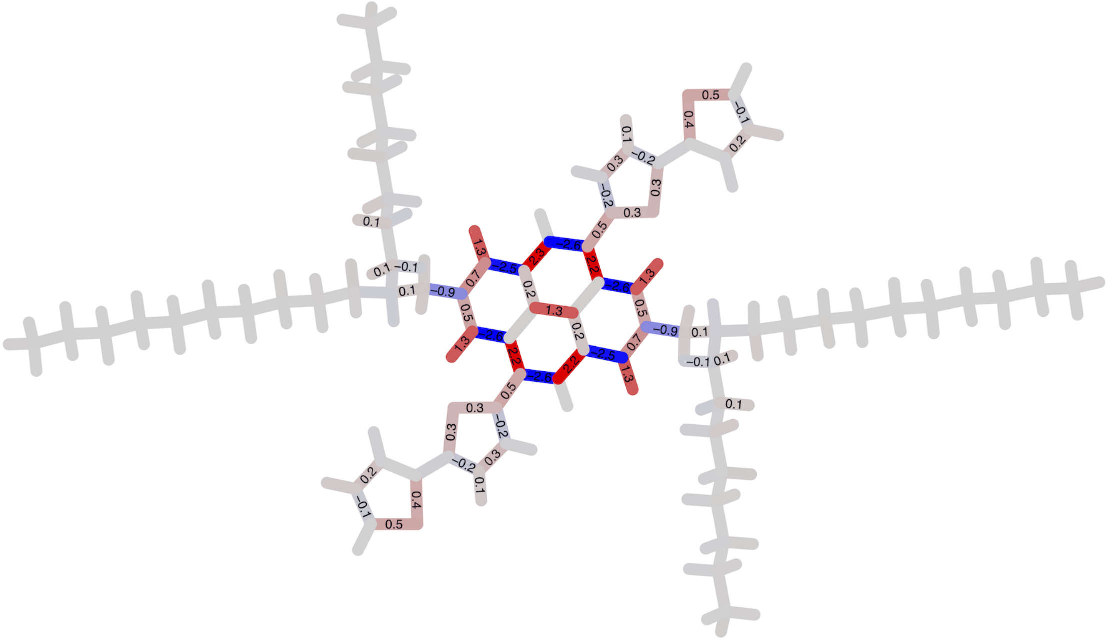

Figure 3.14: Bondplot of $\mathbf{1}^-$: bond-length differences between $\mathbf{1}^-$ and $\mathbf{1}$. Differences are reported in pm. Only differences whose absolute value is equal to or larger than 0.1 pm are shown. Bond-length variations are positive in red regions, negative in blue regions.

of lithium. Nevertheless, this comparison is still meaningful, because the electron-density difference of Figure 3.16 nicely correlates with the previous results.

Extension to one-dimensional crystals. The theoretical approach discussed above can be extended to the periodic models of Figure 3.5, which are treated within periodic boundary conditions (PBCs). In particular, here we focus our attention on the structural relaxation induced by lithiation. Figure 3.17 reports the bondplot of a portion of $\mathbf{1}^-\mathbf{Li}^+$–PBC. A comparison with the bondplot of $\mathbf{1}^-\mathbf{Li}^+$ reported in the inset shows that in the periodic model:

- Structural relaxation is more delocalized and completely involves the T2 units.
- The bond-length increase in the lithiation site is smaller than in the molecular model.
- The most deformed thiophene ring is still the one near lithium.

Starting from these observations, we infer that this periodic model is characterized by a larger excess charge delocalization than the corresponding molecular model. A contribution to this is given by the absence of peripheral NDI units in molecular $\mathbf{1}^-\mathbf{Li}^+$, which would provide further excess charge, causing all the thiophene rings to change their conformation. However, the minor bond-length increase in the lithiation site of the periodic model suggests

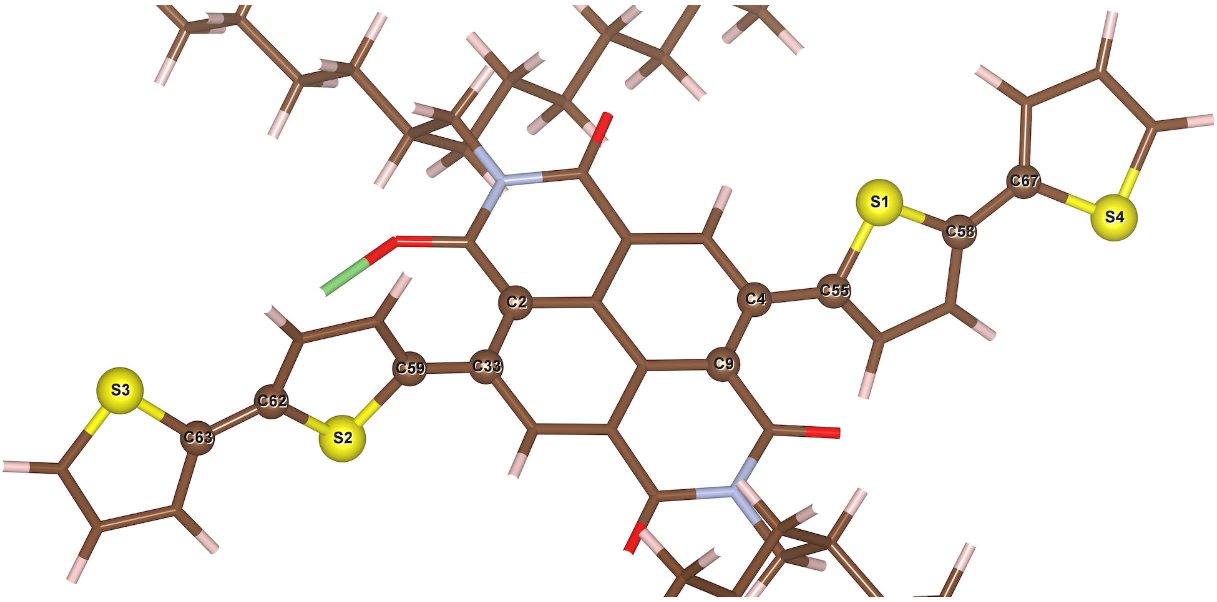
S3
C63
C62
S2
C59
C33
C2
C4
C55
C9
S1
C58
C67
S4

(a) 1^-

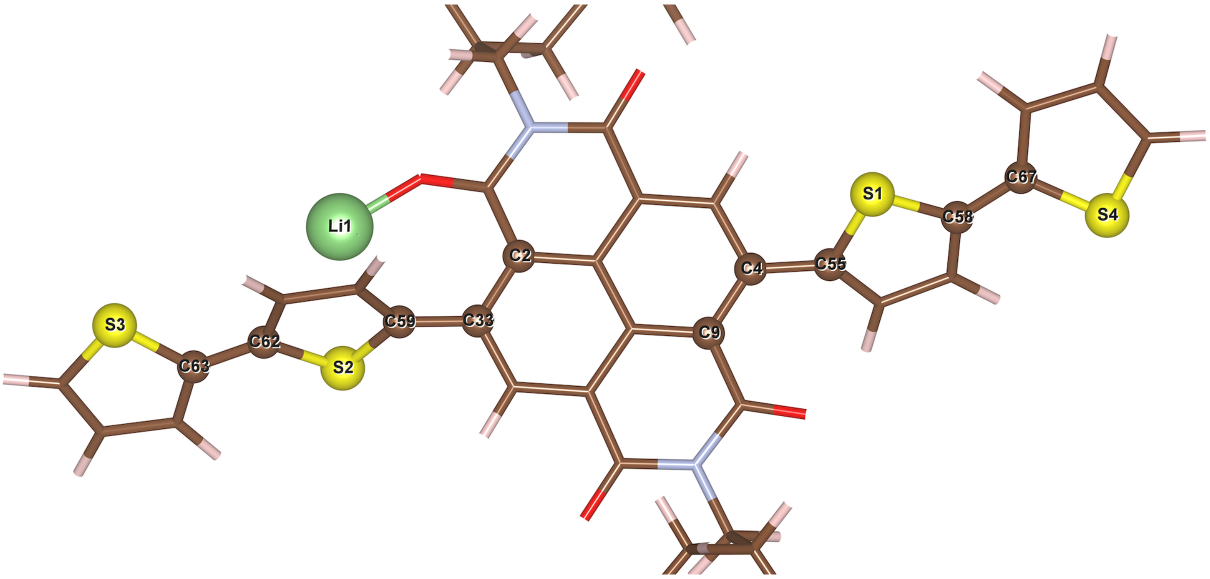
Li1
S3
C63
C62
S2
C59
C33
C2
C4
C55
C9
S1
C58
C67
S4

(b) 1^-Li$^+$

Figure 3.15: Labeling of the dihedral angles taken as a rough measure for the conjugation in the molecular models of doped N2200 in Table 3.4. Only atoms defining the dihedral angles and lithium are represented as spheres.

	$\mathbf{1}^-$		$\mathbf{1}^-\mathbf{Li}^+$		
Label	α (°)	$\min\lvert n\pi-\alpha\rvert$ (°)	α (°)	$\min\lvert n\pi-\alpha\rvert$ (°)	Δ (°)
S1-C55-C4-C9	58.7	58.7	139.2	40.8	-17.9
S2-C59-C33-C2	60.3	60.3	119.4	60.6	+0.3
S3-C63-C62-S2	159.4	20.6	164.9	15.1	-5.5
S4-C67-C58-S1	159.5	20.5	159.4	20.6	+0.1

Table 3.4: Values of some dihedral angles α in $\mathbf{1}^-$ and $\mathbf{1}^-\mathbf{Li}^+$. Atomic labels are defined in Figure 3.15. Here we use $\min|n\pi-\alpha|$, with $n \in \mathbb{Z}$, as a measure of the non-planarity of the dihedral angle α. We have $\min|n\pi-\alpha| \approx \varphi$, where φ is the angle formed by the normals to the planes onto which NDI and thiophene units can be thought to lay, approximately. The last column reports the variation Δ of this measure from $\mathbf{1}^-$ to $\mathbf{1}^-\mathbf{Li}^+$.

that a higher charge delocalization is also a property of models longer than a monomer. This is probably due to the presence of multiple positive-charge centers that spread the excess charge over the crystal. Finally, we find that the periodic model conserves the $\mathrm{OLi}-\pi$ interaction found in the molecular model.

Extension to other doping agents. The effect on structural relaxation of alkali metals different from lithium can also be taken into account. In Figure 3.18 we compare the NDI and T2 regions of the bondplots of $\mathbf{1}^-\mathbf{Li}^+$, $\mathbf{1}^-\mathbf{Na}^+$, and $\mathbf{1}^-\mathbf{K}^+$. As in the case of lithium, the attachment of sodium and potassium does not affect the conformation of the alkyl chains. On the other hand, both the extent and delocalization of structural relaxation depend on the doping agent. In particular, as the ionic radius of the n-dopant is increased:

- The structural relaxation is less localized on the NDI unit and involves the T2 units as well.
- The bond-length variations become smaller in the regions near the attachment site.

These observations can be rationalized by recalling that the doping agent limits charge delocalization acting as a positive-charge center. Then larger atomic radii increase the charge delocalization of the excess charge donated to the polymer due to the larger screening effect on the positive nuclear charge of the cationic dopant. As a consequence, the density of excess charge decreases in the regions near the doping agent, resulting in smaller bond-length variations.

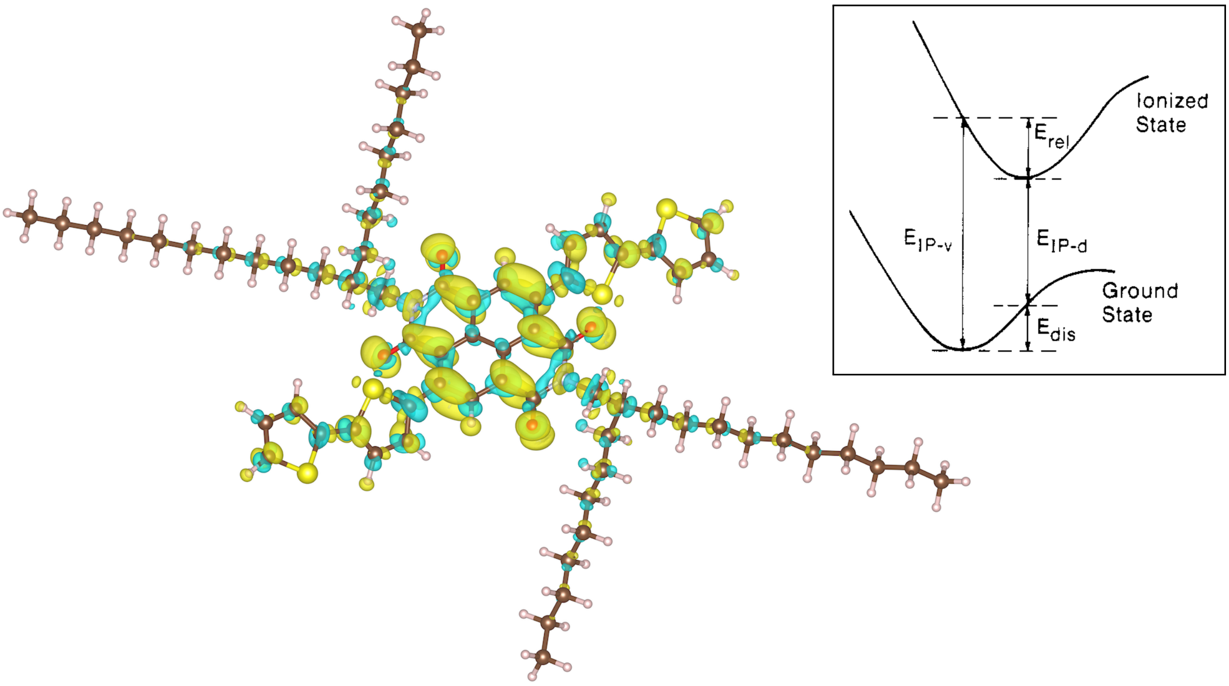

Figure 3.16: Isosurface of the electron-density difference between $\mathbf{1}^-$ and $\mathbf{1}^-$ in the geometry of $\mathbf{1}$. The electron-density difference is positive in yellow regions, negative in blue regions. The isosurface has been taken at `0.001` a_0^{-3}. Inset: representation of the transformation associated with this electron-density difference. In particular, we are concerned with the transformation with energy variation $\mathrm{E}_{\mathrm{IP-V}}$, from the ground state to the ionized state. Reproduced from Ref. [11].

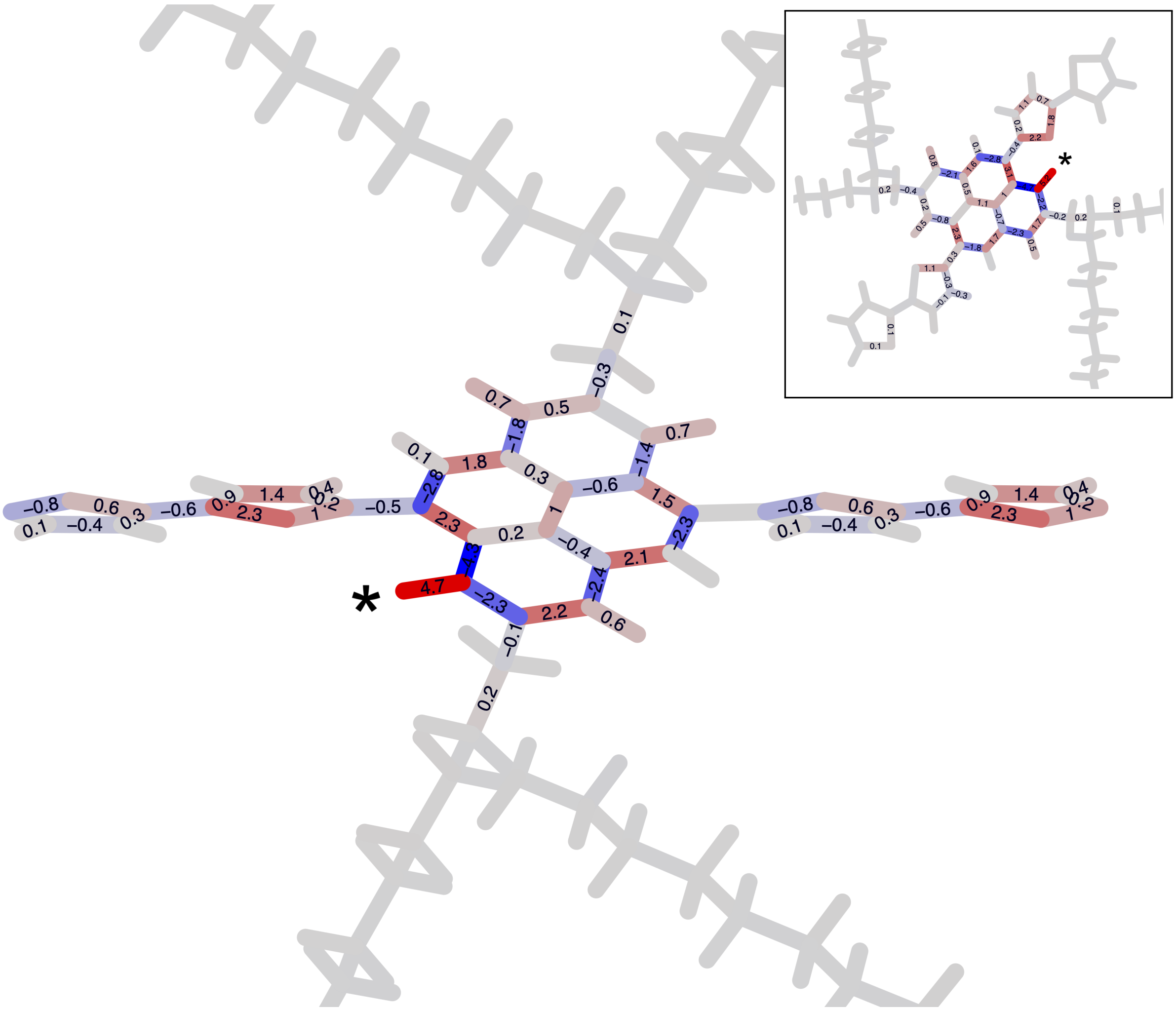
0.1
−0.3
0.7
0.5
0.7
−1.8
−1.4
0.1
1.8
0.3
−0.6
−2.8
1
1.5
−0.8
0.6
0.3
−0.6
0.9
1.4
0.4
0.2
−0.5
2.3
1
0.1
−0.4
2.3
0.2
−0.4
2.1
−2.3
*
4.7
−2.3
−2.4
2.2
0.6
−0.1
0.2
−0.8
0.6
0.3
−0.6
0.9
1.4
0.4
0.2
2.3
1
0.1
−0.4
*

Figure 3.17: Bondplot of a portion of $\mathbf{1}^{-}\mathbf{Li}^{+}$–PBC: bond-length differences between $\mathbf{1}^{-}\mathbf{Li}^{+}$–PBC and $\mathbf{1}$–PBC. In this plot, the asterisk indicates the lithiation site. Differences are reported in pm. Only differences whose absolute value is equal to or larger than 0.1 pm are shown. Inset: portion of Figure 3.13, where the bondplot of $\mathbf{1}^{-}\mathbf{Li}^{+}$ is shown.

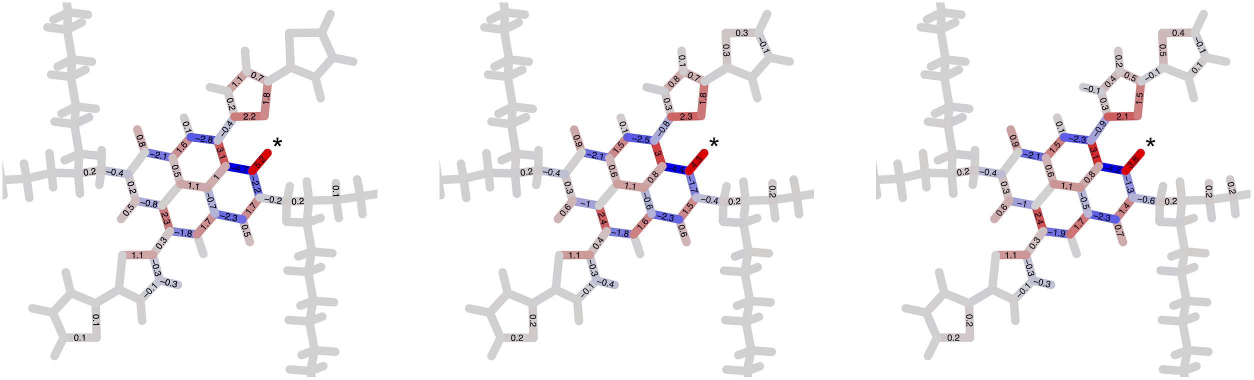

(a) $\mathbf{1^{-}Li^{+}}$ **(b) $\mathbf{1^{-}Na^{+}}$** **(c) $\mathbf{1^{-}K^{+}}$**

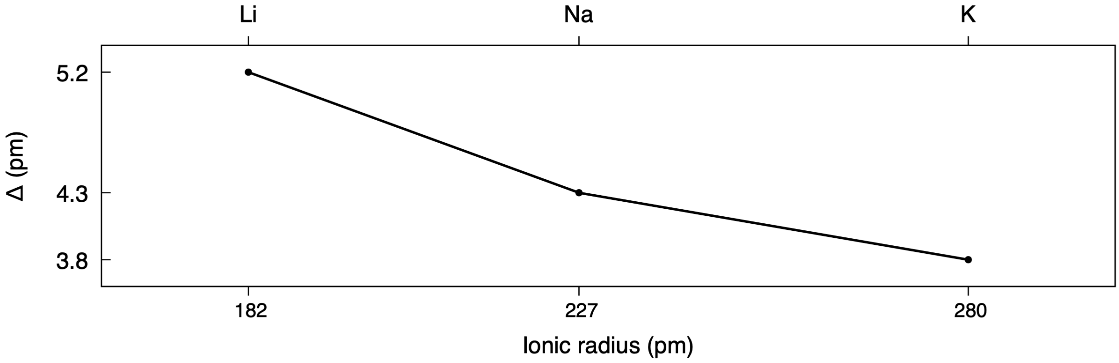

(d) $\mathbf{1^{-}Na^{+}}$

Figure 3.18: (a, b, c) Bondplots of molecular models of N2200 with different alkali metals as n-doping agents: bond-length differences between n-doped models and **1**. In these plots, asterisks indicate the attachment sites of alkali metals. Differences are reported in pm. Only differences whose absolute value is equal to or larger than 0.1 pm are shown. (d) Bond-length difference Δ of the C−O bond in the lithiation site at different ionic radii.

3.3 Chapter conclusions

In this Chapter, we have investigated the relaxation of the structure of N2200 arising from its n-doping through lithiation. We conclude the following:

1. When attached to a carbonyl group of N2200, lithium acts as an n-doping agent donating almost completely its valence electron.
2. The attachment of lithium stabilizes the n-doped species reducing the energy of its SOMO below the energy of the SOMO of the anionic species in the absence of the attached doping agent.
3. The n-doping of N2200 results in the partial localization of the excess charge, which mainly localizes on the central NDI unit and on the nearby T2 unit. The n-doping does not affect the alkyl chains. Such an effect implies a partial localization of the structural relaxation as well, which arises from the perturbation of the electron density. This is the evidence of the polaron localization in the NDI unit.
4. When lithium is attached to the carbonyl group near the T2 unit, it interacts with a thiophene ring through an $\mathrm{OLi} - \pi$ interaction. This causes a partial charge transfer to that thiophene ring.
5. The presence of lithium induces a structural relaxation pattern which differs from that of the anionic species. In particular, lithium attachment makes bond-length variations less homogeneous and more localized in the NDI unit. The structural relaxation is also influenced by the $\mathrm{OLi} - \pi$ interaction.
6. The computed structural relaxation is well rationalized based on the spin density of the lithiated molecular model and on the difference between the electron densities of the anionic species and the anionic species in the geometry of the neutral species.
7. The models with periodic boundary conditions give a slightly different picture of charge delocalization. In particular, it is found that structural relaxation is less localized in a periodic one-dimensional lithiated crystal than in a molecular model.
8. By substituting lithium with other alkali metals, it is found that atomic dopants with larger ionic radii lead to a more homogeneous and extended charge delocalization.

Chapter 4

Functionalized graphene nanoribbons

> *And lo, what was that? One of the snakes grabbed its own tail and the image whirled mockingly before my eyes.*
>
> — August Kekulé, on his discovery of the benzene ring

In Chapter 1, graphene nanoribbons (GNRs) have been introduced as portions of graphene characterized by a nanometric width, for which π stacking in solution can be avoided by edge functionalization. The correct functionalization of GNRs can be studied by spectroscopic techniques. In this Chapter we assign the most prominent features of IR, Raman and UV-Vis spectra of GNRs for a selection of functional groups. We refer to a recent study [53], where functionalized ribbons are referred to as GNR–AOM, being A and OM two substituents introduced in the following. It is useful to recall that both IR and Raman spectroscopy have been identified as useful tools for the study of edge functionalization of graphene nanoribbons [76, 77]. We will be also concerned with the radial breathing-like mode (RBLM) of GNRs. This is a Raman feature of GNRs observed in the low-frequency region. The correspondent vibrational normal mode is schematically represented in Figure 4.1. The fact that the frequency of the RBLM depends on the reciprocal of the square root of the width of the GNR makes it a useful characterization tool [78].

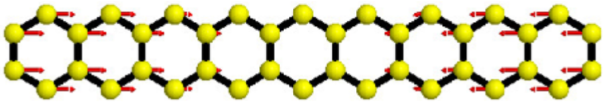

Figure 4.1: Schematic representation of the RBLM of a GNR. Reproduced from Ref. [12].

4.1 The computational model

To assign the IR, Raman, and UV-Vis spectra of GNR–AOM, we consider the following models. Some of them are molecular models (within the so-called oligomer approach [79]), other are models with periodic boundary conditions (PBCs).

1. Figure 4.2 shows the equilibrium geometries of fully hydrogenated oligomers of increasing length. We call these molecules $[n]$GNR–H, where n is the number of repeat units. These molecular models are used to study the vibrational and electronic properties of GNR–AOM which are independent of the substituents. As a matter of convenience, fully hydrogenated models are here represented for only selected values of n. In this Chapter, models with $n = 3, 4, 5, 6, 8, 9, 11, 13$ are considered. Concerning vibrational spectroscopy, the aim of these hydrogenated models is to draw general conclusions on the out-of-plane vibrational bending modes, and they are not to be compared with IR experimental data.

2. Figure 4.3 represents a tetramer functionalized with four anthracenyl (A) groups and four N-n-octadecyl maleimide (OM) groups, which we call [4]GNR–[4]A[4]OM. The choice of both the concentration and the random disposition of A and OM in this model are based on the fact that the chemical synthesis of GNR–AOM does not control the position of the substituents along the GNR. Thus, GNR–AOM can be referred to as atactic. Moreover, this particular disposition of the substituents allows us to take into account possible couplings between different neighboring groups.

3. Figure 4.4 shows oligomers of different lengths and one repeat unit of a model to which PBCs are applied. We refer to these models respectively as $[n]$GNR–A and GNR–A–PBC. These models with only one type of substituent are used to evidence the vibrational markers related to only A. The periodic model is also used as a benchmark for the applicability of the oligomer approach.

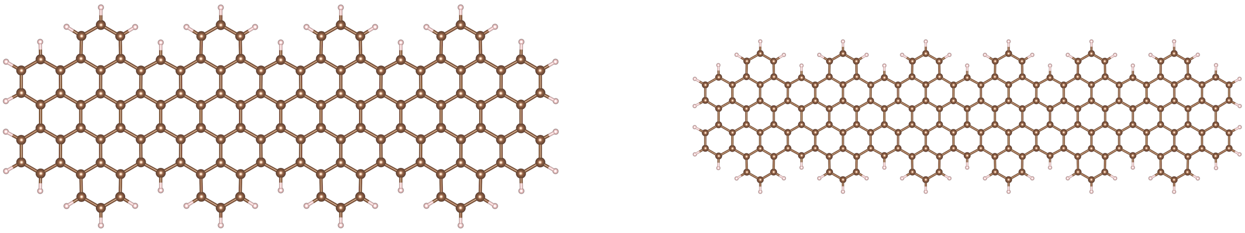

(a) [4]GNR–H **(b)** [6]GNR–H

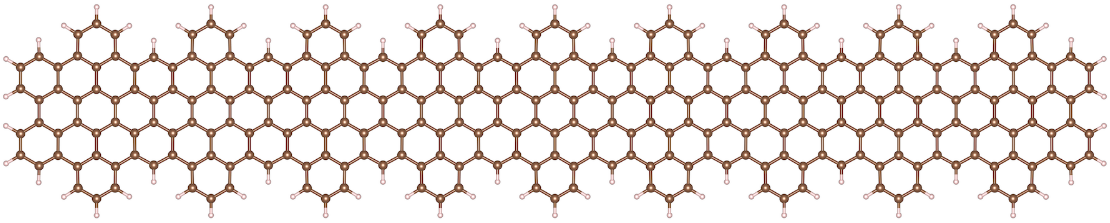

(c) [9]GNR–H

Figure 4.2: Molecular models of fully hydrogenated GNRs.

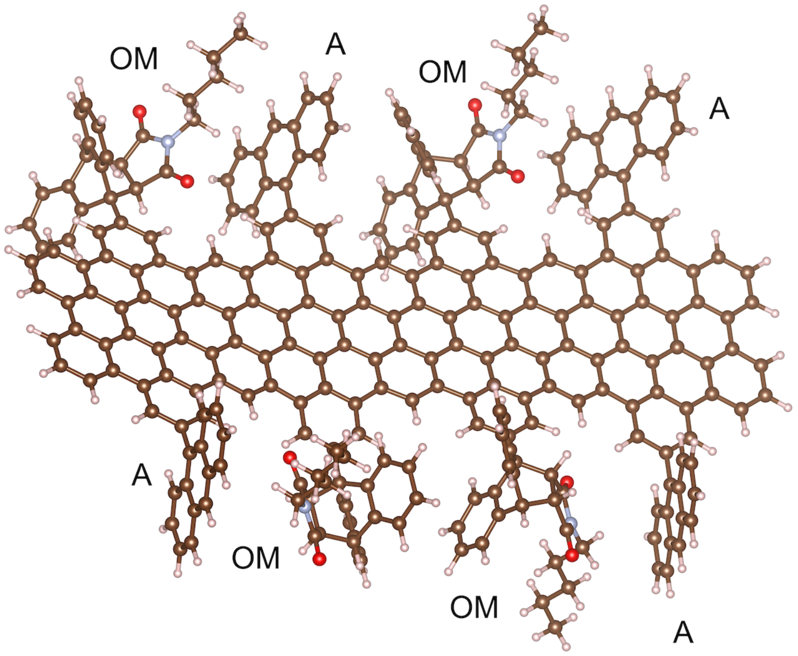

(a) [4]GNR–[4]A[4]OM

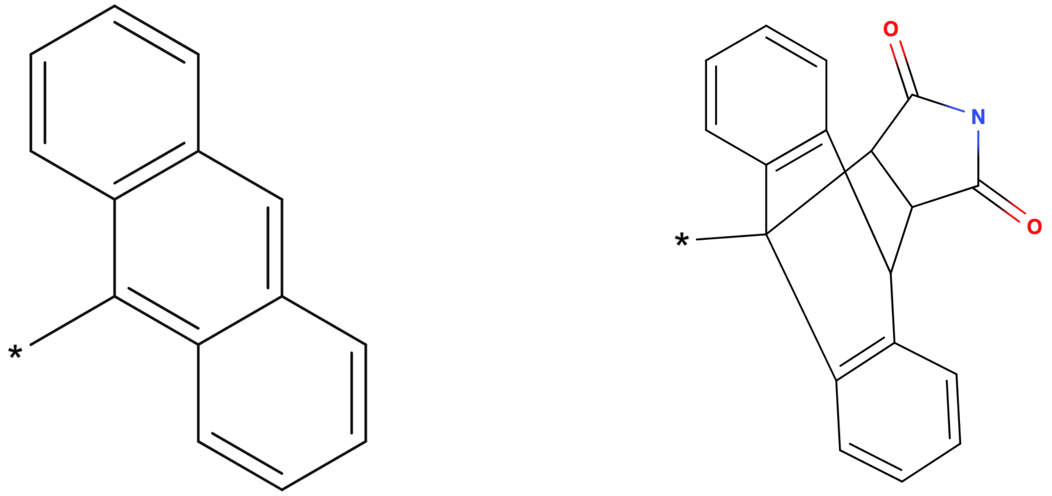

(b) A **(c)** OM

Figure 4.3: Molecular model of a GNR functionalized with A and OM, and their structural formulae. In panel (a) the substituents are indicated. In panels (b) and (c) asterisks indicate the attaching sites.

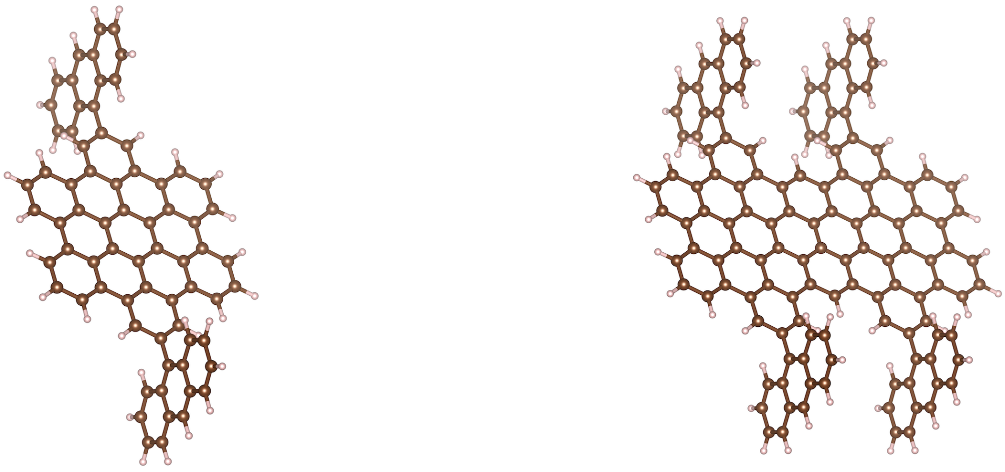

(a) [1]GNR–A **(b)** [2]GNR–A

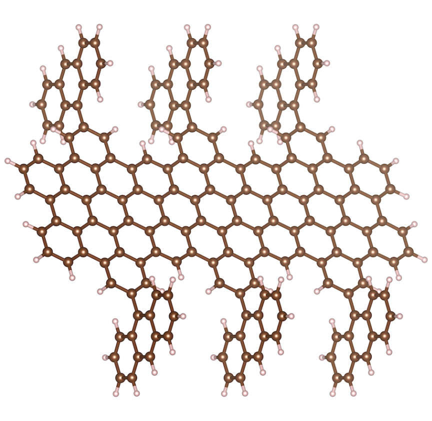

(c) [3]GNR–A **(d)** GNR–A–PBC

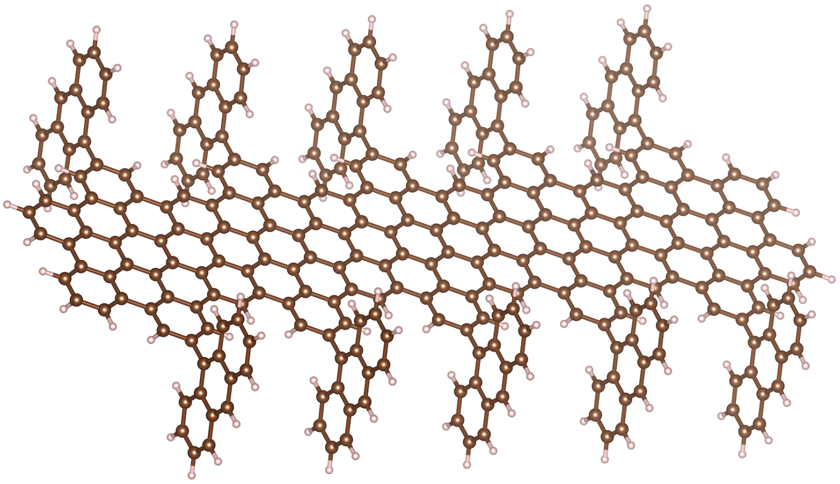

(e) [5]GNR–A

Figure 4.4: Molecular and periodic models of GNRs functionalized with A groups. In panel (d), a repeat unit of GNR–A–PBC is represented.

4.2 Results and discussion - IR

We begin with the assignment of the experimental IR spectrum of Figure 4.5, where four features are put in evidence in the region of the CH out-of-plane bending which was shown to be useful in the characterization of other GNRs [76]. Considering both hydrogenated and functionalized molecular models, we can study the effect of the substituents on the vibrational properties of GNRs.

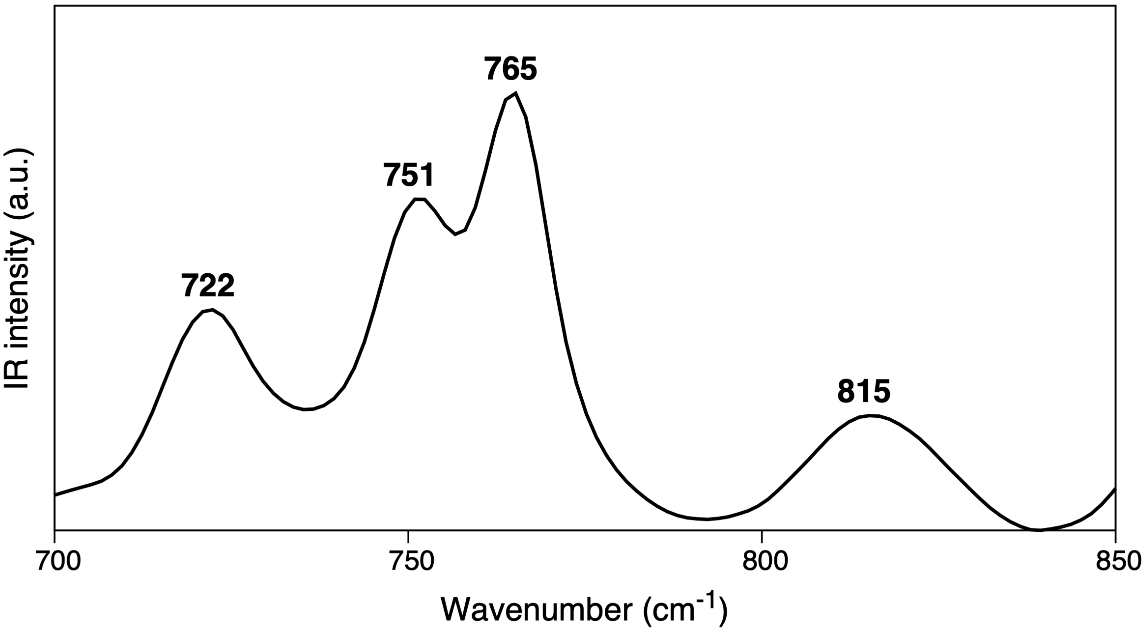

Figure 4.5: Experimental IR spectrum of GNR–AOM (courtesy of Dr. Junzhi Liu, The University of Hong Kong). The most intense bands are labelled with their corresponding wavenumbers in cm^{-1}.

Hydrogenated models. The left panel of Figure 4.6 shows the simulated IR spectra of [n]GNR–H models. The computed spectra are characterized by two relatively intense bands at 755 cm^{-1} and 792 cm^{-1}, with a weak feature at 714 cm^{-1}. We immediately notice that the spectra undergo frequency dispersion with the length of the model up to $n = 6$, as shown in the top right panel. We can thus focus our attention on [6]GNR–H and consider the vibrational normal modes associated with these three features. In Table 4.1, atomic displacements are represented following two conventions, either by means of black arrows or using red arrows together with blue and green segments, which symbolize stretching and shortening bonds. We observe that:

- The feature at 714 cm^{-1} is associated with the displacement of terminal hydrogens and in-plane deformations in the backbone of the GNR. Given this partial terminal nature and the relative low IR intensity of the in-plane normal mode, we expect this feature to almost disappear in longer molecules.

- The feature at 755 cm^{-1} has a complete terminal nature, and should not be found for large values of n. As expected, the intensity of this feature decreases with respect to the band at 792 cm^{-1}, as shown in the bottom right panel of Figure 4.6.
- The feature at $\sim$ 792 cm^{-1} is due to CH out-of-plane bending modes in the regions nearest to the axis of the backbone. These are referred to as the *bay regions* of the GNR.

This analysis confirms the diagnostic role of this IR region for the structure of GNRs. Moreover, we notice that hydrogen-terminated edges lead to a simple IR spectrum in this region. In particular, in the CH out-of-plane region the IR spectrum possesses one edge vibrational marker and one terminal vibrational marker.

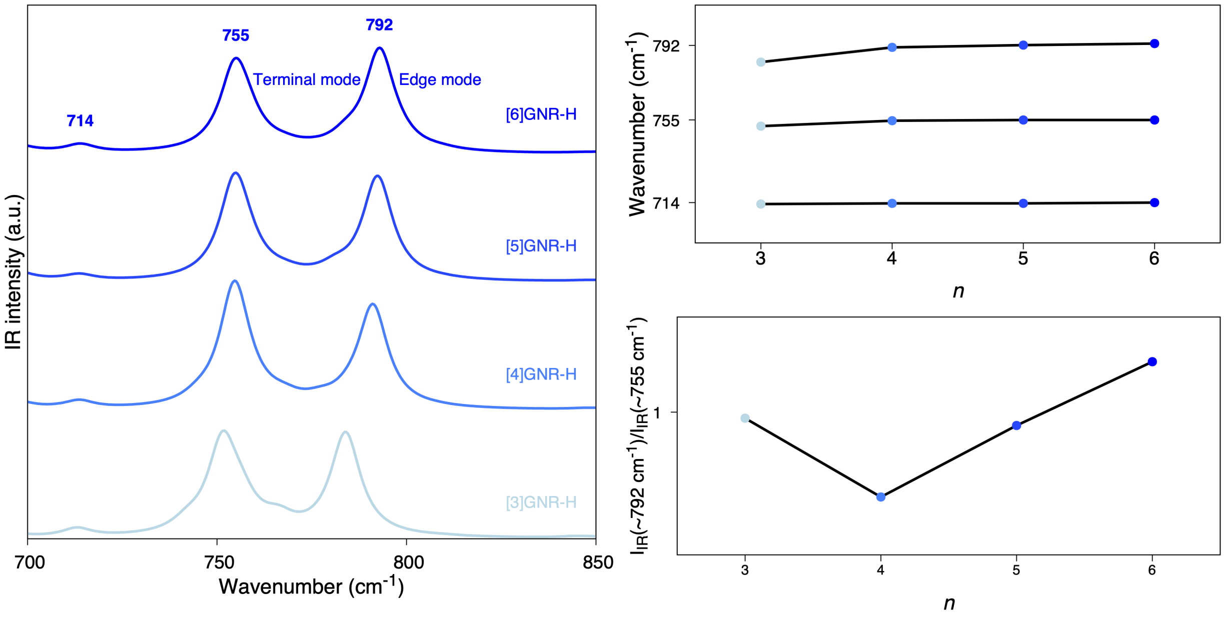

Figure 4.6: Left: simulated IR spectra of hydrogenated oligomers of GNRs. Three most intense simulated bands are labelled with their corresponding wavenumbers in cm^{-1}. Spectra are normalized on their maximum intensity in the represented interval. Top right: wavenumber dispersion of the most intense computed IR bands with respect to the length of the molecular models. Bottom right: ratio between the intensities of the two bands at $\sim$ 792 cm^{-1} and $\sim$ 755 cm^{-1} at different lengths of the molecular models.

Wavenumber (cm^{-1})	IR intensity (km/mol)	Nuclear displacements
713	6	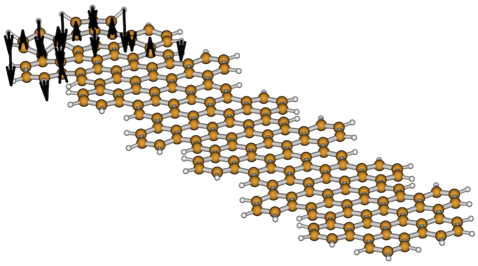
714	7	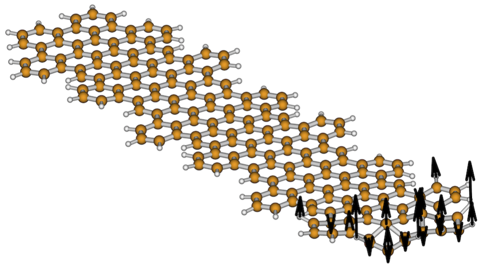
714	8	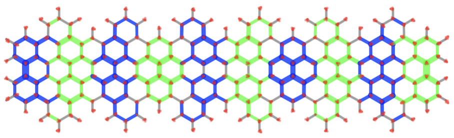

Table 4.1 - Continued on next page

Table 4.1 - Continued from previous page

Wavenumber (cm^{-1})	IR intensity (km/mol)	Nuclear displacements
755	101	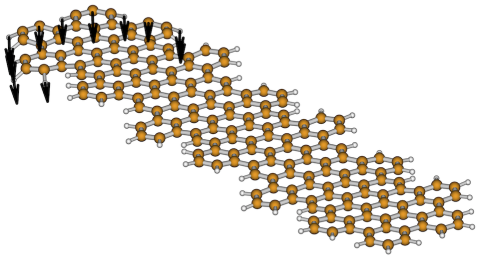
755	111	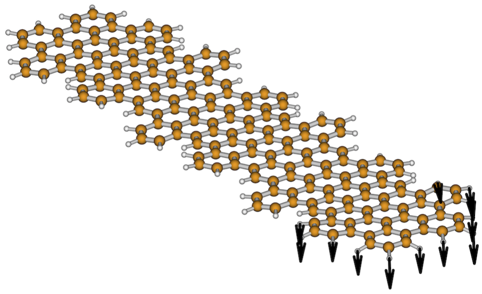
793	266	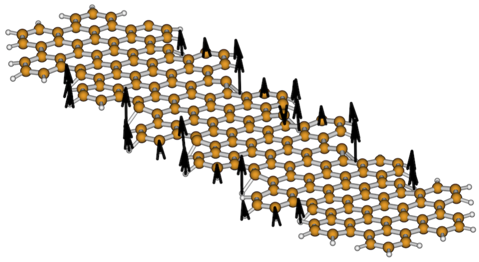

Table 4.1: Vibrational normal modes associated with the most intense features of the IR spectrum of [6]GNR–H. The last column represents the atomic displacements at a given instant of time of the vibration. Blue and green segments symbolize stretching and shortening bonds.

Functionalized model. The functionalized molecular model [4]GNR–[4]A[4]OM approaches the observed IR spectrum in in the CH out-of-plane bending region. This is shown in Figure 4.7, where we can see that the inclusion of the substituents introduces several vibrational features, compared to [n]GNR–H. We inspect the vibrational normal modes associated with the most intense features of the simulated spectrum, which are represented in Table 4.3. We recognize that:

- The peak at 724 cm^{-1} involves collective CH out-of-plane bending in the A groups.
- The band at 745 cm^{-1} is produced by CH out-of-plane bending on both the A and OM substituents.
- The feature at 759 cm^{-1} is due to CH out-of-plane bending and CH_2 twisting, both on the OM groups.
- The broad feature at 816 cm^{-1} arises from both collective in-plane deformation in the OM groups and out-of-plane CH bending in the A groups.
- Finally, the structured band at 834 cm^{-1} is due to collective out-of-plane bending of the A units, collective in-plane deformations in the OM groups, and CH out-of-plane bending in the bay regions of the GNR. Although at lower wavenumber, this latter is the only vibrational feature accounted for also by a fully hydrogenated model. This significant difference is caused by vibrational coupling of the CH of the bay region with the A and OM groups.

These observations allow us to assign the main features of the experimental IR spectrum of GNR–AOM as in Table 4.2.

Wavenumber (cm^{-1}) Experimental	Theoretical	Assignment
722	724	Collective CH out-of-plane bending in A groups
751	745	Collective CH out-of-plane bending in A and OM groups
765	759	Collective CH out-of-plane bending in OM groups, CH_2 twisting in OM, minor contribution from in-plane collective bending on A
815	816	Collective CH out-of-plane bending in A groups, collective in-plane deformations of the OM groups
815	834	Collective CH out-of-plane bending in A groups, collective in-plane deformations of the OM groups, CH out-of-plane bending at the GNR bay regions

Table 4.2: Assignment of the experimental IR spectrum of GNR–AOM.

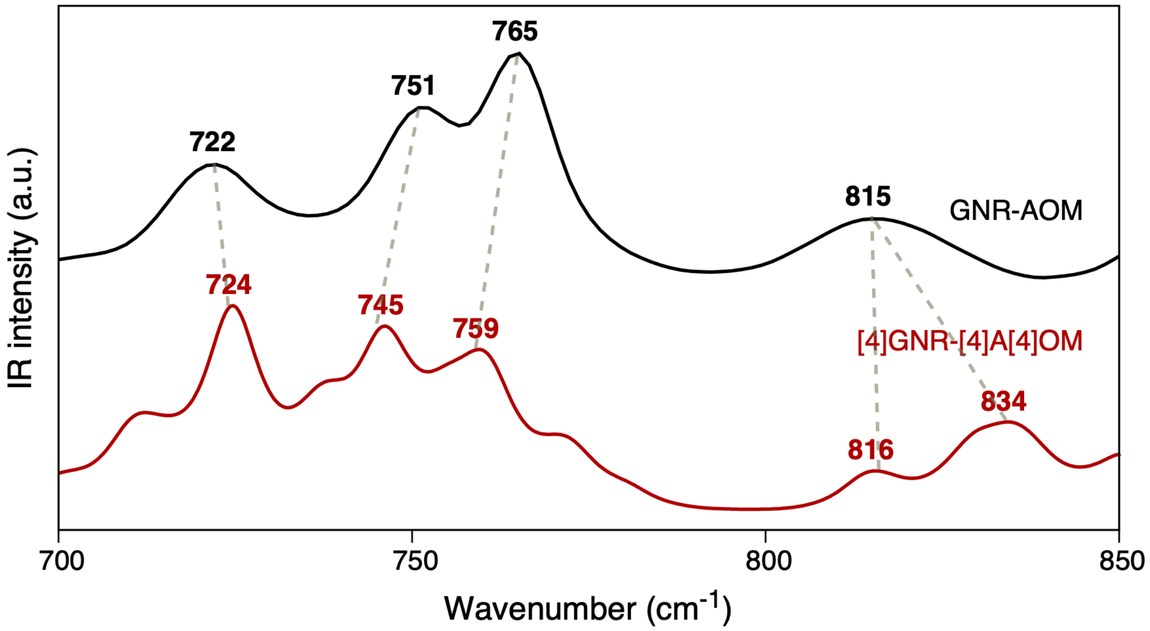

Figure 4.7: Simulated IR spectrum of [4]GNR–[4]A[4]OM compared with the experimental IR spectrum of GNR–AOM (courtesy of Dr. Junzhi Liu, The University of Hong Kong). Dotted lines highlight the assignment of the most prominent IR features. In both spectra, the most intense features are labelled with their wavenumber in cm^{-1}. Spectra are normalized on their maximum intensity in the represented interval.

Wavenumber (cm^{-1})	IR intensity (km/mol)	Nuclear displacements
724	66	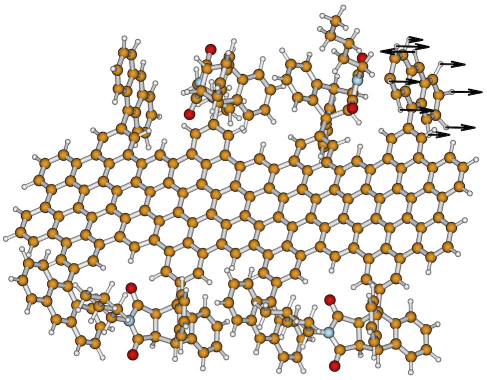

Table 4.3 - Continued on next page

Table 4.3 - Continued from previous page

Wavenumber (cm^{-1})	IR intensity (km/mol)	Nuclear displacements
746	94	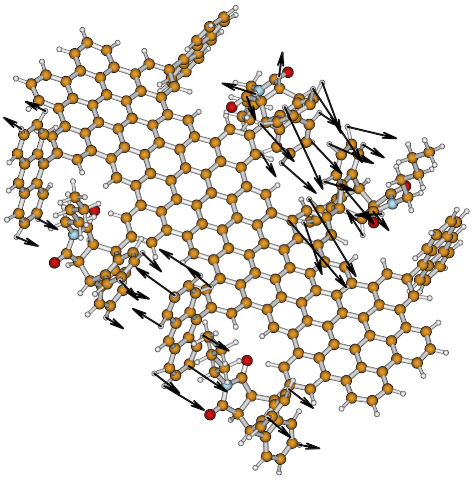
755	40	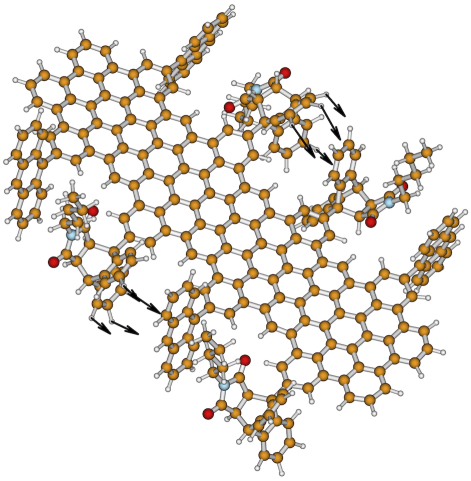
814	11	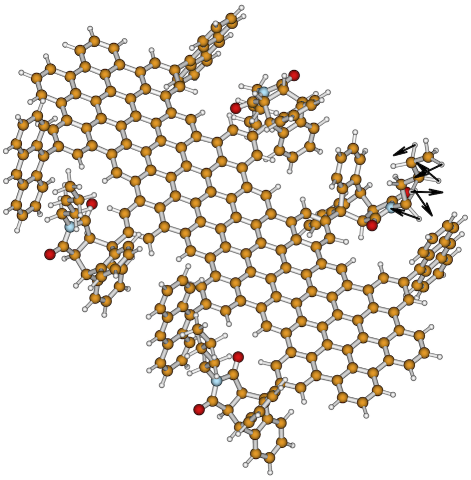

Table 4.3 - Continued on next page

Table 4.3 - Continued from previous page

Wavenumber (cm^{-1})	IR intensity (km/mol)	Nuclear displacements
814	12	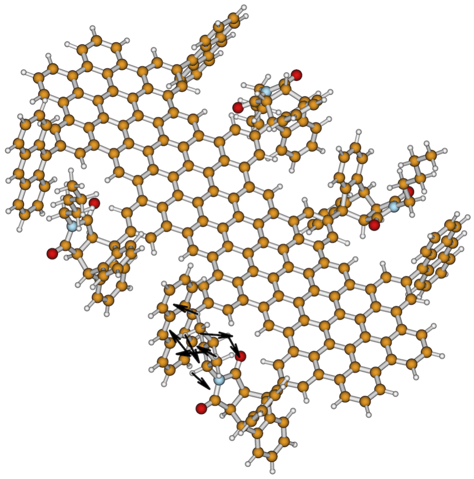
835	33	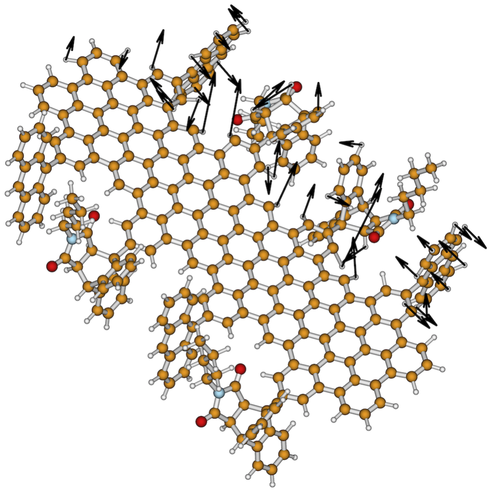

Table 4.3: Vibrational normal modes associated with the most intense features of the IR spectrum of [4]GNR–[4]A[4]OM. The last column represents the atomic displacements at a given instant of time of the vibration.

Extension to periodic models. We can extend the approach followed above considering the models of Figure 4.4, and in particular of Figure 4.4d, where PBCs are applied. In Figure 4.8 the simulated IR spectra of these models are represented compared to the experimental one. Only some experimental features are reproduced by the simulated spectra, as expected because of the absence of the OM groups. From the inspection of the vibrational normal modes, we observe that:

- The feature at 722 cm^{-1} in GNR–A–PBC is related to collective CH out-of-plane bending in the A groups. In moving from shorter to longer oligomers, and finally considering PBCs, this peak undergoes frequency dispersion and shifts closer to the experimental spectrum. The same is true for the feature at 827 cm^{-1}, which is expected to contribute to the broad band at 815 cm^{-1} of the experiment.

- The feature at 780 cm^{-1} in GNR–A–PBC involves collective CH out-of-plane bending in the A groups, and is characterized by a relatively large dispersion of its frequency with respect to the length of the model. Due to its small IR intensity, this feature is hardly observed in the experiment.
- The peak at 815 cm^{-1} in [1]GNR–A increases in frequency with increasing n, becoming a contribution of the structured feature at 840 cm^{-1} in GNR–A–PBC.

From this analysis, we infer that:

1. Not always molecular models give a correct prediction of the IR vibrational frequencies of functionalized GNRs. Longer models are more reliable, because terminal effects are weaker. In some cases, the molecular approach is made suitable by a small frequency dispersion. This is the case of the CH out-of-plane bending at 722 cm^{-1}, which is correctly predicted by [1]GNR–A.
2. Some vibrational features of GNR–AOM are due to the interaction between A and OM groups. Indeed, a model containing only A substituents does not account for the experimental feature at 751 cm^{-1}, which we assign to the CH out-of-plane bending on both the A and OM substituents.

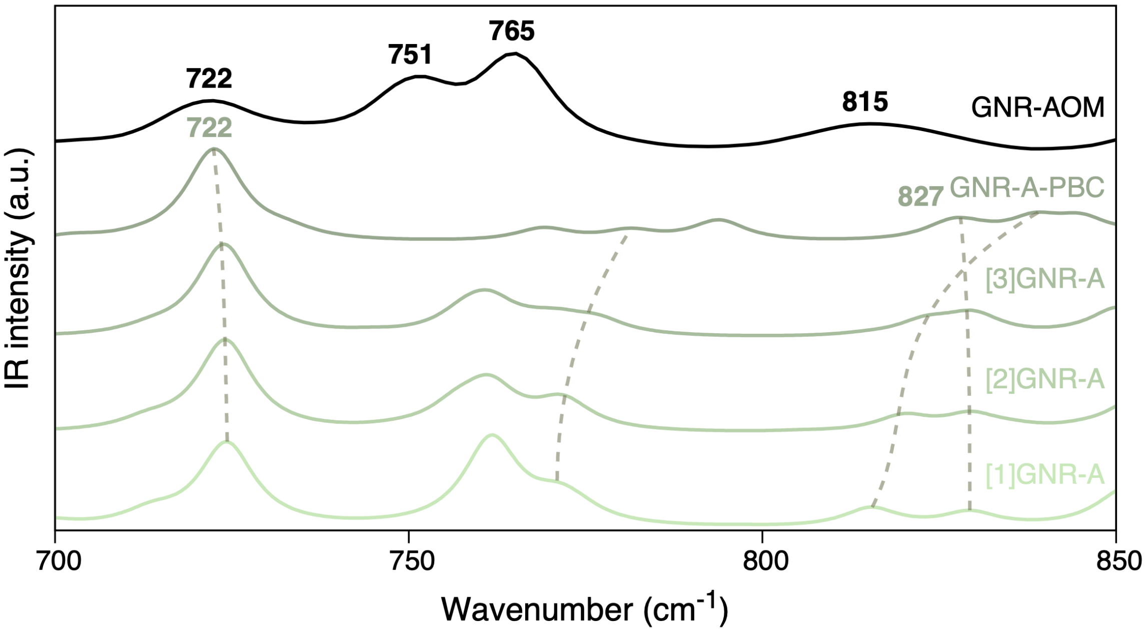

Figure 4.8: Simulated IR spectra of models of GNRs functionalized with A groups compared with the experimental IR spectrum of GNR–AOM (courtesy of Dr. Junzhi Liu, The University of Hong Kong). In the spectra of GNR–AOM and GNR–A–PBC, the most intense features are labelled with their wavenumber in cm^{-1}. Dashed grey lines help to visualize the dispersion of some features with respect to the length of the model. Spectra are normalized on their maximum intensity in the represented interval.

4.3 Results and discussion - UV-Vis

The UV-Vis spectrum of GNR–AOM is represented in Figure 4.9a. As expected for a highly $\pi-$conjugated polymer, this experimental spectrum displays several features in the visible range [80]. Two of such features can be assigned by simulating the UV-Vis spectra of fully hydrogenated and functionalized molecular models, which are represented in Figure 4.9b. There we see that the most prominent peak red-shifts with increasing length of the model. Figure 4.9c shows that this dispersion is almost arrested at $n = 13$, so that [13]GNR–H can be adopted to assign the experimental UV-Vis features. The UV-Vis spectrum of [13]GNR–H has a prominent peak at 549 nm and a weak shoulder at $\sim$ 472 nm. These two can be immediately put in correspondence with the experimental UV-Vis features respectively found at 541 nm and 472 nm.

In Figure 4.9a we also notice that functionalization causes a redshift of the simulated UV-Vis spectrum at constant number of repeat units. The reason for this can be investigated considering the details of the molecular orbitals involved in the electronic excitation process. In Table 4.4 we see that the most intense UV-Vis peak is associated with the coupled

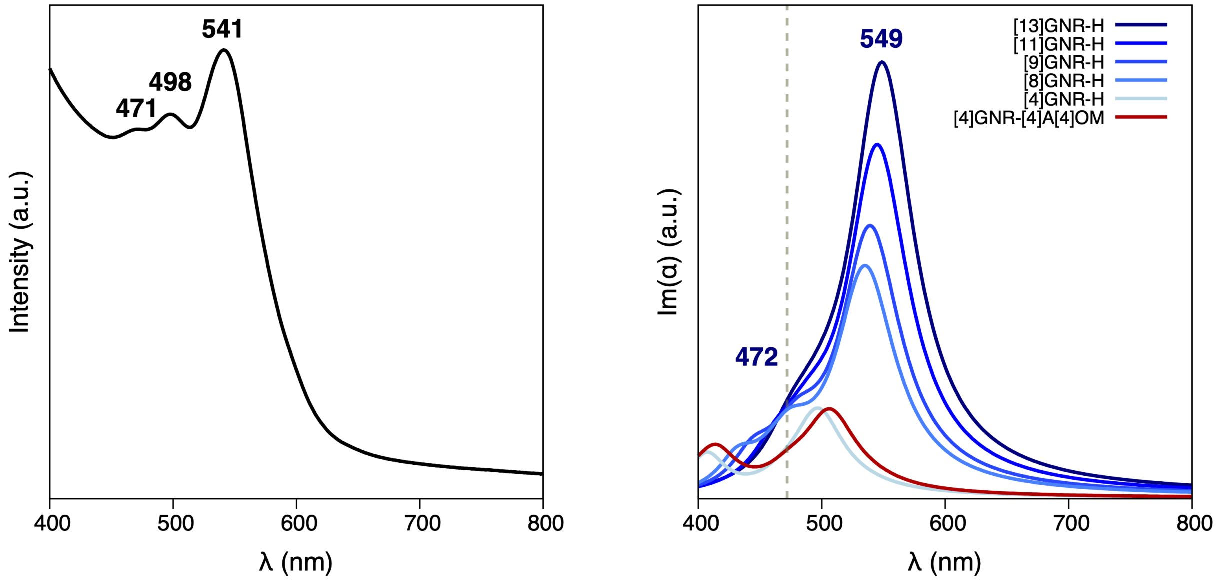

(a) GNR–AOM **(b)** [n]GNR–H, [4]GNR–[4]A[4]OM

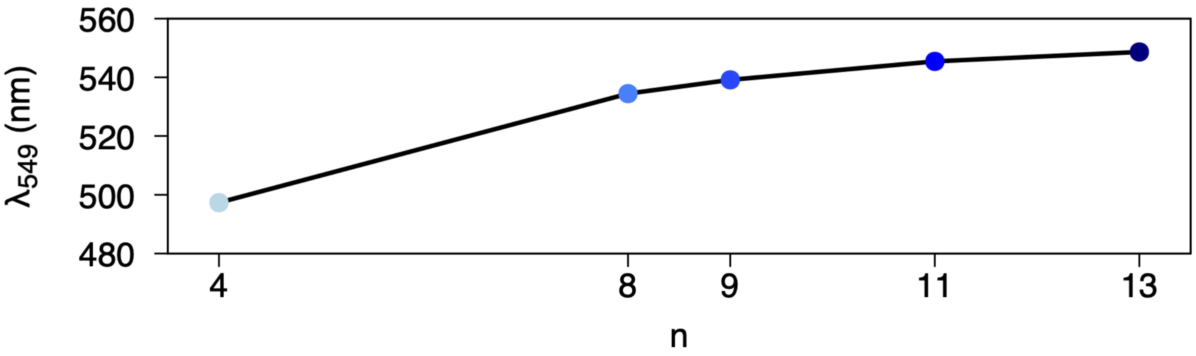

(c) [n]GNR–H

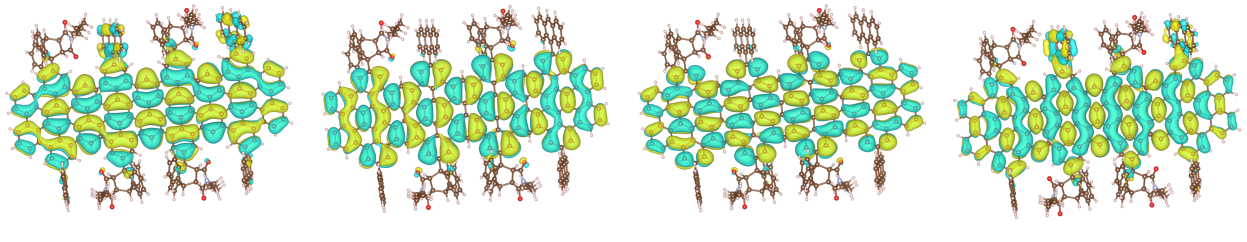

(d) HOMO−1, -4.88 eV **(e)** HOMO, -4.77 eV **(f)** LUMO, 2.16 eV **(g)** LUMO+1, -2.06 eV

Figure 4.9: (a) Experimental UV-Vis spectrum of GNR–AOM (courtesy of Dr. Junzhi Liu, The University of Hong Kong). (b) Simulated UV-Vis spectra of [n]GNR–H and [4]GNR–[4]A[4]OM models. (c) Dispersion of the peak at 549 nm in [13]GNR–H. (d-g) Isosurfaces of the FMOs of [4]GNR–[4]A[4]OM involved in the electronic transitions associated with the most prominent peaks of its UV-Vis spectrum. The FMOs are positive in yellow regions, negative in blue regions. Isosurfaces have been taken at $0.005\,a_0^{-3/2}$. In the UV-Vis spectra, the most intense features are labelled with their wavelength in nm. In particular, a dashed line helps to visualize the shoulder of the UV-Vis spectrum of [13]GNR–H.

HOMO−1 → LUMO+1 and HOMO → LUMO single excitations. Similarly, we find that the most important contributions to the feature at 472 nm involve electronic transitions from HOMO−1 and HOMO to LUMO+1 and LUMO. We can then understand the reason for the redshift of the UV-Vis spectrum of [4]GNR–[4]A[4]OM observing the topology of its frontier molecular orbitals (FMOs). In Figures 4.9d-4.9g we see that functionalization causes the FMOs to spread outside the graphenic backbone, increasing the conjugation of the whole molecule. In particular, we see that the A groups cause the largest increase in conjugation, leaving the OM groups with almost no effect. We can thus rationalize the trend observed in Figures 4.9b and 4.9c as follows:

1. Increasing the length of a fully hydrogenated molecular model, the FMOs involved in the electronic transitions at 474 nm and 543 nm spread onto larger regions. This leads to an increase of the conjugation of the molecule, which is known to cause a redshift of the UV-Vis spectrum [36].

2. Functionalizing a molecular model at constant length leads to an increase of conjugation as well, with the same effect discussed above.

Therefore, the effect of functional groups on the overall conjugation of the molecule is small. This is due to both the limited size of the A groups and their insertion on the backbone, which is almost orthogonal because of the steric hindrance of neighboring groups. As a result, fully hydrogenated molecular models are representative of two of the three UV-Vis experimental features of GNR–AOM.

λ nm	Oscillator strength	$i \to j$ excitation	$\delta P_{i\to j}$
543	0.12	HOMO−1 → LUMO+1	0.37
		HOMO → LUMO	0.58
474	0.72	HOMO−3 → LUMO+3	0.10
		HOMO−1 → LUMO+1	0.57
		HOMO → LUMO	-0.37

Table 4.4: Analysis of the electronic excitations associated with the UV-Vis features at 472 nm and 549 nm in the simulated spectrum of [13]GNR–H of Figure 4.9b.

The experimental peak at 498 nm is not reproduced by our models. This is likely to be a vibronic feature since it has not a counterpart in our calculations of vertical transition energies.

4.4 Results and discussion - Raman

We conclude this Chapter studying the Raman spectrum of GNR–AOM.

Hydrogenated models. On the left panel of Figure 4.10, the experimental Raman spectrum of GNR–AOM is compared with the computational ones of [n]GNR–H models. All of these spectra display the D and G peaks which are characteristic of graphenic materials [81, 82]. In the right panel, the frequency of the D peak of the theoretical spectra is reported as a function of the number of repeat units n. We see that the dispersion is small in passing from [5]GNR–H to [6]GNR–H, so that the latter can be chosen for further analysis. As expected, we find that the D and G peaks of [6]GNR–H are related to ring-breathing and ring-stretching vibrational normal modes, respectively, as illustrated in Table 4.5.

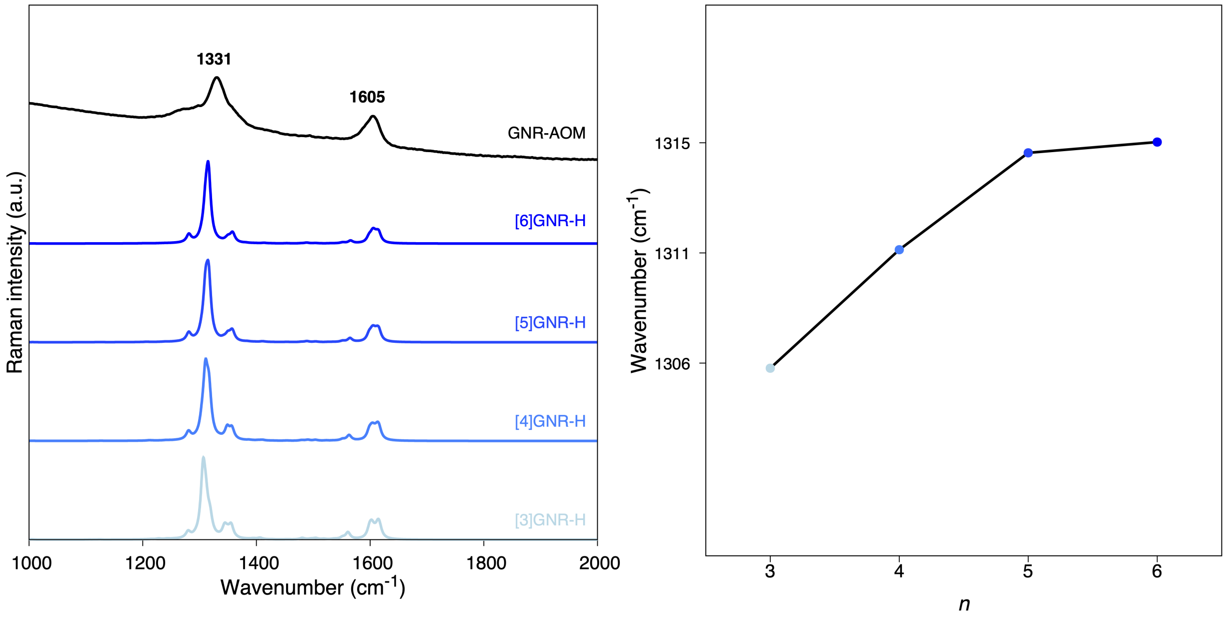

Figure 4.10: Left: simulated Raman spectra of hydrogenated oligomers of GNRs and experimental Raman spectrum of GNR–AOM (courtesy of Dr. Junzhi Liu, The University of Hong Kong). The D and G peaks of the experimental spectrum are labelled with their corresponding wavenumbers in cm^{-1}. Spectra are normalized on the intensity of the D peak. Right: wavenumber dispersion of the computed D peak with respect to the length of the molecular models.

Wavenumber (cm^{-1})	Raman activity (Å^2/amu$^{1/2}$)	Nuclear displacements
1310	138375	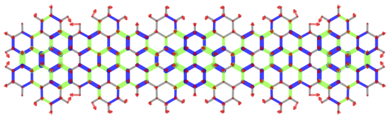
1566	12534	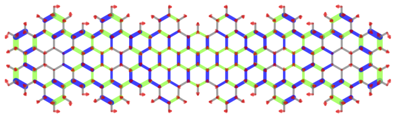

Table 4.5 - Continued on next page

Table 4.5 - Continued from previous page

Wavenumber (cm^{-1})	Raman activity (Å^2/amu$^{1/2}$)	Nuclear displacements
1606	29869	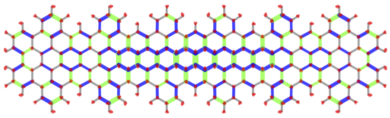

Table 4.5: Vibrational normal modes associated with the D and G peaks of [6]GNR–H. The last column represents the atomic displacements at a given instant of time of the vibration. Blue and green segments symbolize stretching and shortening bonds.

Functionalized model. The effect of the substituents on the Raman spectrum of GNR–AOM is accounted for by the [4]GNR–[4]A[4]OM model. Figure 4.11 shows a comparison between its simulated Raman spectrum and the experimental one. It is possible to see that the D and G peaks are still well reproduced, both in their overall shape and frequency. However, a comparison with Figure 4.10 shows that the substituents perturb the Raman spectrum, causing the two peaks to become more structured. As shown in Table 4.6, the reason for this is that in [4]GNR–[4]A[4]OM the ring-breathing and ring-stretching vibrational modes couple with the substituents in several different ways. This coupling effect induced by the presence of the substituents fully agrees with that discussed for the assignment of the UV-Vis spectrum of GNR–AOM. Consistently, we find that the effect of the substituents on the Raman spectrum of GNR–AOM is small, similar to the small conjugation modulation induced by the substituents on the GNR.

Wavenumber (cm^{-1})	Raman activity (Å^2/amu$^{1/2}$)	Nuclear displacements
1314	39203	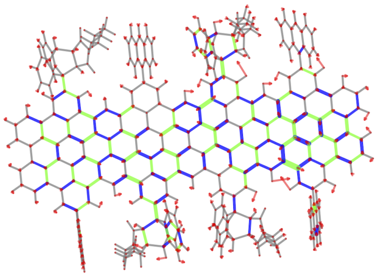
1323	68156	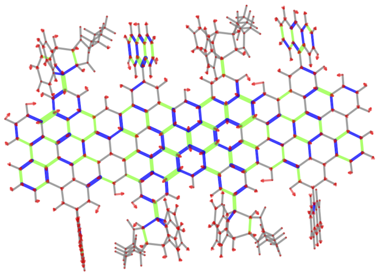

Table 4.6 - Continued on next page

Table 4.6 - Continued from previous page

Wavenumber (cm^{-1})	Raman activity ($\mathring{A}^2/amu^{1/2}$)	Nuclear displacements
1586	13842	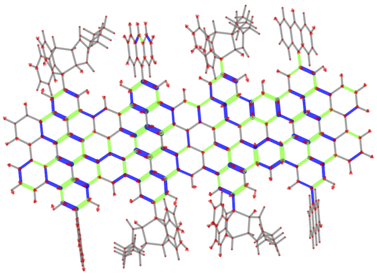
1607	11577	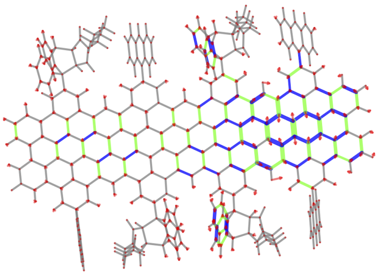
1610	18366	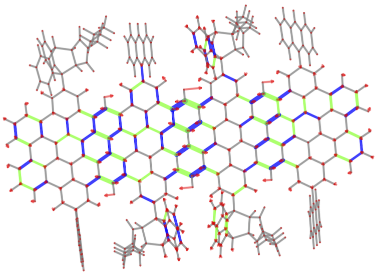
1611	2382	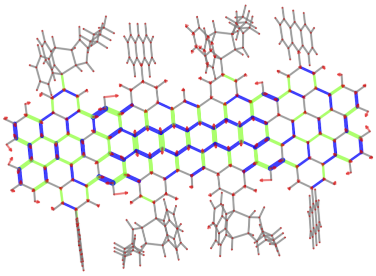

Table 4.6: Vibrational normal modes associated with the D and G peaks of [4]GNR–[4]A[4]OM. The last column represents the atomic displacements at a given instant of time of the vibration. Blue and green segments symbolize stretching and shortening bonds.

Radial breathing-like mode. The experimental spectrum of GNR–AOM displays a radial breathing-like mode (RBLM) at 252 cm^{-1}, as shown in Figure 4.12. The same feature is shown by [n]GNR–H models, but at a significantly higher wavenumber ($\sim 308\,cm^{-1}$). This effect is not related to the finite length of the molecular models, since the wavenumber dispersion of the RBLM feature is already negligible for [6]GNR–H. On the contrary, this is likely to be a mass effect related to the presence of the substituents in GNR–AOM. The same single RBLM

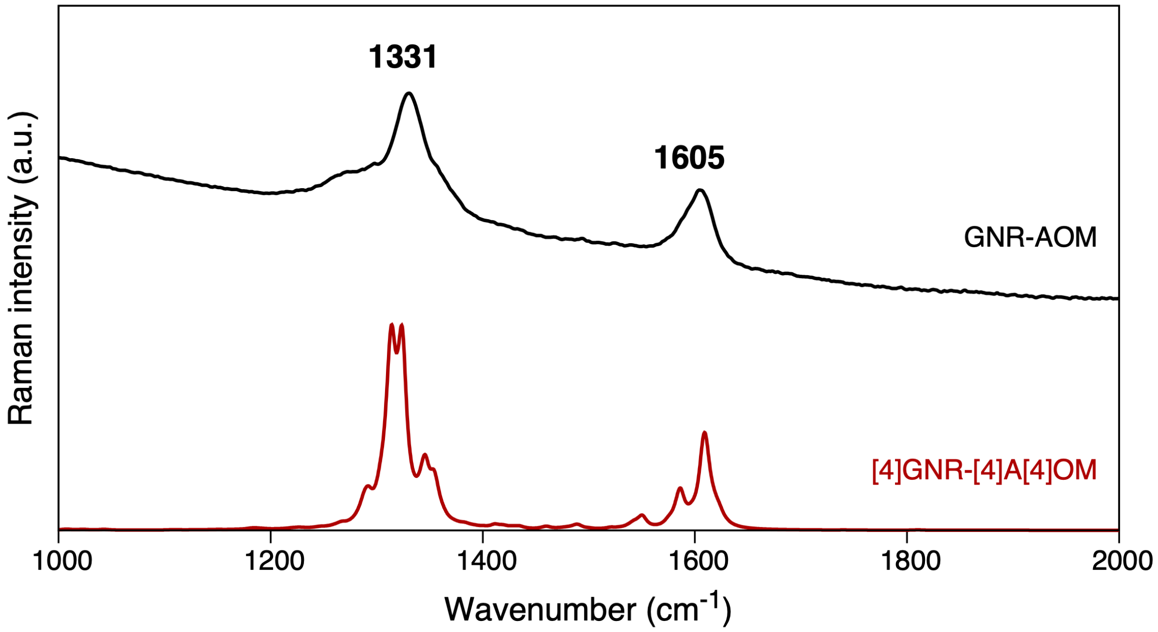

Figure 4.11: Simulated Raman spectrum of [4]GNR–[4]A[4]OM compared with the experimental Raman spectrum of GNR–AOM (courtesy of Dr. Junzhi Liu, The University of Hong Kong). The D and G peaks of the experimental spectrum are labelled with their corresponding wavenumbers in cm^{-1}. Spectra are normalized on the intensity of the D peak.

feature is hardly found in [4]GNR–[4]A[4]OM. Similar to the case of the D and G peaks, the [4]GNR–[4]A[4]OM model possesses several RBLM features at low wavenumbers, coupled with collective vibrations of the A and OM groups. Therefore, a precise assignment of the RBLM feature of GNR–AOM cannot be done with a single model of [4]GNR–[4]A[4]OM.

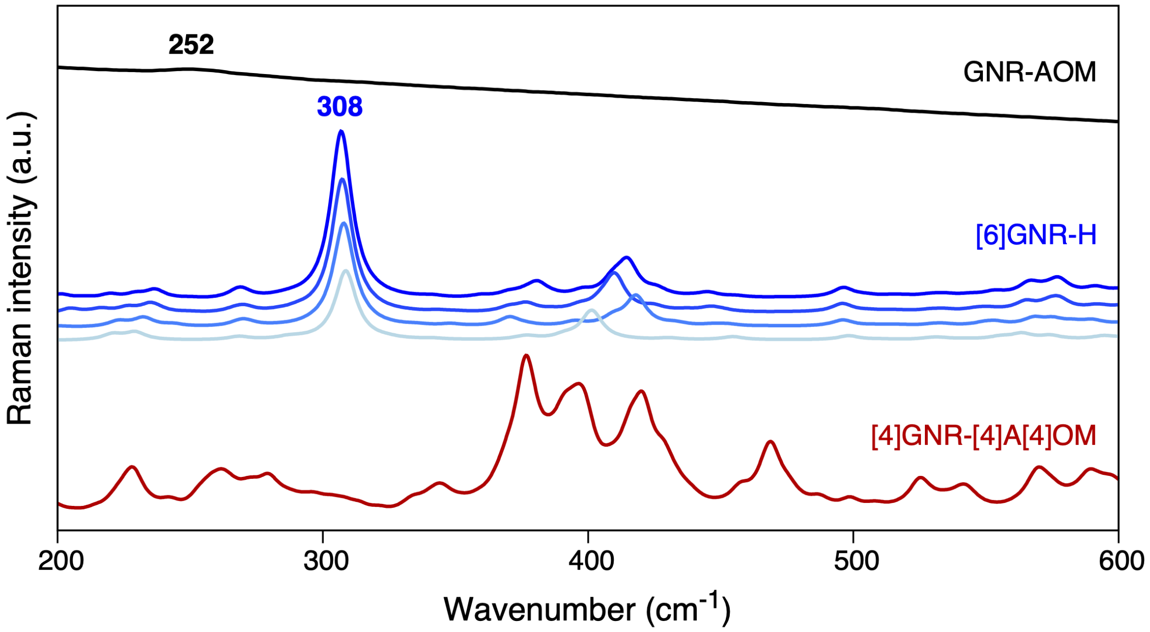

Figure 4.12: From top to bottom: experimental Raman spectrum of GNR–AOM (courtesy of Dr. Junzhi Liu, The University of Hong Kong), simulated Raman spectra of [6]GNR–H, [n]GNR–H models with $n = 5, 4, 3$, and [4]GNR–[4]A[4]OM. The RBLM features of GNR–AOM and [6]GNR–H are labelled with their corresponding wavenumbers in cm^{-1}. All spectra except those of [n]GNR–H models are normalized with respect to the most intense feature of the represented interval. The spectra of [n]GNR–H models are normalized with respect to the intensity of the RBLM feature of [6]GNR–H.

4.5 Chapter conclusions

In this Chapter, we have assigned the experimental IR, UV-Vis, and Raman spectra of GNRs functionalized with A and OM groups. The following can be concluded:

1. The IR spectrum of GNR–AOM in the CH out-of-plane bending region between 700 cm^{-1} and 850 cm^{-1} is highly influenced by functionalization. In particular, we find that the feature at 722 cm^{-1} is a chemical marker of A; the feature at 751 cm^{-1} is a marker of the coupling between A and OM; the feature at 765 cm^{-1} is a chemical marker of OM; the broad feature at 815 cm^{-1} is related to several IR transitions, namely collective CH out-of-plane bending in A groups, in OM groups and at the GNR bay regions.

2. Although the oligomer approach correctly predicts the vibrational IR features of GNR–AOM, the reliability of the simulated IR spectrum increases by taking into account a periodic model.

3. The UV-Vis spectrum of GNR–AOM is partially reproduced by a fully hydrogenated molecular model, and two of its most prominent peaks are associated with electronic

transitions between FMOs. Substituents have a small redshift effect on the UV-Vis spectrum. This is a consequence of the small electronic coupling between the graphenic backbone and the functional groups, as results from the topology of the FMOs.

4. One feature of the experimental UV-Vis spectrum is not accounted for by our models. We infer that such a feature is vibronic, and not predictable by the selected first-order theoretical approach which considers vertical transitions only. Further calculations of Franck-Condon factors would be necessary to shed light on this point, but are cumbersome due to the complexity of the system.

5. The Raman spectrum of GNR–AOM shows the D and G peaks typical of graphenic molecules. Functionalization results in the broadening of those features since, because of vibrational coupling between the GNR and the side groups, it introduces several Raman active vibrational modes at slightly different frequencies. This also agrees with the small $\pi-$electron coupling between the backbone and substituents found with the analysis of UV-Vis data.

6. The RBLM of GNR–AOM is poorly explained by our models. This is because fully hydrogenated models lack the mass effect of the substituents, while [4]GNR–[4]A[4]OM does not display a single RBLM feature.

Chapter 5

PVDF

“Goodbye,” he said.
“Goodbye,” said the fox. “And now here is my secret, a very simple secret: it is only with the heart that one can see rightly; what is essential is invisible to the eye.”

— Antoine de Saint-Exupéry, *The Little Prince*

The piezoelectricity of the ferroelectric polymer polyvinylidene fluoride (PVDF) opens the possibility for the design of innovative electronic devices [46], but faces the fact that its piezoelectric phase β is not the most stable from the point of view of thermodynamics, so that crystallization from the melt does not lead spontaneously to piezoelectricity [9]. Given this fact, the copolymer poly (vinylidene fluoride-co-trifluoroethylene) (P(VDF−TrFE)), which is characterized by the random alternation of VDF and TrFE units and spontaneously crystallizes into its piezoelectric all-*trans* phase, is of large interest [47, 83]. However, the reasons for this behavior need further investigation in order to be unveiled. In this Chapter, we apply density functional theory (DFT) to show that markers of the TrFE unit and conformational disorder are found in the vibrational spectra, corroborating recent experimental results [2]. Then, we study the solid-state effects on the vibrational properties of PVDF.

5.1 The computational model

We will study the IR and Raman response of PVDF and P(VDF−TrFE) considering the models described below.

1. A PVDF macromolecule can be described in the first approximation as an isolated chain with chemical formula $CF_3{-}[CHCF]_n{-}CH_3$ of finite length n. This model is referred to as $n-$VDF, and is represented in the particular case of $n = 10$ in Figure 5.1a.

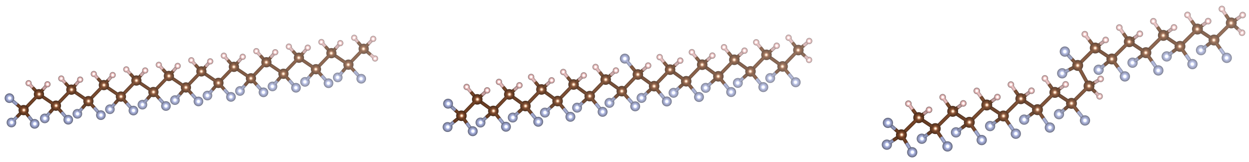

(a) 10−VDF **(b)** 9−VDF−1−TrFE **(c)** 10−VDF−1−GTG'

Figure 5.1: Equilibrium geometries of molecular models of PVDF and P(VDF−TrFE).

Substituting 1/10 of the CH_2CF_2 units of n−VDF with $CHCF_3$ (TrFE) units, one obtains n−VDF−m−TrFE, where $n + m$ is an integer multiple of 10. This is an *in vacuo* molecular model for the copolymer P(VDF−TrFE). Given this ideal construction of the model, we will refer to the unit TrFE as the *chemical defect*. The particular case with $n = 9$ is represented in Figure 5.1b.

Conformational disorder can also be incorporated imposing the presence of one gauche-trans-gauche' (GTG') dihedral angle in an n−VDF molecule every 10 repeat units. This is also the most simple way to take into account that the distribution of these *conformational defects* is random above the Curie temperature of PVDF. We refer to this model as n−VDF−l−GTG', with $n = 10l$, and illustrate the particular case for $n = 10$ in Figure 5.1c.

In all of these molecular models, we impose an all-*trans* conformation of the polymer backbone to better describe the β phase of PVDF, which is also the only crystalline phase of P(VDF−TrFE) [48, 84]. Terminal groups CH_3 and CF_3 are chosen coherently with the chemical structure of PVDF, in order to preserve the periodic alternation of CH_2 and CF_2 groups as much as possible. When multiple chemical and conformational defects are taken into account, they are disposed in a regular arrangement along the molecule, so as to make them equidistant from each other. On one side, this is done in view of the randomness with which the statistical distribution of these defects is described in the literature [85]. On the other hand, this approach allows us to consider independent defects, which simplifies the subsequent investigation of their effect on the vibrational properties of PVDF and P(VDF−TrFE).

2. A further step towards the modeling of macromolecular chains of PVDF and P(VDF−TrFE) is done passing from finite molecular to one-dimensional periodic models. In particular, Figure 5.2 represents VDF−1D and VDF−TrFE−1D, to which periodic boundary conditions (PBCs) are applied. These models ideally represent the limit behavior of n−VDF and n−VDF−m−TrFE for $n \to \infty$.

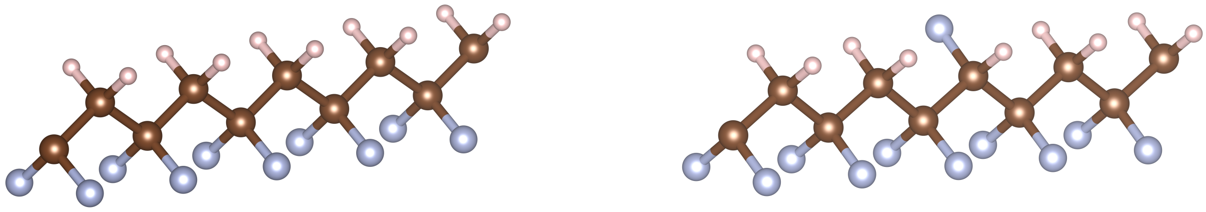

(a) VDF−1D **(b)** VDF−TrFE−1D

Figure 5.2: Equilibrium geometries of one-dimensional periodic models of PVDF and P(VDF−TrFE). In panel (a) a portion with five repeat units of VDF−1D is represented, while panel (b) shows the repeat unit of P(VDF−TrFE).

We notice that, to preserve a constant concentration of chemical defect, the structural unit of the chemically-defected one-dimensional periodic model must be relatively large. This requires to impose again the all-*trans* conformation to the polymer backbone, which instead directly results from periodicity in the other model.

3. To account for solid-state effects in PVDF, inter-chain interactions must be taken into account. This is first done considering clusters, ideally obtained stacking a finite number of VDF−1D models along the direction of their electric dipole moment. This results in 2−VDF−1D and 3−VDF−1D−**m** models, which are represented in Figure 5.3. In particular, 2−VDF−1D is used as the most simple approximation of the inter-chain interactions, while 3−VDF−1D−**m** approximates the interaction of a PVDF chain embedded in a large crystal with two first neighbors in the direction of their electric dipole moments. To increase the accuracy of 3−VDF−1D−**m**, arbitrary large masses are assigned to the external chains, for the reasons discussed at point 5. Then, the limit behavior of these models for $n \to \infty$ can be also taken into account, considering a two-dimensional periodic model with the same basis of Figure 5.2a, which is referred to as VDF−2D.

4. A second step towards the modeling of the solid crystalline phase of PVDF requires a three-dimensional periodic model. In this case we consider the model VDF−3D, which is obtained with the basis of Figure 5.2a for an orthorhombic crystal structure. This gives the model illustrated in Figure 5.4a. The chemical defect can be taken into account as done for one-dimensional models. Imposing the usual requirements for an all-*trans* conformation of the chains, the VDF−TrFE−3D model of Figure 5.4b is obtai-

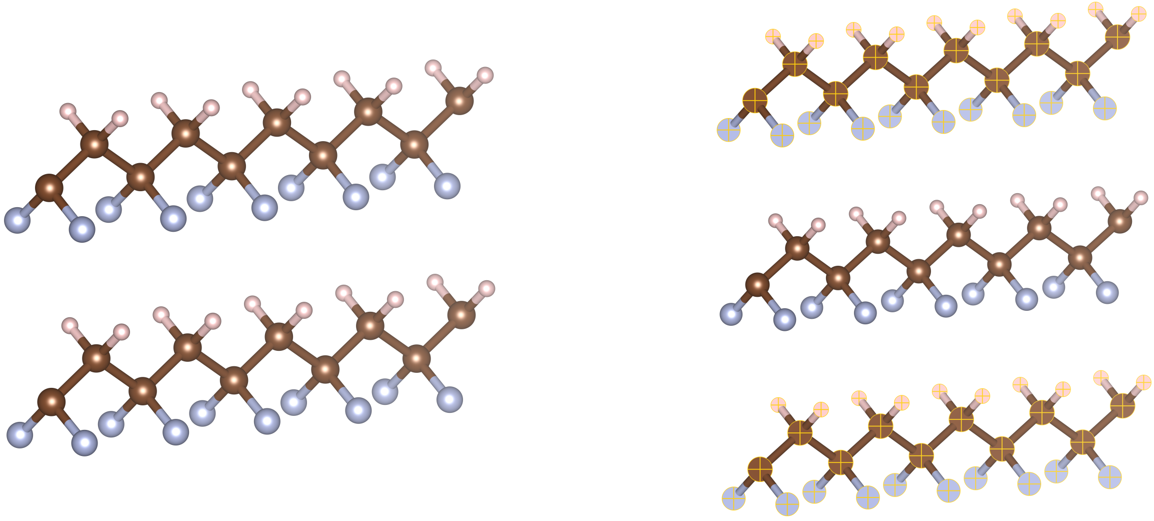

(a) 2−VDF−1D **(b)** 3−VDF−1D−**m**

Figure 5.3: Equilibrium geometries of cluster models of PVDF. In both panels, portions with five repeat units are shown. In panel (b), crossed atoms are assigned a mass $m = 1000\,\text{amu}$.

ned. In particular, we point out that this is a simple three-dimensional periodic model, with all the chemical defects at equivalent positions. This choice makes our approach simple, but also limited, because the statistical distribution of chemical defects is in this way completely neglected. In both cases, the structural optimization begins with experimental equilibrium values for PVDF available in the literature [86].

5. In some cases, it is convenient to assign an arbitrary large mass to particular atoms of a model in order to localize normal vibrational modes in regions of interest. In doing this, we follow an approach applied for the first time elsewhere [87]. When all the atoms of 9−VDF−1−TrFE except the CHF unit of the chemical defect are assigned a large mass, we refer to it as 9−VDF−1−TrFE−**m**. Also 3−VDF−1D−**m**, discussed above, has by definition large masses on the two external PVDF one-dimensional periodic chains. These models are represented in Figures 5.5 and 5.3b.

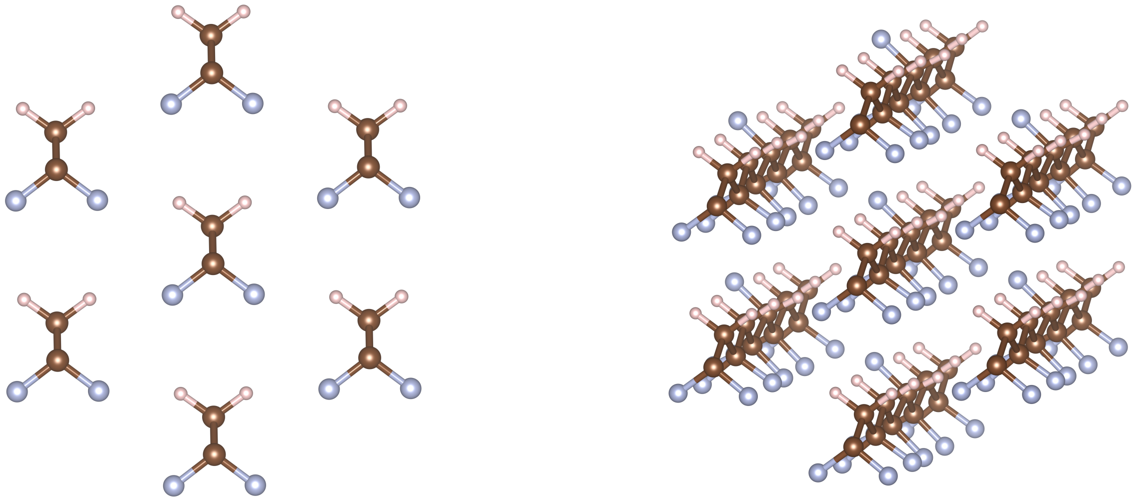
(a) VDF−3D (b) VDF−TrFE−3D

Figure 5.4: Equilibrium geometries of three-dimensional periodic models of PVDF and P(VDF−TrFE). In both panels, portions with seven repeat units are shown.

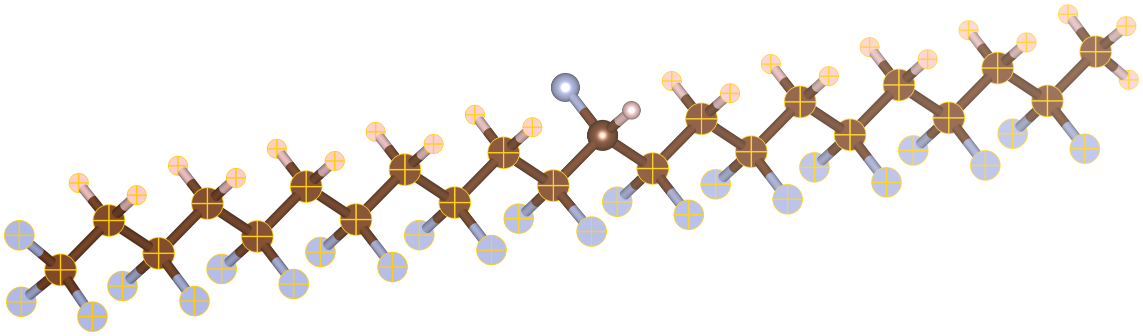

Figure 5.5: Equilibrium geometry of 9−VDF−1−TrFE−**m**. Crossed atoms are assigned a mass $m = 1000\,\text{amu}$.

5.2 Model performance

PVDF. In order to study the vibrational properties of PVDF and P(VDF−TrFE), we first need to consider that molecular models of different lengths are characterized in general by different performances. Longer oligomeric models are usually more descriptive of experiments, but they also require more computational effort in simulating their properties [88]. Therefore, the choice of a good molecular model is a compromise between reliability and simplicity. In Figure 5.6a, the IR spectra of several n−VDF models are represented. It is possible to see that, in passing from $n = 2$ to $n = 10$ repeat units in the model, spurious features at $\sim 1400\,\text{cm}^{-1}$ and $\sim 950\,\text{cm}^{-1}$ progressively disappear. This points out that those features are associated to vibrations localized on molecular terminal groups, which are not observed experimentally. This is confirmed by inspecting the vibrational normal modes of these molecular models. Figure 5.6b shows that extending the length to $n > 10$, only a little effect on the terminal bands is obtained.

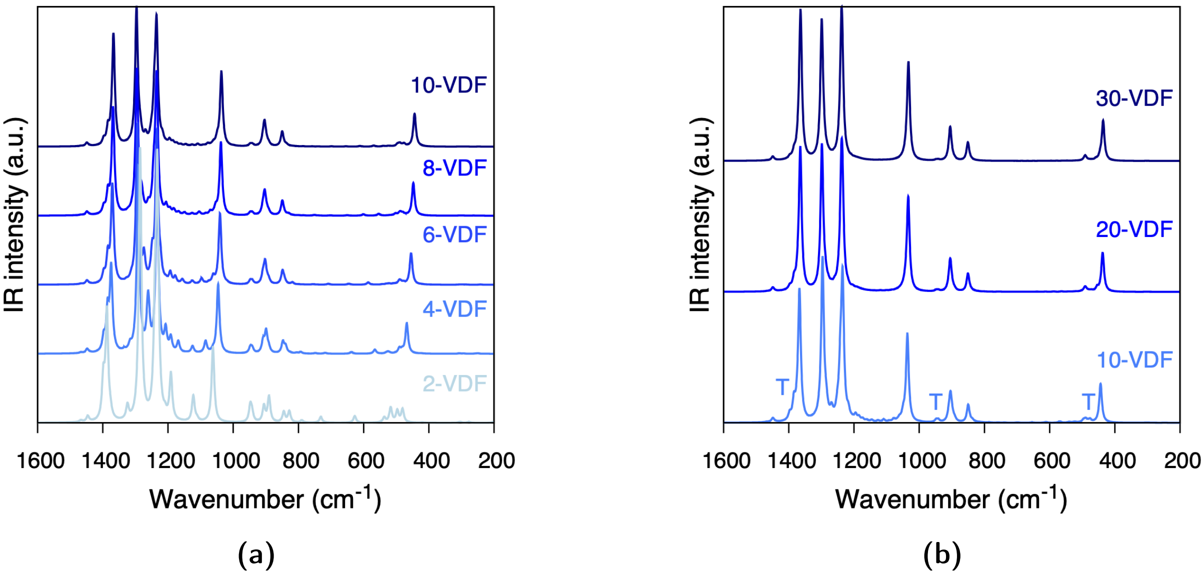

(a)

(b)

Figure 5.6: Study of the performance of oligomeric models of PVDF. IR spectra of $n-$VDF with $n = 2, 4, 6, 8, 10, 20, 30$. In both panels, IR intensities are normalized to n. In panel (b) terminal bands are indicated with T.

The simulated Raman spectra of Figure 5.7a show a similar situation for what concerns the terminal bands, which are present at $\sim 1500\,\mathrm{cm}^{-1}$ and cancel out when longer models are considered. Moreover, we notice that the region between $1000\,\mathrm{cm}^{-1}$ and $1200\,\mathrm{cm}^{-1}$ is more affected by the length of short models with respect to the same region of the IR spectra observed above. This fact suggest this region of the Raman spectrum to be sensitive of the disorder in the material. We expect this portion to become structured and with broad features when disorder is introduced in the material, for example by means of heating. The spectra of Figure 5.7b confirm that 10$-$VDF is a good choice to model the vibrational properties of PVDF in the oligomer approach, because longer models show no significant enhancements.

Chemical and conformational defects. The same procedure as above can be applied also to oligomeric models incorporating chemical and conformational defects. Figure 5.8 shows that the predictions of 9$-$VDF$-$1$-$TrFE and longer models are almost identical, both for IR and Raman spectroscopy. Although terminal modes at $\sim 1250\,\mathrm{cm}^{-1}$ and $1450\,\mathrm{cm}^{-1}$ are still present, we choose 9$-$VDF$-$1$-$TrFE by consistency: in this way, the effect of chemical defects can be studied at constant length of the chains. Moreover, Figure 5.8b confirms that in the region between $1000\,\mathrm{cm}^{-1}$ and $1200\,\mathrm{cm}^{-1}$ the Raman response is affected by the number of repeat units in the oligomer, for which the same observations as above are valid.

The goodness of 10$-$VDF and 9$-$VDF$-$1$-$TrFE as molecular models is corroborated by their

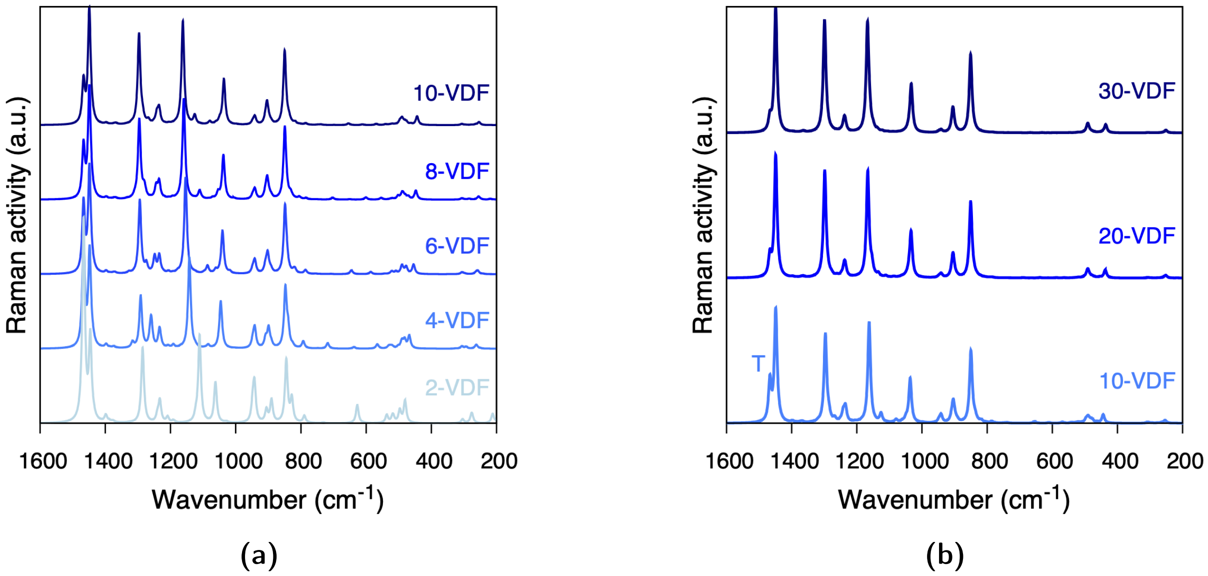

Figure 5.7: Study of the performance of oligomeric models of PVDF. Raman spectra of n−VDF with $n = 2, 4, 6, 8, 10, 20, 30$. In both panels, Raman activities are normalized to n. In panel (b) a terminal band is indicated with T.

comparison with one-dimensional models to which PBCs are applied. Taking into account that symmetry necessarily simplifies the spectra of VDF−1D and VDF−TrFE−1D [56], as expected Figure 5.9 shows that some differences in IR intensities and Raman activities exist between oligomeric and periodic models. Apart from this, however, the simulated spectra of molecular and periodic models are similar, especially for what concerns the wavenumber of the most intense features. Therefore, 10−VDF and 9−VDF−1−TrFE can be safely chosen as *in vacuo* models for PVDF and P(VDF−TrFE). It must be pointed out that this kind of choice makes us completely neglect the effect of inter-chain interactions on the IR and Raman responses. These solid-state effects will be taken into account by one-dimensional periodic clusters and two- and three-dimensional periodic models in section 5.5.

We postpone the discussion on the choice of the oligomeric model with conformational defects to section 5.4. There, it will be shown that 10−VDF−1−GTG' can be chosen for describing the effect of GTG' defects in a PVDF chain.

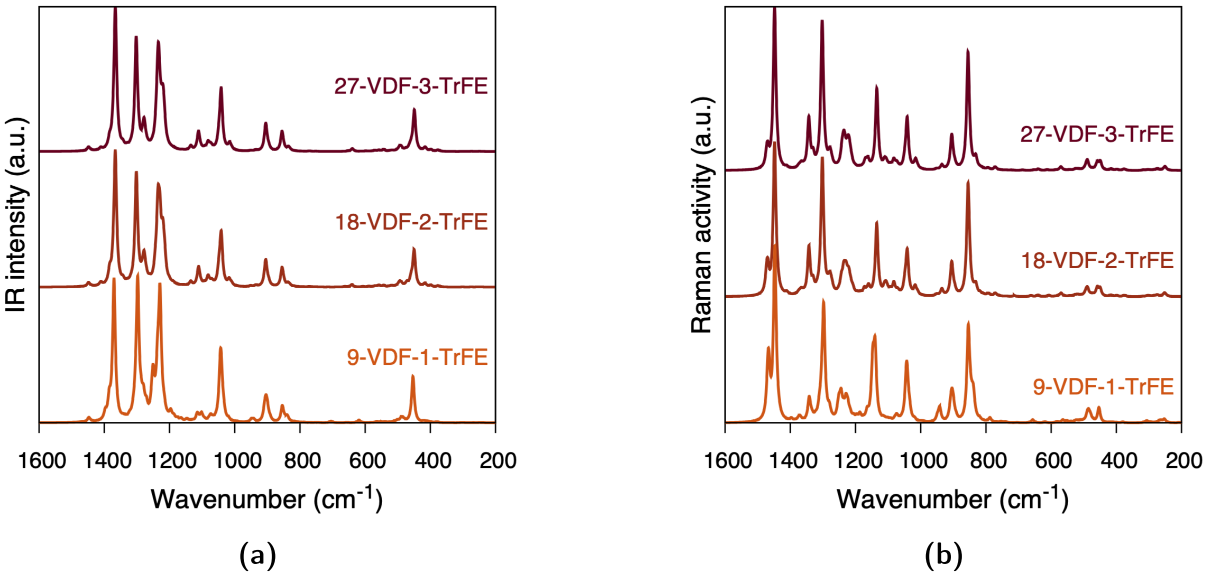

Figure 5.8: Study of the performance of oligomeric models of P(VDF−TrFE). IR (a) and Raman (b) spectra of n−VDF−m−TrFE, with $n = 9, 18, 27$. IR intensities and Raman activities are normalized to $(10/9)n$.

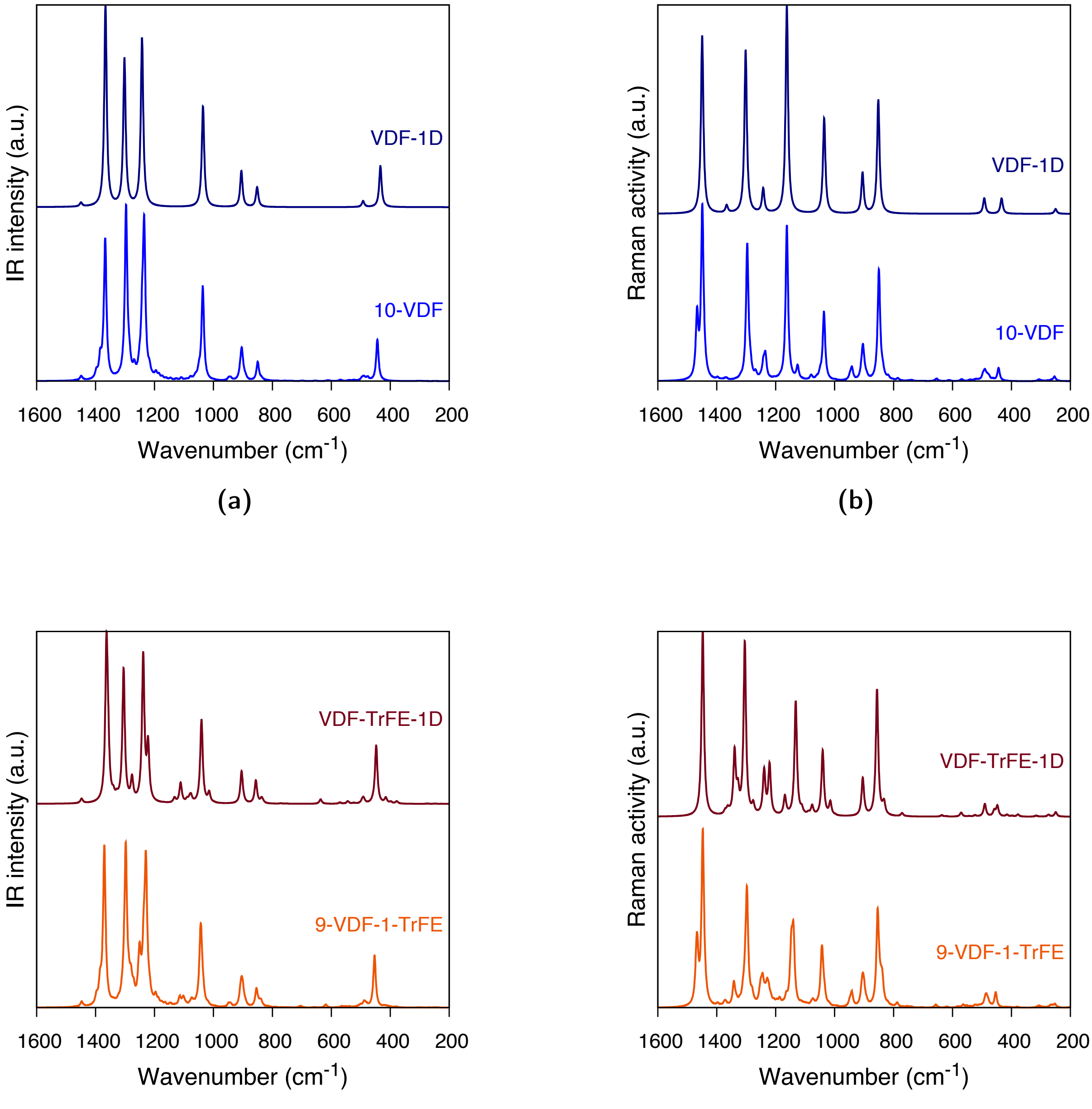

(a) **(b)**

(c) **(d)**

Figure 5.9: Comparison between IR and Raman spectra of molecular and one-dimensional periodic models of PVDF (a, b) and P(VDF−TrFE) (c, d). In all panels, IR intensities and Raman activities have been normalized on the number of CH_2CF_2 or $CHCF_3$ units either in the molecule or in the repeat unit.

5.3 Chemical defect

We now regard TrFE units as chemical defects of PVDF, and study their effect on the IR and Raman spectra of P(VDF−TrFE) models. In this way, IR and Raman chemical defect markers will be identified.

IR spectroscopy. The explanatory power of 10−VDF and 9−VDF−1−TrFE is readily tested by a comparison with experiments. In Figure 5.10a, simulated IR spectra are compared with the experimental spectrum of P(VDF−TrFE) films reproduced from Ref. [2]. As it can be observed, our model does not account correctly for the intensities in the wavenumber region between $1200\,\mathrm{cm}^{-1}$ and $1400\,\mathrm{cm}^{-1}$. On the contrary, theory and experiment are in good accordance for what concerns the wavenumber of the bands. This is especially true for the weak features at $1113\,\mathrm{cm}^{-1}$ and $1341\,\mathrm{cm}^{-1}$, which are displayed by both P(VDF−TrFE) and 9−VDF−1−TrFE, but not by 10−VDF. Inspecting the vibrational normal modes associated to those features, we conclude that they are associated respectively to the CF stretching and to the CH bending of the only chemical-defective unit of 9−VDF−1−TrFE, as represented in Figures 5.10b and 5.10c. This suggests to identify such bands as IR vibrational markers of TrFE units in PVDF.

A stronger assignment of the vibrational features at $1113\,\mathrm{cm}^{-1}$ and $1341\,\mathrm{cm}^{-1}$ as markers of the chemical defect is obtained considering 9−VDF−1−TrFE−**m**, in which the only IR intense vibrational normal modes are localized on the defective CHF unit (see Figure 5.5). As a consequence, all the IR features of 9−VDF−1−TrFE−**m** are markers of the chemical defect. As shown in Figure 5.11, the previous suggestion on the chemical defect markers is confirmed. The IR spectrum of 9−VDF−1−TrFE−**m** also shows two features at $\sim 875\,\mathrm{cm}^{-1}$ and $\sim 800\,\mathrm{cm}^{-1}$, which are visible in the spectrum of 9−VDF−1−TrFE of Figure 5.10a as well, but, due to their low IR intensity, are hardly observed during experiments. On the opposite, 9−VDF−1−TrFE shows two weak IR features at $\sim 700\,\mathrm{cm}^{-1}$ and $600\,\mathrm{cm}^{-1}$ that do not have a counterpart in 9−VDF−1−TrFE−**m**, and are assigned to vibrational collective modes of all the molecule. This means that the ideal insertion of TrFE units in PVDF modifies its IR response introducing new vibrational modes which not only are localized on the chemical defect, but can also involve the whole molecular chain.

The above observations keep their validity also when the discussion is extended to periodic one-dimensional models. For VDF−TrFE−1D, we also observe the presence of markers of the chemical defect corresponding to collective modes of the one-dimensional crystal, which are absent in VDF−1D. Such features may be traced back to phonons at $k \neq 0$ in VDF−1D,

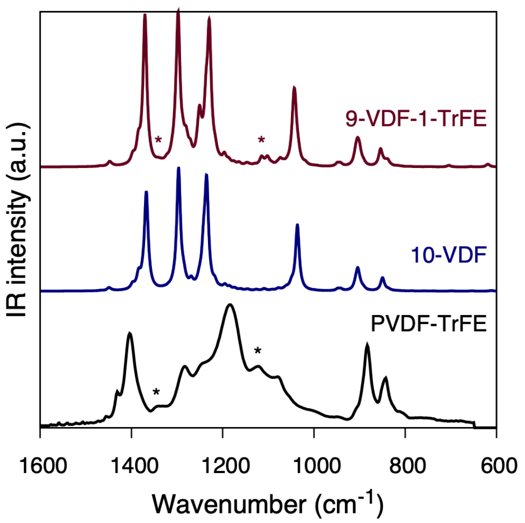

(a)

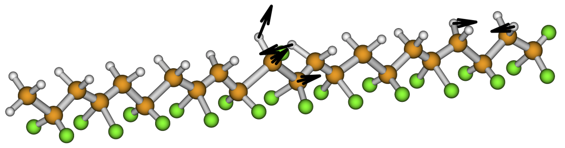

(b) 1113 cm^{-1}

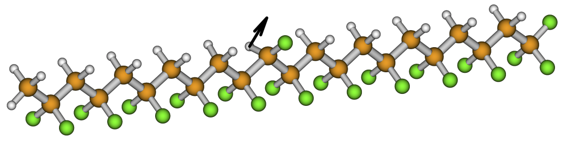

(c) 1341 cm^{-1}

Figure 5.10: IR vibrational markers of the chemical defect in molecular models. (a) IR spectra of P(VDF−TrFE), 10−VDF and 9−VDF−1−TrFE, where asterisks indicate experimental and computed vibrational markers of the TrFE unit. The maximum IR intensities are normalized to 1 in the represented interval. The experimental IR spectrum is reproduced from Ref. [2]. (b, c) Vibrational normal modes of 9−VDF−1−TrFE corresponding to the computed vibrational markers of the TrFE unit.

and thus not obtained in our simulated spectra. In this case the cause for this would be the different size of the bases of the two one-dimensional crystals.

Three-dimensional periodic models corroborate the above findings, as shown in Figure 5.12b. Indeed, VDF−TrFE−3D shows vibrational markers for the TrFE unit at 1102 cm^{-1} and 1337 cm^{-1}, with the same correspondence to localized vibrational normal modes described above. This same plot also shows that the presence of a chemical defect causes the dispersion of the IR spectrum of VDF−3D to wavenumbers which are more in accordance with the experiment. The results of the above investigation are resumed in Table 5.1.

Raman spectroscopy. The same procedure as above can be applied to investigate for the presence of Raman vibrational markers of the TrFE unit. We first consider the simulated Raman spectra of 10−VDF and 9−VDF−1−TrFE, and compare them with the experimental Raman spectrum in Figure 5.13. It is immediately noticed that a peak is present at 1341 cm^{-1} only in the spectrum of 9−VDF−1−TrFE, corresponding to a feature in P(VDF−TrFE) at $\sim$ 1345 cm^{-1}. Inspecting the computed vibrational normal modes, this marker is traced back to a CH bending localized in the TrFE unit. Therefore, we regard this feature as a Raman vibrational marker of the presence of a TrFE chemical defect in P(VDF−TrFE). Another, less active, vibrational feature associated to vibrational modes localized in the chemical defect

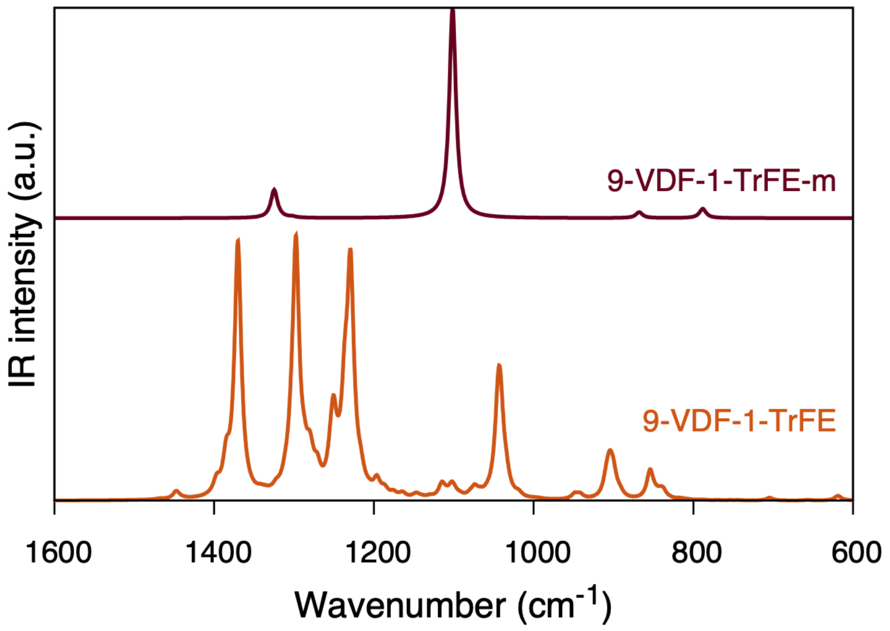

Figure 5.11: IR vibrational markers of the chemical defect in molecular models. IR spectra of 9–VDF–1–TrFE and 9–VDF–1–TrFE–**m**. The maximum IR intensities are normalized to 1.

can be found at $\sim 450\,\mathrm{cm}^{-1}$. It is associated in our computation to a CF_2 scissoring mode localized in TrFE. However, we do not consider this feature as a vibrational marker, due to its low Raman activity.

The implications of the discussion above are corroborated by comparing the simulated Raman spectra of 9–VDF–1–TrFE and 9–VDF–1–TrFE–**m** as in Figure 5.14a. In the spectrum of 9–VDF–1–TrFE–**m**, the previously found Raman vibrational marker appears as the most intense feature at $1354\,\mathrm{cm}^{-1}$. Other relatively intense peaks are present as well, but they do not behave as vibrational markers in the Raman spectra, due to their low Raman activity. However, the occurrence of these Raman transitions is still meaningful considering the discussion of section 5.2, where the particular dependence of the Raman spectrum on the disorder in the material was mentioned. This is evident if we compare the normalized IR and Raman intensities of 9–VDF–1–TrFE–**m** in the same wavenumber interval as in Figure 5.14b. It is immediately recognized that the presence of the TrFE unit has different effects in the IR and Raman responses of models where vibrations are localized by assigning arbitrary large masses to selected atoms: while the IR spectrum is characterized by one intense localized vibration in the chemical unit at $1324\,\mathrm{cm}^{-1}$, together with a less intense one at $1101\,\mathrm{cm}^{-1}$, the Raman spectrum shows several peaks of comparable activity. We observe therefore that chemical defects have a general perturbative effect on the Raman response of P(VDF–TrFE), introducing bands relative to collective motions which involve the chemical defect as well. It

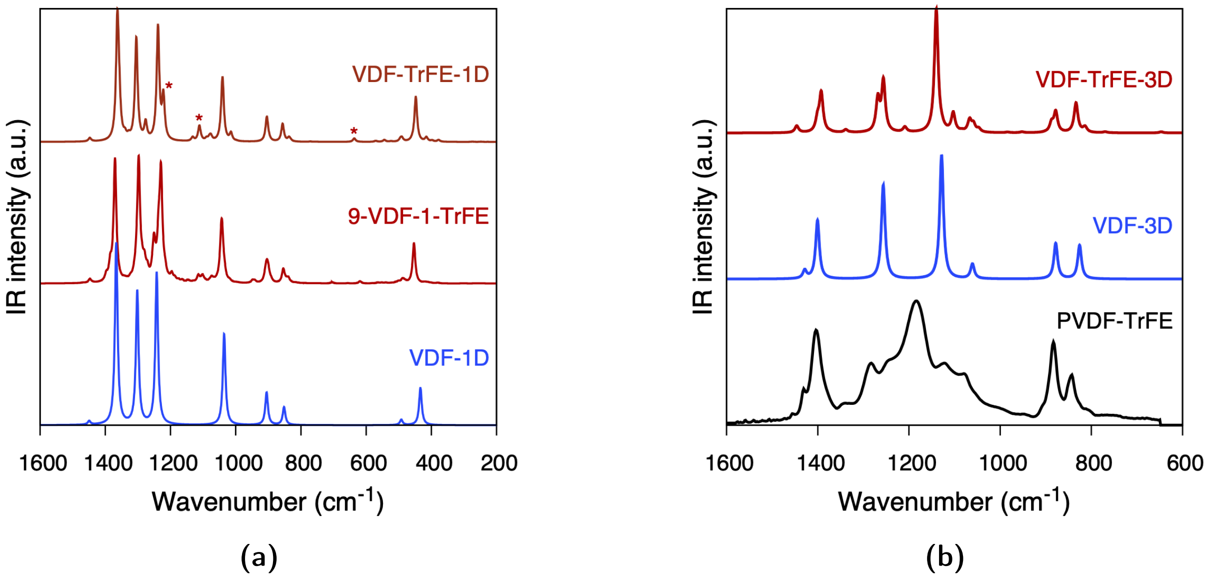

Figure 5.12: IR vibrational markers of the chemical defect in periodic models. (a) IR spectra of 10−VDF, 9−VDF−1−TrFE and VDF−TrFE−1D. Asterisks indicate the computed vibrational markers of the chemical defect. IR intensities are normalized on the number of CH_2CF_2 or $CHCF_3$ units either in the molecule or in the repeat unit. (b) IR spectra of P(VDF−TrFE), VDF−3D and VDF−TrFE−3D. The maximum IR intensities are normalized to 1.

is also to be noted, however, that in considering Raman spectra without the effect of large atomic masses, clearly localized Raman markers for the chemical defect are absent, due to the coupling of the vibrational normal modes of the defect with the chain. In section 5.4, we will see that a similar effect is produced by the introduction of conformational defects by means of heating (Figure 5.17b).

The simulated Raman spectra of one- and three-dimensional periodic models containing the chemical defect are reported in Figure 5.15, in comparison with the analogous for periodic models of PVDF. Figure 5.15a shows the substantial accordance between the predictions of 9−VDF−1−TrFE and VDF−TrFE−1D for what concerns the wavenumber of the vibrational marker of TrFE, which is found at $1338\,cm^{-1}$ for VDF−TrFE−1D. A slight shift towards higher wavenumbers is instead observed for the weak feature at $\sim 450\,cm^{-1}$. The same accordance exists for VDF−TrFE−3D, that correctly predicts the presence of a vibrational marker of the TrFE unit at $1338\,cm^{-1}$.

We thus infer that the presence of a TrFE unit in P(VDF−TrFE) determines a Raman feature at $1341\,cm^{-1}$, which we characterize as a vibrational marker of the chemical defect. In Table 5.2 we report the results of the discussion above.

Model	Wavenumber (cm^{-1})	IR intensity (km/mol)	Assignment
9−VDF−1−TrFE	1113	44	CF stretching
9−VDF−1−TrFE	1341	8	CH bending
9−VDF−1−TrFE	1366	6	CH bending
9−VDF−1−TrFE−**m**	1101	57	CF stretching
9−VDF−1−TrFE−**m**	1324	7	CH bending
VDF−TrFE−1D	1111	51	CF stretching
VDF−TrFE−1D	1338	14	CH bending
VDF−TrFE−3D	1102	187	CF stretching
VDF−TrFE−3D	1337	27	CH bending

Table 5.1: IR vibrational markers of the unit TrFE in different molecular and periodic models. In the last column, the localization of the vibrational normal mode in the chemical defect is understood.

Model	Wavenumber (cm^{-1})	Raman activity ($\mathring{A}^2/amu^{1/2}$)	Assignment
9−VDF−1−TrFE	1341	9	CH bending
9−VDF−1−TrFE−**m**	1354	6	CH bending
VDF−TrFE−1D	1338	13	CH bending
VDF−TrFE−3D	1338	20	CH bending

Table 5.2: Raman vibrational markers of the chemical-defective unit TrFE in different molecular and periodic models. In the last column, the localization of the vibrational normal mode in the chemical defect is understood.

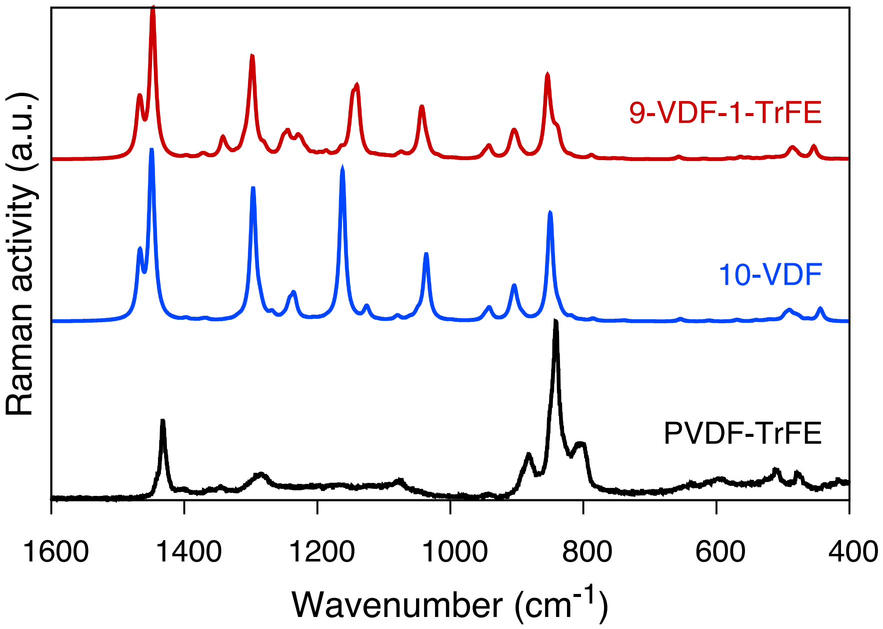

Figure 5.13: Raman vibrational markers of the chemical defect in molecular models. Raman spectra of P(VDF—TrFE), 10—VDF and 9—VDF—1—TrFE. The maximum Raman activities are normalized to 1 in the represented interval. The experimental Raman spectrum is reproduced from Ref. [2].

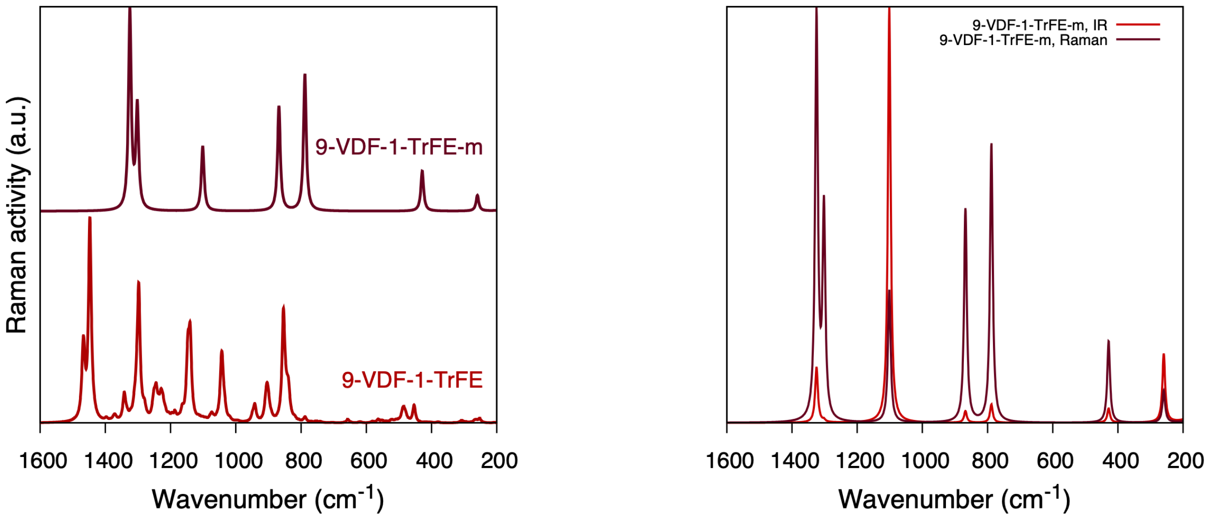

(a) (b)

Figure 5.14: Raman vibrational markers of the chemical defect in molecular models. (a) Raman spectra of 9—VDF—1—TrFE and 9—VDF—1—TrFE—**m**, with their maxima normalized to 1 in the represented interval. (b) IR and Raman spectra of 9—VDF—1—TrFE—**m** with their maxima normalized to 1 in the represented interval.

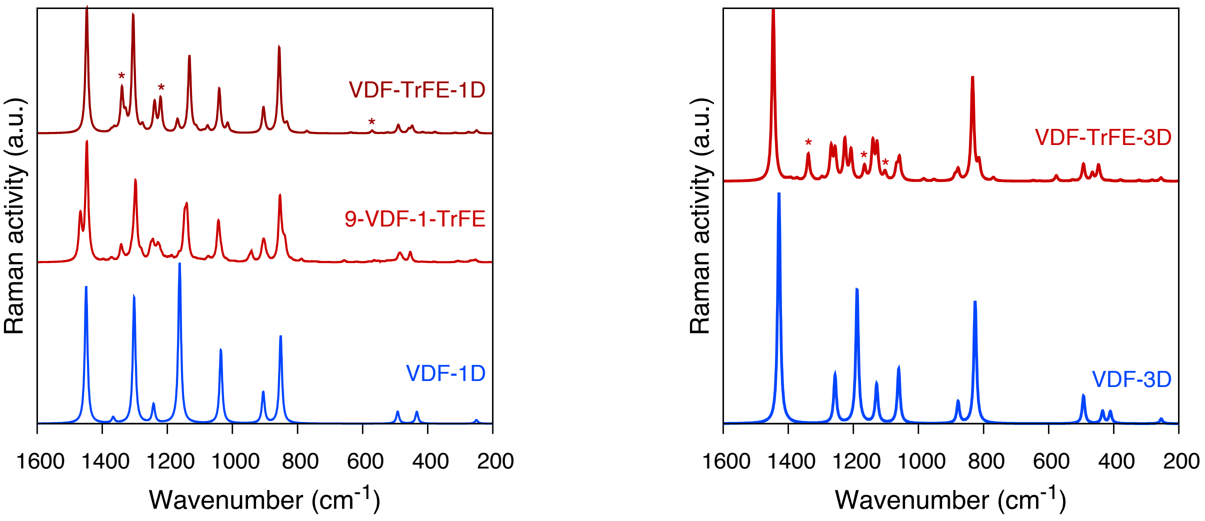

(a) **(b)**

Figure 5.15: Raman vibrational markers of the chemical defect in periodic models. (a) Raman spectra of VDF−1D, 9−VDF−1−TrFE and VDF−TrFE−1D. (b) Raman spectra of VDF−3D and VDF−TrFE−3D. In both panels, asterisks indicate the computed vibrational markers of the chemical defect, and Raman activities are normalized on the number of CH_2CF_2 or $CHCF_3$ either in the molecule or in the repeat unit.

5.4 Conformational defect

In the previous section, we have discussed the role of the TrFE unit on the IR and Raman spectra of P(VDF−TrFE). Another type of defect which can be considered is the conformational disorder of a single chain, which is produced for example providing heat to the material: as the energy of the polymeric chains increases, new conformations become energetically available, with an increase in the disorder. As pointed out in section 5.1, a most simple way of incorporating such defect in our model is considering GTG' torsions, also called *kinks*.

IR spectroscopy. Figure 5.16a compares the IR spectra of 10−VDF and 10−VDF−GTG'. Considering the effect of temperature increase in a real sample of P(VDF−TrFE) represented in Figure 5.16b, the following interesting points are noted. First, the presence of conformational disorder largely influences the region near $1250\,\mathrm{cm}^{-1}$. In particular, we notice that the IR intensity between the two peaks around $1300\,\mathrm{cm}^{-1}$ and $1225\,\mathrm{cm}^{-1}$ increases when the kink defect is present, which has a splitting action on those peaks. This suggests that the presence of the GTG' torsion activates vibrational modes which are localized in that region. The experimental counterpart for this fact is found in the growth of a shoulder at $\sim 1250\,\mathrm{cm}^{-1}$ in the IR spectrum of P(VDF−TrFE) as temperature is increased. Second, the relatively intense simulated feature at $900\,\mathrm{cm}^{-1}$ increases its IR intensity in the presence of the conformational defect. This, again, is in accordance with the effect of heat on P(VDF−TrFE).

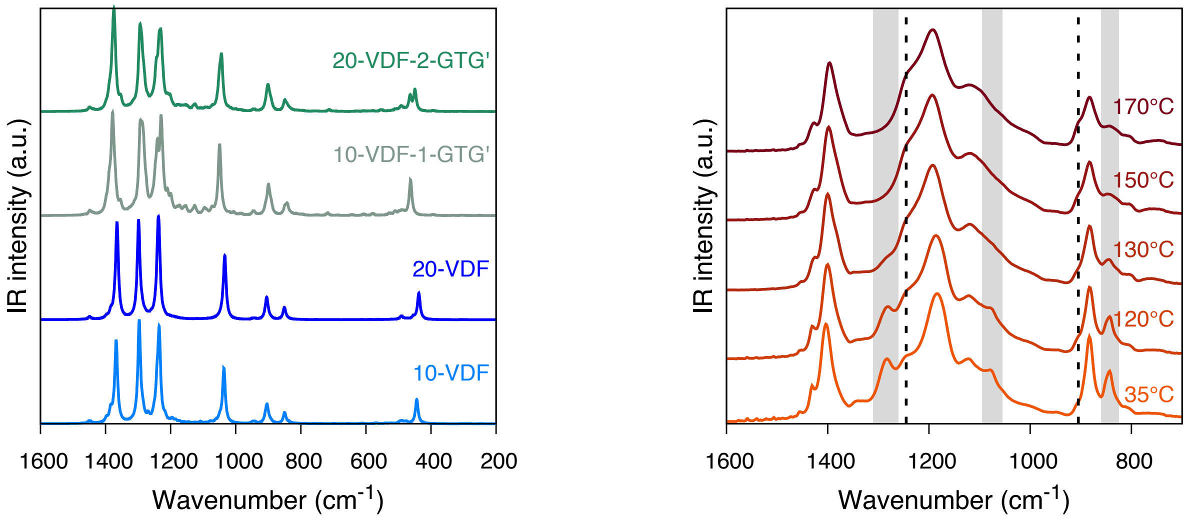

(a) (b)

Figure 5.16: (a) IR vibrational marker of the conformational defect in molecular models. IR spectra of 10−VDF, 20−VDF, 10−VDF−1−GTG' and 20−VDF−2−GTG'. IR intensities are normalized on the number of CH_2CF_2 repeat units. (b) IR spectrum of P(VDF−TrFE) films, reproduced from Ref. [2]. IR intensities are normalized to 1 in the represented interval.

Another interesting feature of 10−VDF−GTG' is the low-wavenumber component of the band at 850 cm^{-1}. Inspecting the vibrational normal modes associated to such feature, two modes of comparable intensities are found, each of which is the collective vibration of only one of two portions of the chain identified by the kink defect, as in Table 5.3. Thus a single conformational defect introduces two vibrational modes at similar frequency and IR intensity, each localized in a different portion of the chain. Extending this line of reasoning, the observed broadening of the experimental band at $\sim$ 850 cm^{-1} with heating can be rationalized: at high temperature, several vibrational modes are introduced which span a small interval of wavenumbers, and thus produce a broad feature as observed experimentally.

Model	Wavenumber (cm^{-1})	IR intensity (km/mol)	Assignment
10−VDF−GTG'	841	58	Collective CF stretching
10−VDF−GTG'	848	44	Collective CF stretching

Table 5.3: Vibrational normal modes corresponding to the low-wavenumber component of the band at 850 cm^{-1} of the IR spectrum of 10−VDF−1−GTG', represented in Figure 5.16a.

Raman spectroscopy. The effect of conformational disorder on the Raman response of PVDF is illustrated in Figure 5.17, where we report the simulated Raman spectra of 20−VDF−2−GTG' and 10−VDF on panel (a) and the experimental Raman spectrum of P(VDF−TrFE) at different temperatures in panel (b). As for the IR response discussed above, also the Raman spectrum is affected by conformational disorder with the appearance of several new features near 1250 cm^{-1}. In Figure 5.17a, the presence of a weak feature for 20−VDF−2−GTG' at 781 cm^{-1} is also interesting: it is associated to CCC bending modes partially localized on the GTG' defect, as described in Table 5.4. Therefore, this may be regarded as a spectroscopic marker for conformational disorder. This is consistent with the experiment, as seen in Figure 5.17b, where the increase in temperature causes the intensification of the band near 780 cm^{-1}. In the experimental Raman spectra, also the band at 600 cm^{-1} is affected by temperature. Coherently, 20−VDF−2−GTG' possesses, corresponding to that frequency, vibrational normal modes which are partially localized on the conformational defect, as listed in Table 5.4.

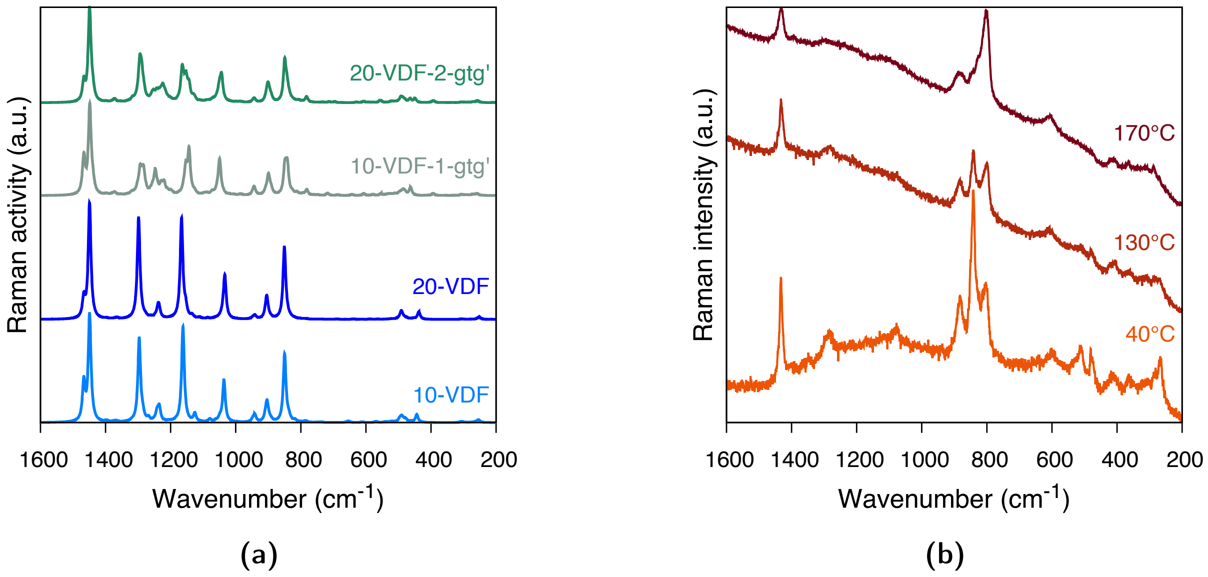

Figure 5.17: Raman vibrational marker of the conformational defect in molecular models. (a) Raman spectra of 10−VDF, 20−VDF, 10−VDF−1−GTG' and 20−VDF−2−GTG'. Raman activities are normalized on the number CH_2CF_2 repeat units. (b) Raman of P(VDF−TrFE) fibers, reproduced from Ref. [2]. Raman intensities are normalized to 1.

Model	Wavenumber (cm^{-1})	Raman activity ($Å^2/amu^{1/2}$)	Assignment
20−VDF−2−GTG'	781	3	CCC bending
20−VDF−2−GTG'	782	5	CCC bending
20−VDF−2−GTG'	606	2	CCC bending
20−VDF−2−GTG'	628	1	CCC bending

Table 5.4: Raman vibrational markers of the chemical-defective unit TrFE in different molecular and periodic models. In the last column, the localization of the vibrational normal mode in the chemical defect is understood.

5.5 Solid-state effects in PVDF

In sections 5.2 and 5.3 we have seen that molecular and one-dimensional periodic models are completely coherent. In this section, we investigate the effect of the solid state on the IR and Raman response of PVDF by means of a comparison between one- and higher-dimensional periodic models.

Comparison between one- and three-dimensional crystals. In Figure 5.18, the IR and Raman spectra of VDF−1D and VDF−3D are compared. In both cases, three effects on the vibrational features are obtained when passing from an *in vacuo* single-chain to a three-dimensional crystal model, namely the wavenumber shift, and the change in absolute and relative intensities or activities. By inspecting the vibrational normal modes associated to each feature, we are able to obtain a correspondence scheme between the features of

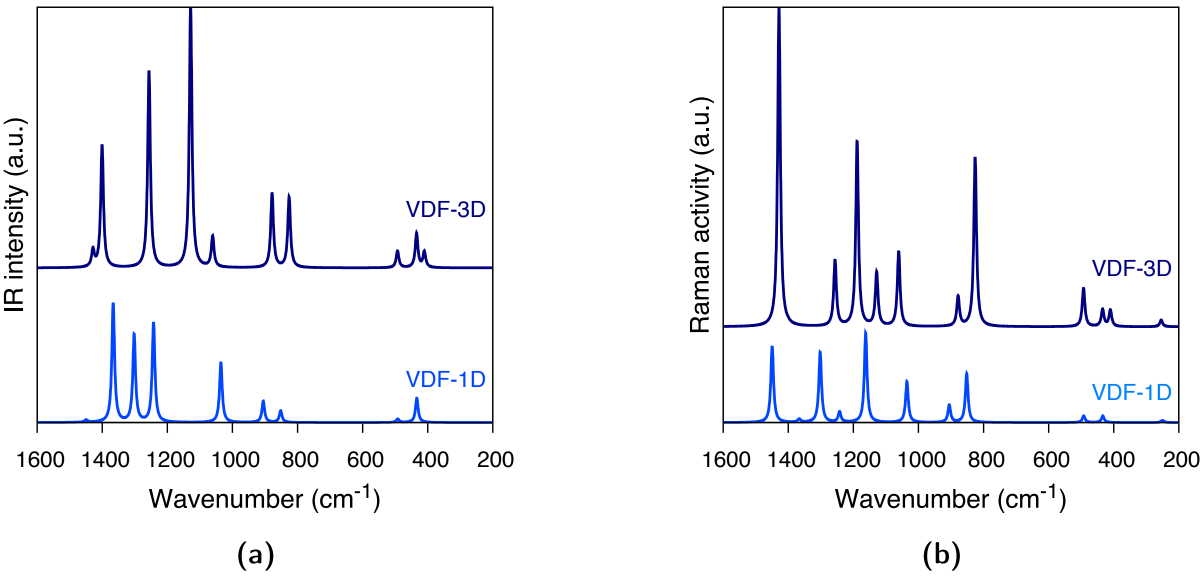

Figure 5.18: Solid-state effects on the IR and Raman responses of PVDF. (a) IR spectra of VDF−1D and VDF−3D. (b) Raman spectra of VDF−1D and VDF−3D.

VDF−1D and VDF−3D, as reported in Table 5.5. We thus observe that inter-chain electrostatic interactions have a non-negligible effect on the positions of both IR and Raman features of PVDF: in both spectra, there exists at least one band which undergoes a wavenumber shift $> 100\,\mathrm{cm}^{-1}$ from the *in vacuo* to the solid state. Electrostatic interactions affect the intensities of the features as well. Table 5.5 shows that the general trend is an increase in both IR intensities and Raman activities in passing to the solid state. However, no simple rule is found to account for the extent of either the wavenumber shift or peak intensification of different features. Nevertheless, these observations already show that different vibrational features are affected in different ways by inter-chain electrostatic interactions. Finally, we note that both the IR and Raman bands of VDF−3D vary in their intensity more than VDF−1D in the region we are interested in. A comparison with Figures 5.10a and 5.13 shows that this is characteristic of the experimental spectra. All of this suggests that a complete understanding of the IR and Raman vibrational properties of PVDF cannot neglect the interactions between chains. However, it is also to be reminded that some features, such as the vibrational markers studied in section 5.3, can still be grasped with an *in vacuo* approach.

Two-dimensional periodic models. The comparison above misses the possibility to discern between the range at which inter-chain interactions affect both the wavenumber and intensity of IR and Raman peaks. This aspect can be investigated more in detail considering two-dimensional models. In particular, Figure 5.19 adds to the previous comparison 2−VDF−1D, 3−VDF−1D−**m** and VDF−2D. It is useful to recall that these ideally represent the stacking of respectively two, three and an infinite number of VDF−1D models, and that in every case the electric dipole moments are aligned. In general, a trend compatible

Wavenumber (cm^{-1})	IR	Raman	Assignment
VDF−3D			
410	16	1	CH_2 rocking
434	35	1	CF_2 wagging
492	17	4	CF_2 scissoring
825	72	18	CF sym. stretching
878	76	3	CF asym. stretching + CH_2 rocking
1060	31	8	CH_2 wagging
1128	266	5	CH_2 rocking + CF asym. stretching
1188	0	20	CH_2 twisting
1257	201	7	CC bending
1400	125	0	CH_2 wagging
1428	17	35	CH_2 scissoring
VDF−1D			
433	24	0	CF_2 wagging
850	11	5	CF sym. stretching
904	21	1	CF asym. stretching + CH_2 rocking
1034	61	4	CH_2 wagging
1161	0	9	CH_2 twisting
1242	102	1	CH_2 rocking + CF asym. stretching
1301	89	7	CC bending
1366	122	0	CH_2 wagging
1449	2	8	CH_2 wagging

Table 5.5: Assignment of the IR and Raman spectra of VDF−1D and VDF−3D shown in Figure 5.18. IR intensities are reported in km/mol, Raman activities in $Å^2/amu^{1/2}$.

with long-range interactions is obtained for every vibrational feature of both spectra: indeed, non-negligible wavenumber shifts and intensity variations are observed in moving from 3−VDF−1D−**m** to VDF−2D. The same holds for the transition from VDF−2D to VDF−3D. From these observations, we infer that long-range electrostatic interactions between aligned electric dipoles give important contributions to the vibrational behavior of PVDF, but the whole crystal must be considered to account for it completely. In Figure 5.19, three features in particular are characterized by a large variation of intensity, positioned in VDF−1D at $\sim 1250\,cm^{-1}$, $925\,cm^{-1}$ and $870\,cm^{-1}$. The behavior of the former will be taken into account in the following discussion. These last two are studied in Table 5.6, both from the point of view of their wavenumber and peak intensity. We notice that the general trend found when considering only VDF−1D and VDF−3D is here only partially reproduced: indeed, while the wavenumber shift is monotonous and both the considered features decrease in wavenumber in moving towards VDF−3D, the same is not true for the IR intensities and Raman activities in general. This motivates us to consider a more detailed situation with different expansions of the three-dimensional model.

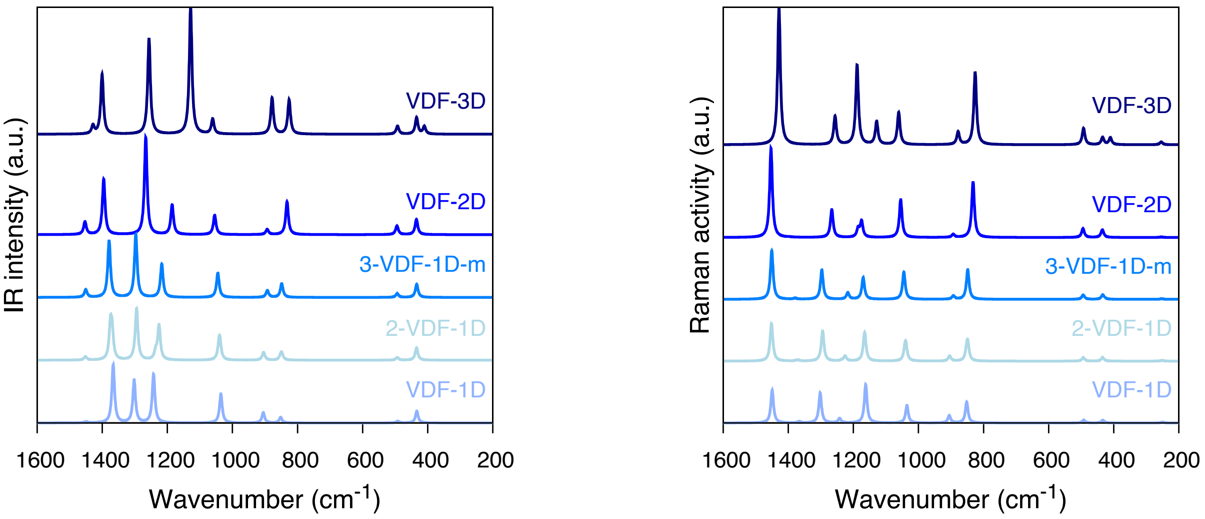

(a) **(b)**

Figure 5.19: Solid-state effects on the IR and Raman responses of PVDF. (a) IR spectra of VDF−1D, 2−VDF−1D, 3−VDF−1D−**m**, VDF−2D and VDF−3D. (b) Raman spectra of VDF−1D, 2−VDF−1D, 3−VDF−1D−**m**, VDF−2D and VDF−3D.

Isotropic expansion of VDF−3D. Progressively increasing two cell parameters of VDF−3D in a uniform way, the transition from a three- to an effective one-dimensional model can be reproduced. Figures 5.20a and 5.20b show the dispersion of the IR and Raman spectra of VDF−3D during this expansion. The range at which vibrational features are influenced is evident. In general, all the features are characterized by an important wavenumber shift as soon as the equilibrium cell parameters of PVDF are increased. However, we see that the feature at $\sim 1250\,\mathrm{cm}^{-1}$ in the IR spectrum of VDF−1D, which corresponds to the peak at $\sim 1100\,\mathrm{cm}^{-1}$ in VDF−3D, is characterized by the largest wavenumber shift in the first steps of the expansion. A similar behavior is shared by other IR and Raman features. On the opposite, other features are characterized by a minimum wavenumber dispersion, for example the weak band at $\sim 500\,\mathrm{cm}^{-1}$ in VDF−3D. Based on this, we infer that the whole three-dimensional neighborhood of chains has different effects on the vibrational properties of PVDF based on the involved vibrational normal mode. A second important observation is that the degree of the expansion at which a plateau in the wavenumber is reached depends on the particular feature. We can infer for instance that the CH_2 wagging corresponding to the IR band at $1060\,\mathrm{cm}^{-1}$ in VDF−3D is highly influenced at short-range, while the CH_2 rocking with CF asymmetric stretching of the IR peak at $1128\,\mathrm{cm}^{-1}$ is affected by long-range interactions.

Anisotropic expansion of VDF−3D. Similarly to what discussed above, we can also take into account the expansion of VDF−3D at constant distance between the PVDF chains with aligned electric dipoles, so that the transition from VDF−3D to VDF−2D of Figure 5.21 is obtained. This comparison can be used in combination with the one above to separate

Model	Wavenumber (cm^{-1})	IR intensity (km/mol)	Raman activity ($\mathring{\mathrm{A}}^2/\mathrm{amu}^{1/2}$)
VDF−1D	870	12	5
VDF−1D	925	22	1
2−VDF−1D	867, 871	19	6
2−VDF−1D	924	17	1
3−VDF−1D−**m**	867	29	7
3−VDF−1D−**m**	912	15	1
VDF−2D	850	69	14
VDF−2D	913	11	1
VDF−3D	844	72	19
VDF−3D	897	76	3

Table 5.6: Solid-state effects on two vibrational features in the region between 850 cm^{-1} and 1000 cm^{-1} in periodic models of PVDF.

between the influence of neighboring chains with parallel electric dipoles and the effect of chains with aligned dipoles. In particular, we see that the IR peak at 1128 cm^{-1} of VDF−3D is highly dependent on short-range interactions between chains with parallel electric dipole.

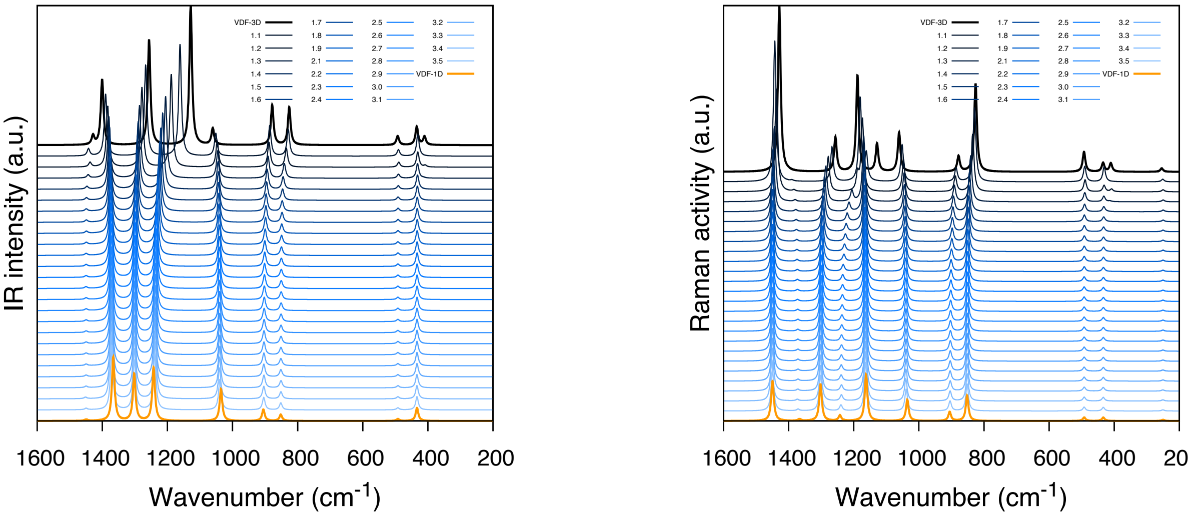

(a)

(b)

Figure 5.20: IR and Raman spectra of VDF−3D at different extents of isotropic expansion. In both spectra, the key reports the values of $a/a_0 = b/b_0$, where the cell parameters a and b correspond to directions orthogonal to the PVDF chain axis and 0 indicates their equilibrium values.

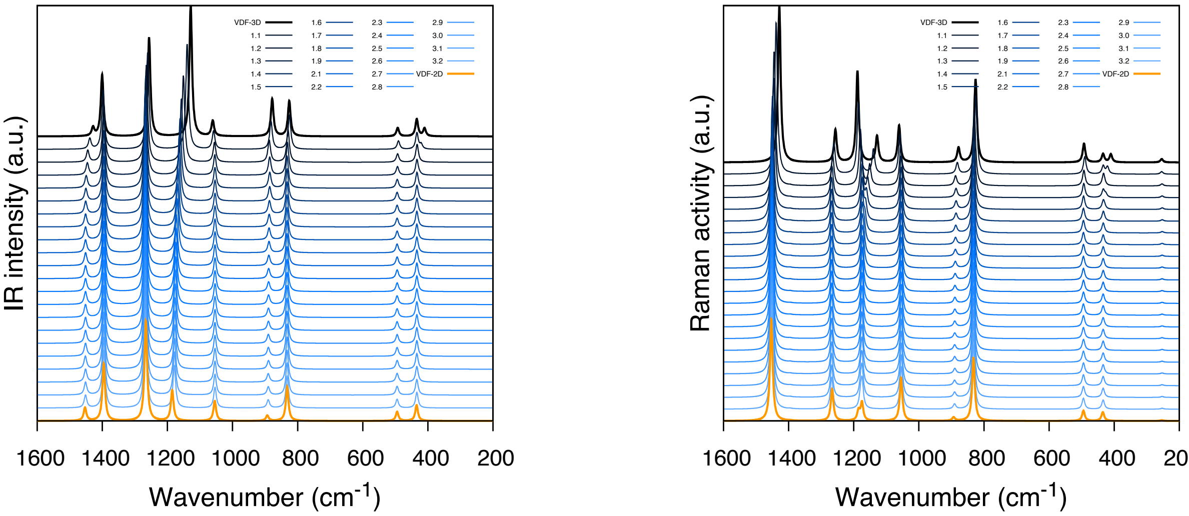

(a)

(b)

Figure 5.21: IR and Raman spectra of VDF−3D at different extents of anisotropic expansion. In both spectra, the key reports the values of a/a_0, where the cell parameter a corresponds to a direction orthogonal to the PVDF chain axis and 0 indicates its equilibrium value.

5.6 Chapter conclusions

In this Chapter, density functional methods have been applied to investigate the vibrational properties of PVDF and P(VDF−TrFE). In conclusion, we have found that:

1. Molecular models do not account completely for IR and Raman intensities of PVDF and P(VDF−TrFE), but correctly predict the wavenumbers of the most prominent features in the region between $200\,\mathrm{cm}^{-1}$ and $1600\,\mathrm{cm}^{-1}$. This is because 10−VDF has all the useful features of a one-dimensional crystal.
2. It is possible to support theoretically the existence of spectroscopic markers of the TrFE unit in P(VDF−TrFE) by means of a molecular model. In particular, two IR and one Raman vibrational markers near $1113\,\mathrm{cm}^{-1}$ and $1340\,\mathrm{cm}^{-1}$ have been obtained computationally and proved to be associated to localized CF stretching and CH bending vibrational modes.
3. It is possible to rationalize the trend of the IR and Raman spectra of P(VDF−TrFE) with heat based on molecular models with a GTG' torsional angles.
4. Solid-state effects in PVDF are accounted for by three-dimensional models. In particular, it is found that long-range electrostatic interactions between PVDF chains result in non-negligible wavenumber shifts and peak intensification. Moreover, the extent and the effectiveness of the intermolecular interactions is heavily dependent on individual normal modes.

Chapter 6

Conclusion

Again! again! again!

— Thomas Campbell

The introduction of density functional theory (DFT) in the field of quantum chemistry has been termed a revolution [89]. Focusing on the particular field of vibrational spectroscopy, the above Chapters have shown the practical outcomes of DFT, highlighting the wide range of applicability of this theory for what concerns the characterization of advanced materials and the understanding of their behavior.

In this Thesis, DFT has been used as an analytical tool for the prediction and corroboration of experimental results obtained by vibrational spectroscopy. In particular, three problems have been posed relative to different advanced materials, and the predictive power of DFT supported experimental evidence.

In particular, in Chapter 3 we investigated the polaron localization resulting from the n-doping of the conductive polymer N2200 [90] and supported previous experimental evidence [1]; in Chapter 4 we supported the successful synthesis of functionalized graphene nanoribbons [53] by assigning their IR and Raman spectra; in Chapter 5 we showed that the TrFE chemical unit of P(VDF−TrFE) perturbs the IR and Raman spectra of PVDF; we identified the vibrational markers of TrFE, and deepened the reasons for the observed thermal behavior of the vibrational spectra of P(VDF−TrFE) [2]. The results reported in these three Chapters show how different concepts in materials science could be corroborated applying DFT to simple molecular or periodic models.

On an equal footing, our simulations allowed us to go deeper inside the reasons for the observed phenomena. We could relate the extent of polaron localization in N2200 with the electrostatic attractive effect of the positively charged n-dopant. We assigned the IR and Raman peaks of functionalized graphene nanoribbons, unveiling the details of the underlying molecular vibrations. We specified the reasons for the different importance of chemical and conformational defects in the IR and Raman spectra of P(VDF−TrFE).

Furthermore, we used DFT to obtain information which could not be straightforwardly obtained by experiments. When studying N2200, we investigated on the role of the ionic radius of the atomic dopant, finding that the electrostatic screening effect of larger alkali metals leads to a more homogeneous and extended charge delocalization. When dealing with PVDF, we highlighted peculiar solid-state effects on its vibrational spectra, noticing that different features depend in different ways on the electrostatic inter-chain interactions.

Future perspectives

Considering the applications of DFT, which is the main theme of this Thesis, in each of our explorations, solvent effects were never taken into account explicitly, mostly in the view of a simple approach which could quickly grasp the leading effects of interest. An immediate extension of this work would be then obtained considering in more detail the environmental effects in the computational model. One may for instance begin with a continuum approach to solvation, evaluating on a case-by-case basis possible extensions to more complete approaches, taking into account their computational demands [91]. The effect of functionalization on GNRs could be also approached more extensively by considering selected series of differently substituted GNRs. Solid-state effects could be explored for P(VDF−TrFE) as well, and its vibrational properties further studied considering more carefully the statistics of both TrFE units and conformational disorder.

Not all the possibilities can be listed here, and new challenges will probably arise in the future, also taking into account the advent of quantum computing [92]. These perspectives are therefore a limited view of a much wider scenario, which is expected to imply the development of new computational and data analysis tools.

References

[1] I. Denti *et al.*, Chemistry of Materials **31**, 6726 (2019).

[2] A. Arrigoni *et al.*, *P(VDF-TrFE) nanofibers: structure of the ferroelectric and paraelectric phases through IR and Raman spectroscopies*, submitted.

[3] `http://alwaysontherun.net/sigur.htm` (accessed July 7, 2020).

[4] P. Hohenberg and W. Kohn, Physical Review **136**, B864 (1964).

[5] W. Kohn and L. J. Sham, Physical Review **140**, A1133 (1965).

[6] A. Zangwill, Physics Today **68**, 34 (2015).

[7] Y. Liang *et al.*, Journal of the American Chemical Society **137**, 4956 (2015).

[8] J. Liu *et al.*, Journal of the American Chemical Society **137**, 6097 (2015).

[9] A. Milani, C. Castiglioni, and S. Radice, The Journal of Physical Chemistry B **119**, 4888 (2015).

[10] A. J. Lovinger, Science **220**, 1115 (1983).

[11] J. L. Bredas and G. B. Street, Accounts of Chemical Research **18**, 309 (1985).

[12] R. Saito, M. Furukawa, G. Dresselhaus, and M. S. Dresselhaus, Journal of Physics: Condensed Matter **22**, 334203 (2010).

[13] K. Popper, *The Logic of Scientific Discovery*, 2019.

[14] P. Halsall, *Letter to the Grand Duchess Christina of Tuscany, 1615*, 1997, `https://sourcebooks.fordham.edu/mod/galileo-tuscany.asp` (accessed July 5, 2020).

[15] R. Feynman, *The Feynman Lectures on Physics*, 1964.

[16] A. Zagoskin, *Quantum Theory of Many-Body Systems*, 2014.

[17] J. C. Maxwell, Nature **8**, 437 (1873).

[18] L. H. Thomas, Mathematical Proceedings of the Cambridge Philosophical Society **23**, 542 (1927).

[19] E. Fermi, Rendiconti Lincei **6**, 602 (1927).

[20] E. Fermi, Zeitschrift für Physik **48**, 73 (1928).

[21] E. Teller, Reviews of Modern Physics **34**, 627 (1962).

[22] W. Y. Robert G. Parr, *Density-Functional Theory of Atoms and Molecules*, 1989.

[23] A. D. Becke, The Journal of Chemical Physics **140**, 18A301 (2014).

[24] M. T. Yin and M. L. Cohen, Physical Review Letters **45**, 1004 (1980).

[25] A. R. Oganov and S. Ono, Nature **430**, 445 (2004).

[26] J. W. D. Connolly and A. R. Williams, Physical Review B **27**, 5169 (1983).

[27] J. Neugebauer and T. Hickel, Wiley Interdisciplinary Reviews: Computational Molecular Science **3**, 438 (2013).

[28] A. N. Kolmogorov *et al.*, Physical Review Letters **105**, 217003 (2010).

[29] H. Gou *et al.*, Physical Review Letters **111**, 157002 (2013).

[30] H. Shirakawa *et al.*, Journal of the Chemical Society, Chemical Communications **16**, 578 (1977).

[31] A. Facchetti, Chemistry of Materials **23**, 733 (2011).

[32] D. de Leeuw, M. Simenon, A. Brown, and R. Einerhand, Synthetic Metals **87**, 53 (1997).

[33] S. Wang *et al.*, Advanced Materials **28**, 10764 (2016).

[34] R. M. Kluge *et al.*, Advanced Functional Materials **30**, 2003092 (2020).

[35] J. Wang *et al.*, Materials Chemistry Frontiers **4**, 661 (2020).

[36] H. G. Kiess, *Conjugated Conducting Polymers*, 1992.

[37] D. Fazzi and M. Caironi, Physical Chemistry Chemical Physics **17**, 8573 (2015).

[38] B. D. Naab *et al.*, Advanced Electronic Materials **2**, 1600004 (2016).

[39] K. S. Novoselov *et al.*, Nature **438**, 197 (2005).

[40] D. R. Cooper *et al.*, ISRN Condensed Matter Physics **2012**, 1 (2012).

[41] M. Fujita, K. Wakabayashi, K. Nakada, and K. Kusakabe, Journal of the Physical Society of Japan **65**, 1920 (1996).

[42] K. Nakada, M. Fujita, G. Dresselhaus, and M. S. Dresselhaus, Physical Review B **54**, 17954 (1996).

[43] Y.-L. Lee *et al.*, Nano Letters **18**, 7247 (2018).

[44] M. E. Gemayel *et al.*, Nanoscale **6**, 6301 (2014).

[45] H. Kawai, Japanese Journal of Applied Physics **8**, 975 (1969).

[46] S. You *et al.*, Micromachines **10**, 302 (2019).

[47] T. Furukawa *et al.*, Japanese Journal of Applied Physics **19**, L109 (1980).

[48] A. Aliane *et al.*, Organic Electronics **25**, 92 (2015).

[49] J. A. Wolny, H. Paulsen, A. X. Trautwein, and V. Schünemann, Coordination Chemistry Reviews **253**, 2423 (2009).

[50] B. Klaumünzer, D. Kröner, and P. Saalfrank, The Journal of Physical Chemistry B **114**, 10826 (2010).

[51] A. Marques *et al.*, Journal of Molecular Structure **1130**, 231 (2017).

[52] J. Kubicki and H. Watts, Minerals **9**, 141 (2019).

[53] J. Liu *et al.*, in preparation.

[54] P. Atkins and J. D. Paula, *Atkins' Physical Chemistry*, 2019.

[55] R. P. Feynman, Physical Review **56**, 340 (1939).

[56] J. Ziman, *Principles of the theory of solids*, 1979.

[57] M. A. Marques and E. K. Gross, *Time-Dependent Density Functional Theory*, 2003.

[58] A. D. Becke, The Journal of Chemical Physics **98**, 5648 (1993).

[59] C. Lee, W. Yang, and R. G. Parr, Physical Review B **37**, 785 (1988).

[60] S. H. Vosko, L. Wilk, and M. Nusair, Canadian Journal of Physics **58**, 1200 (1980).

[61] P. J. Stephens, F. J. Devlin, C. F. Chabalowski, and M. J. Frisch, The Journal of Physical Chemistry **98**, 11623 (1994).

[62] *Avogadro: an open-source molecular builder and visualization tool. Version 1.2.0.*, `http://avogadro.cc/`.

[63] G. Schaftenaar, E. Vlieg, and G. Vriend, Journal of Computer-Aided Molecular Design **31**, 789 (2017).

[64] G. Schaftenaar and J. Noordik, Journal of Computer-Aided Molecular Design **14**, 123 (2000).

[65] M. J. Frisch *et al.*, *Gaussian 09.*

[66] R. Dovesi *et al.*, Wiley Interdisciplinary Reviews: Computational Molecular Science **8**, e1360 (2018).

[67] R. Dovesi *et al.*, *CRYSTAL17, (2017) CRYSTAL17 User's Manual.*

[68] M. K. Kesharwani, B. Brauer, and J. M. L. Martin, The Journal of Physical Chemistry A **119**, 1701 (2014).

[69] A. Maghsoumi *et al.*, Journal of Raman Spectroscopy **46**, 757 (2015).

[70] V. D'Innocenzo *et al.*, Advanced Functional Materials **24**, 5584 (2014).

[71] L. Brambilla, M. Tommasini, G. Zerbi, and R. Stradi, Journal of Raman Spectroscopy **43**, 1449 (2012).

[72] M. Armand *et al.*, Nature Materials **8**, 120 (2009).

[73] X. Han *et al.*, Advanced Materials **19**, 1616 (2007).

[74] K. Fukui, T. Yonezawa, and H. Shingu, The Journal of Chemical Physics **20**, 722 (1952).

[75] M. Nishio *et al.*, Phys. Chem. Chem. Phys. **16**, 12648 (2014).

[76] A. Narita *et al.*, Nature Chemistry **6**, 126 (2013).

[77] D. Rizzo *et al.*, Physical Review B **100**, 045406 (2019).

[78] J. Zhou and J. Dong, Applied Physics Letters **91**, 173108 (2007).

[79] S. Alberti, *Calcolo di fononi in polimeri conduttori e nanoribbons di grafene (GNRs)*, 2016.

[80] M. S. Vezie *et al.*, Nature Materials **15**, 746 (2016).

[81] F. Tuinstra and J. L. Koenig, The Journal of Chemical Physics **53**, 1126 (1970).

[82] A. C. Ferrari *et al.*, Physical Review Letters **97**, 187401 (2006).

[83] E. Fukada and S. Takashita, Japanese Journal of Applied Physics **8**, 960 (1969).

[84] A. J. Lovinger, G. T. Davis, T. Furukawa, and M. G. Broadhurst, Macromolecules **15**, 323 (1982).

[85] T. Soulestin, V. Ladmiral, F. D. D. Santos, and B. Améduri, Progress in Polymer Science **72**, 16 (2017).

[86] R. Hasegawa, M. Kobayashi, and H. Tadokoro, Polymer Journal **3**, 591 (1972).

[87] N. da Costa *et al.*, Journal of Molecular Structure: THEOCHEM **305**, 19 (1994).

[88] A. Nakata *et al.*, Journal of Chemical Theory and Computation **13**, 4146 (2017).

[89] P. Geerlings, F. D. Proft, and W. Langenaeker, Chemical Reviews **103**, 1793 (2003).

[90] H. Yan *et al.*, Nature **457**, 679 (2009).

[91] G. Monard and J.-L. Rivail, *Solvent Effects in Quantum Chemistry*, 2017.

[92] F. Gaitan and F. Nori, Physical Review B **79**, 205117 (2009).